Università degli Studi di Napoli *Federico II*

DOTTORATO DI RICERCA IN FISICA

Ciclo XXXVII

Coordinatore: prof. Vincenzo Canale

Structuring Azobenzene-containing Materials in Three Dimensions with Light

Settore Scientifico Disciplinare PHYS-03/A

Dottorando
I Komang Januariyasa

Tutor
Prof. Stefano Luigi Oscurato

Anni 2021/2024

Abstract

The introduction of three-dimensional micro-architecture to the surface of the material has enabled the realization of a multitude of novel functionalities. The distinctive functionality is derived from the complex interplay between the three-dimensional architectural configuration and the surrounding environment, which separates it from the capabilities of planar or bulk versions of the materials. To date, photolithography has provided a robust methodology for the fabrication of microstructures with the aid of light. A multitude of photolithography techniques have been developed; however, they typically exhibit a trade-off between scalability for large-surface fabrication and flexibility for creating complex microstructures. Azopolymers, a type of polymer containing azobenzene molecules, have been proposed as a promising class of photo-responsive materials for the fabrication of structures on surfaces. The response of the azopolymer to light is strongly influenced by the intensity and polarization of the light, which offers a range of possibilities for creating microstructures on the surface.

This Thesis presents novel ideas and concepts for utilizing the interaction between engineered light and the pre-structured azopolymer surface for the fabrication of three-dimensional micro-architectures. The first concept introduces the wavelength as a novel lithographic parameter for three-dimensionally controlling photodeformation of azopolymer-based micropillars. The application of different wavelengths results in varying degrees of deformation within the micropillar volume, ultimately leading to distinct microstructural morphologies. This approach allows for the straightforward generation of surfaces with distinct wettability characteristics through the use of two distinct wavelengths. The second concept is based on employing spatially engineered intensity of light to reshape azopolymer-based micropillars. The computer-generated holography technique was employed to generate any arbitrary spatial intensity pattern. By rationally designing the intensity patterns in relation to the geometric shape of the micropillar, a variety of geometric structures can be achieved. The third idea introduces an approach that employs a polarization rotator technique to generate spatially rotating polarization. The locally varying polarization provides a spatially reconfigurable driving force, enabling the free reshaping of azopolymer micropillars. This strategy allows for the creation of micro-architectures with tailored orientational features. Additionally, by modifying the scale of the beam in relation to the dimensions of the micropillar, it is possible to achieve different scales of orientational features. The concepts introduced here demonstrate the potential of azopolymer for fabricating complex three-dimensional

micro-architecture on the surface, both in polarization-based and intensity-based control, drastically extending the range of potential applications.

Preface

This thesis reports on my studies conducted during the three years duration of the Ph.D. program in Physics at the University of Naples “Federico II”. The activities have been done in Optics of Materials Laboratory in Physics Department “Ettore Pancini” – University of Naples “Federico II” (Italy) and completed in Optics Laboratory in Physics Department – The College of New Jersey (United States).

First and foremost, I would like to express my gratitude to Dr. Stefano Luigi Oscurato for his dedication in mentoring me as a Ph.D. student and, most importantly, for introducing me to the fascinating and such open-ended research topic of azopolymer and light surface patterning through the “Holo-Lithography” research group. I would also like to express my special thanks to Dr. Marcella Salvatore, as a senior research colleague, and Dr. Francesco Reda, as my Ph.D. colleague, who shared many hours of laboratory work together. Both have been my other “mentors in disguise”, sharing their various conceptual and experimental knowledge with me, despite being busy with their own projects. I would also like to share my special gratitude to Prof. Fabio Borbone for his dedication to the development of the azopolymer materials that we have used for all the studies in this thesis. Last but not least, I would like to express my special thanks to Prof. Pasqualina Maddalena. He is a great figure in our department and especially in our group, never hesitating to give his guidance.

It was also a great pleasure to have the opportunity to visit the Optics Laboratory at TCNJ, hosted by Dr. David J. McGee. From this research collaboration activity, I have gained many new knowledge and experience and broadened my understanding of azopolymer research topics. Specifically, the study reported in one chapter of this thesis was conducted in this laboratory. In addition, I have learned a lot about the art of teaching and communication from David J. McGee, as he is known as a great teacher in the Physics Department – TCNJ.

I would like to send my gratitude to Prof. Lian Nedelchev, PhD (Bulgarian Academy of Sciences) and Prof. Anna Kozanecka-Szmigiel (Warsaw University of Technology) for their time and dedication to review this thesis, giving valuable insights, comments, and suggestions to improve the overall presentation of this thesis.

I would like to use these final words to state that this thesis does not only reflect the contribution of the author, but more importantly demonstrates the accumulation of

knowledge, ideas, and concepts exchanged between my Ph.D. mentor, my colleagues, and many researchers I have met along the way.

I Komang Januariyasa

Napoli – October 2024

Table of Contents

Table of Figures

Chapter 1

Chapter 2

Chapter 3

Chapter 4

Table of Tables

Introduction

The development of three-dimensional (3D) structures with well-defined features on the surface from submicro- to micrometer scale is gaining momentum due to their effect on improving the functionality of the material surface. The emergence of three-dimensional structured surfaces is driven by their distinctive interactions with external environments (*1–4*). This kind of special interactions can be illustrated by the ability of the surface to manipulate the propagation of the light in photonic devices (*5–7*), control the liquid-surface interaction in surface wettability (*8*, *9*), generate a structural adhesion for adhesive technologies (*10, 11*), have a moveable part in the structure for actuators and sensors (*12*, *13*), and provide a morphological adaptability to the environment for wearable devices (*14*, *15*). These capabilities illustrate the potential of structured surfaces and differentiate their functionality from that of their planar and bulk counterparts.

The ability to create well-defined and functional structures on surfaces is made possible by the advancement of numerous microstructure fabrication methods. A plethora of techniques have been developed thus far, each relying on diverse mechanisms and involving interdisciplinary fields to make it possible (*1–4*). One of the most powerful concepts for the production of structures on surfaces is the utilization of light-matter interactions (*1*). This approach, well-known as photolithography, is based on a fundamental concept: inducing a chemical reaction within a material on the surface using light. Then it is typically followed by a series of post-development techniques, such as selective etching and residual removal with chemical processes, ultimately resulting in the formation of morphological features on the surface. The use of light as a stimulus for the formation of surface structures offers a number of advantages, including remote triggering, spatiotemporal control of the photoreaction, and precise manipulation of the matter-light interaction (*1*, *2*). Furthermore, the ongoing developments in the field of optics, the progress in the development of photo-responsive materials, and the growing understanding of the interaction between light and matters are driving the advancement of photolithography.

The photolithography family includes a wide range of techniques that employ diverse classes of photo-reactive materials, optics, and light-matter interactions (*1*). These

elements define the intrinsic characteristics of a particular technique, which may include aspects such as resolution, accuracy, flexibility, throughput, cost, and scalability. The primary trade-off between these characteristics lies in the *scalability* of the technique to produce large surface areas in a short time, and the *flexibility* to manipulate the spatiotemporal interaction between the material and the light. Conventional mask-based photolithography represents one of the earliest techniques to employ light for surface fabrication, offering high scalability due to its parallel nature. The fundamental concept of this technique is the utilization of a physically patterned mask to impart a structured spatial intensity (an image) within the light beam prior the exposure of the photoresist surface (*1, 2*). The photoresist's photochemical properties dictate whether it will become soluble or insoluble in a specific solvent following exposure to light. Subsequently, an additional etching process will result in the formation of a positive or negative pattern on the surface. However, this technique lacks the flexibility to control the complexity of the surface pattern, as the final microstructure is the protruded two-dimensional pattern of the projected image of the mask (*2*). Furthermore, the necessity for a physical mask introduces an additional limitation due to the requirement for the production of new masks with each new pattern design. The contrasting example of photolithography that allows for substantial flexibility in design is direct laser writing, especially in its implementation as two-photon lithography. This technique is based on a specially designed class of materials that is capable of efficient non-linear two photon absorption, thereby facilitating the desired polymerization reaction (*1, 16*). Consequently, when a tightly focused beam is exposed within the volume of the polymer, only the polymer around the waist of the focused beam (where the intensity is higher) can undergo polymerization. By maneuvering the focused beam within the volume of the resinous polymer in a three-dimensional path, any three-dimensional shape or microstructure on a surface can be created. However, this high degree of flexibility comes at the cost of scalability for large functional surfaces due to the serial nature of the technique. The necessity for specialized instruments and the lack of scalability renders two-photon lithography an arduous and costly technique for the production of microstructures on surfaces (*1, 2*). Thus far, it remains a challenge to find an alternative technique that offers flexibility in architectural design and a reasonable time and cost ratio in relation to the yielded area.

Recently, azopolymers have attracted the attention of the scientific community due to their potential for low-cost surface patterning strategies. Azopolymers are a class of polymers that contain azobenzene molecules, making them photo-responsive materials (*17*). A defining characteristic of azopolymer–light interaction is the light-driven mass migration, which sets it apart from other photo-responsive materials (*1, 18–20*). This light-driven mass migration does not result from ablative or removal processes, nor it is

a thermal-induced phenomenon (*17*, *18*, *20*). Since their initial introduction (*21*, *22*), it is widely accepted that the primary driving force behind this mechanism is the photochemical behavior exhibited by azobenzene molecules. Upon absorbing photons within the typical UV-visible absorbance band, azobenzene molecules undergo a cyclic *trans-cis-trans* isomerization (*17*). This cyclical transformation of states gives rise to a unique nano-mechanical phenomenon, whereby the molecules undertake random reorientation in each cycle until they ultimately align their long axes perpendicular to the electric field direction (*17*). When these molecules are embedded in a polymer chain, the cyclic isomerization of azobenzene molecules in the side chains of the polymer drives the realignment of the main chain to be parallel to the electric field direction, resulting in the straightening and alignment of the polymer with the polarization direction. This produces a viscoelastic tensile stress within the azopolymer volume in the direction of polarization (*20, 23*). The mass migration at the macroscale occurs with a relatively low energy beam and at temperatures that are below the glass transition temperature of the polymer (*17*, *18*, *20*, *23*). In contrast to the conventional photoresist employed in photolithography, the surface deformation observed in azopolymers following exposure, although stable at standard environment conditions, is not permanent. This allows for the implementation of strategies such as multi-step exposure and the erase-then-rewrite approach (*17*, *18*, *20*).

The most striking feature of the mass migration in azopolymers is its substantial dependence on two properties of light: intensity gradient and polarization (*1*, *18–20*, *23*). The general mechanism underlying the intensity gradient dependency is the tendency of the mass to migrate from an area experiencing a higher intensity of light to an area experiencing a lower intensity. In addition to the intensity gradient, mass migration tends to follow the direction parallel with that of the dominant electric field component (e.g. in the direction of linear light polarization). These dependencies have led to the introduction of various surface patterning strategies, which exhibit different degrees of flexibility and scalability. Two crucial factors influence the flexibility and scalability of the final surface morphology: the characteristics of the light field (e.g., collimated with varying polarization states, spatially modulated intensity, or spatially varying polarization) and the initial morphology of the azopolymer surface (e.g., smooth flat surface, pre-patterned surface, or suspended micro-volume systems).

The majority of strategies currently employed in the field of azopolymers-based surface patterning involve diverse combinations of engineered light fields and preparation of the initial surface states. The most straightforward approach to surface patterning, in terms of experimental configuration, is the spontaneous formation of surface relief gratings (SSRGs) (*24–26*). These arise when an azopolymer surface is exposed to a

homogeneous, collimated laser beam. When a linearly polarized beam is used, the SSRGs form a one-dimensional grating-like structure (*24*). Conversely, circular polarization induces the formation of hexagonal-like micro-nodes (*25*). Another typical approach exploits the intensity gradient dependency for the formation of sinusoidal surface relief gratings (SRGs) by exposing the flat surface to a sinusoidal intensity pattern generated from a two-beam interference configuration (*18*, *22*, *27*). The resulting gratings exhibit a pattern that is the inverse of the intensity distribution, with peaks occurring in regions of low intensity and valleys in regions of high intensity. An alternative approach to the fabrication of SRGs is based on the periodic rotation of linear polarization with a constant intensity, generated by the interference of two circularly polarized beams with opposite handedness (*28*). In this instance, the peaks emerge in regions experiencing *s*-polarization, while the valleys arise from *p*-polarization. Furthermore, different variations of polarization-based two-beam interference have been demonstrated to produce SRGs with varying grating profiles (*28*, *29*). To enhance the flexibility in creating surface patterns, several experiments have demonstrated the versatility of computer-based holography, which enables the spatial modulation of light intensity (*30*). This capability expands the potential applications of azopolymers, including their use as reprogrammable holographic plates (*31*). Despite the diverse surface patterns that can be generated through these strategies, the ability to control the 3D architectural features of the produced microstructures remains a challenge.

In the pursuit of flexibility in the fine-tuning of 3D micro-architectural features, a sub-field of research has emerged within the broader field of azopolymers photo-structuring. This sub-field is devoted to the exploitation of pre-structured azopolymer surfaces, wherein a pre-existing microstructure array is imprinted on the surface through preliminary lithographic step prior to illumination. This methodology enables the fabrication of intricate 3D microstructures in a simplified manner by directly photo-deforming the original microarchitecture into more complex architectures that are not straightforward to achieve with most other lithography techniques.

The most common pre-structured approach employs the use of a micropillar array that is preliminarily stamped on the azopolymer surface through the application of soft lithography (*32*–*38*). As an initial example, upon irradiation of a homogeneous collimated beam with linear polarization, the micropillar undergoes photodeformation, exhibiting an elongation parallel to the orientation of the linear polarization (*34*, *37*). It is essential to note that the most fundamental aspect of this approach is its dependency on polarization. The introduction of a localized microvolume, as exemplified by the micropillar array on the surface, enables the surface to directly capture the vectorial

property of light (i.e., polarization state and directionality). In essence, the mass migration, manifested as photo-induced deformation of the microvolume, follows the major component of the electric field. The application of different variations of polarization can induce distinct three-dimensional shapes. For example, the use of a circularly polarized beam with micropillars results in the formation of an isotropic lateral deformation on the micropillar surface (*14*, *34*, *39*). This deformation eventually gives rise to a mushroom-like microstructure, which can be utilized for superhydrophobic applications (*33*). In terms of utilizing the directionality of polarization-dependent mass migration, unidirectional photodeformation can be achieved by employing a slanted illumination scheme. This results in an unbalanced driving force for the original micropillar, leading to the formation of asymmetric shapes (*32*, *34*, *36*). Other optical strategies, including polarization-based interference (*35*) and angular momentum beam (*40*), as well as alternative material systems, such as azopolymer-based microspheres (*41*), breath figures (*42*), and submicro-holes (*39*), have been investigated. These findings illustrate the adaptability of this approach as a comprehensive technique for the fabrication of intricate 3D micro- and submicro-architectures on the surface. However, a notable number of potential strategies remain unexplored.

This thesis primarily investigates novel approaches and concepts for fabricating intricate three-dimensional micro-architectures using the distinctive directionality of the azopolymer's response to light through in pre-structured surfaces. This will include an examination of the influence of an alternative optical property, namely the light wavelength; the adoption of holographic optical approaches initially used in flat surface schemes; and an unprecedented strategy for producing unconventional micro-architectures using a computer-programmable polarization rotator.

The Structure of Thesis

Chapter 1 will provide an overview of the fundamental physical aspects underlying the phenomenology of azopolymers. The introduction begins with an examination of the photochemical properties of the azobenzene molecule, which serves as the fundamental driving motor behind all observed phenomena at the macroscopic scale. How this molecular phenomenon translates to a surface patterning capability of azopolymers will be described phenomenologically. In general, azopolymer-based surface patterning approaches can be categorized into different levels depending on the complexity of the optical field and the azopolymer surface systems. In the final part of the chapter, a discussion will be held on the topic of photodeformation of azopolymer-based microvolume systems. This will serve as a further introduction to this specific subfield, which will then become the basis for the next chapters.

Chapter 2 introduces the concept of wavelength of light as a new parameter that can be utilized to control the complexity of three-dimensional microstructures. This is based on the wavelength-dependent penetration depth of light when propagating within the azopolymer volume. The general approaches to utilizing the directionality of photodeformation in azopolymer-based microstructures are determined by the lateral deformation, which can introduce varying degrees of asymmetry contingent on the optical schemes employed. The varying wavelength-dependent penetration depth of light can be exploited to introduce a new degree of control, whereby different penetration depths of light induce photodeformation at varying levels of depth within the azopolymer-based microvolume. By modifying the wavelengths, this study has demonstrated the capacity to induce different morphological features in the final microarchitectures. Additionally, a demonstration of wettability control with the fabricated structures will also be presented.

Chapter 3 presents an innovative approach that integrates computer-generated holography (CGH) based on a Spatial Light Modulator (SLM) with a pre-structured azopolymer surface. The conventional approaches used to fabricate azopolymer-based complex three-dimensional microstructures rely mainly on the directionality of mass migration, which is guided by the direction of polarization of light. This study, however, investigates the potential of utilizing a spatial intensity pattern of light to induce a three-dimensional morphing of pristine micro-architectures. This combination provides a flexible technique to produce various three-dimensional microstructures with high diversity, localized control, and group selectivity.

Chapter 4 proposes a novel strategy to tap the maximum potentiality of the directionality of light-induced mass migration in azopolymer-based microvolume systems. In this study, a computer-controlled polarization rotator based on a SLM is employed to generate any spatial polarization distribution in the wavefield of a laser beam (*43–46*). By rationally designing the polarization map in two dimensions to align with the geometric configuration of the pre-existing microstructures on the surface, a variety of unconventional microstructures and surface configurations can be achieved. This technique reimagines the spatially changing polarization direction across the planar space as “guiding pathways” when it interacts with the azopolymer-based microvolumes on the surface. Since the wavefield with spatially rotating linear polarization can be described as a 2D vectorial field as soon as it interacts with the surface, the way of this approach producing unconventional micro-architectures is called “vectorial field-guided lithography”.

Lastly, conclusions and future prospects for this work are presented.

1 Azopolymers:

Photo-active materials for microstructure fabrication

Azopolymers are a class of polymers that are incorporated with azobenzene molecules. The defining characteristic of this class of polymers is its photo-responsive property. It is widely accepted that fundamental mechanism underlies this photo-responsiveness is the interaction between the light and the azobenzene molecule. Azobenzene exists in two distinct isomerization states: the *trans*-state and the *cis*-state. The transformation from *trans* to *cis* and *vice versa* can be initiated by the absorption of a photon. In most cases, the wavelength of the light that triggers both processes is within an overlapping range (typically 350–550 nm). Consequently, it is feasible to initiate a cyclic photoisomerization process (*trans-cis-trans*) by irradiating the molecule with a beam of light within the proper range of absorbable wavelength. This photo-triggered cycle induces a phenomenon at the macroscale level, namely photo-driven mass migration. The mass migration of azopolymers is significantly influenced by the properties of the light field, including factors such as intensity gradient, polarization, and effective wavefront. These dependencies offer a multitude of possibilities for controlling mass migration, which can subsequently be used to control the formation of azopolymer-based surface patterns. This chapter presents an overview of azopolymers as a material for surface patterning. The discussion begins with an examination of the fundamental photochemistry of azobenzene and its transformation into a functional mass migration mechanism for the creation of surface reliefs. This chapter presents a variety of strategies, ranging from the simplest to the most complex surface relief features, that have been studied. The final section focuses on a strategy of using a pre-structured surface to form complex three-dimensional micro-architectures, which is the main focus of this work. The chapter discusses several strategies that have been reported on this intriguing topic to provide a comprehensive introduction to the urgency, flexibility, and most importantly, the unexplored potential of producing three-dimensional micro-architectures using azopolymers.

1.1 Azobenzene Molecules

1.1.1 Photochemistry of azobenzene molecules

Azopolymers are defined as a specific type of polymer that contains azobenzene molecules. The photo-responsive behavior of these polymers is fundamentally based on the photochemical properties of the azobenzene molecules. Azobenzene molecules are chemically characterized by their azo bond (-N=N-), which interconnects two phenyl rings (*17*). This chemical structure exhibits intense optical absorption, which provides the foundation for the photochemistry of azobenzene molecules. Upon absorbing a photon, the azobenzene molecule undergoes photoisomerization, which results in a transition from the *trans*-state to the *cis*-state or *vice versa* as illustrated in Figure 1.1(A).

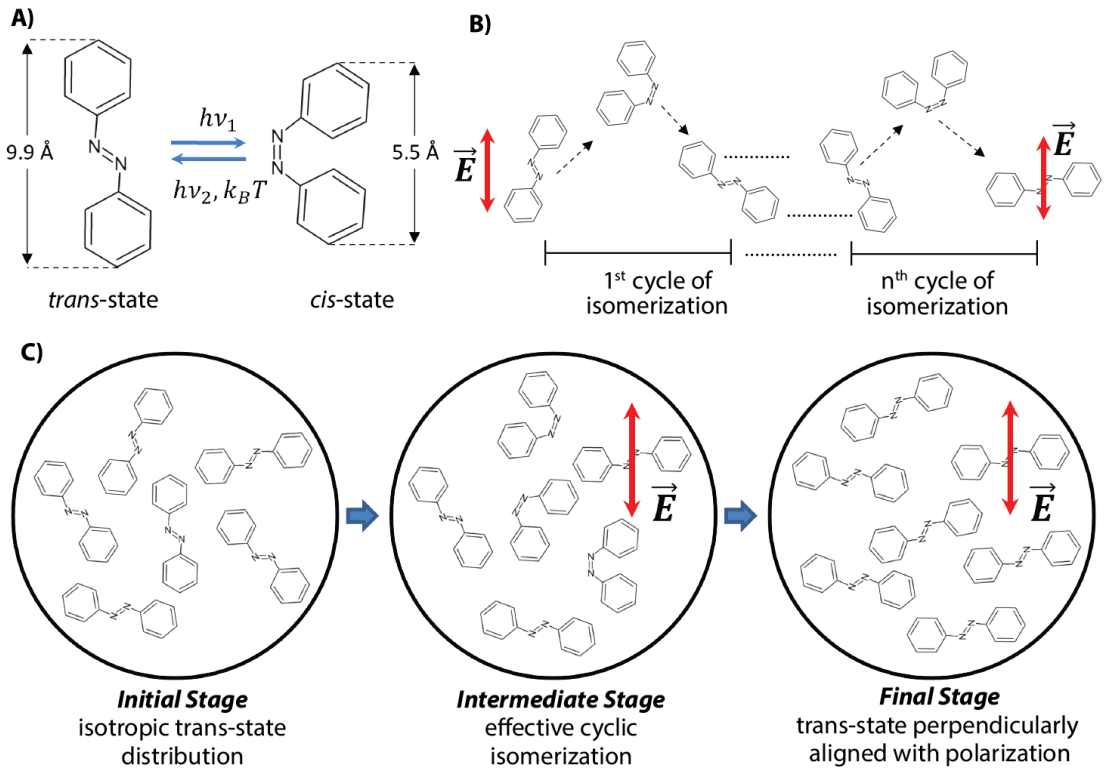

Figure 1.1 The photochemistry and photo-orientation of azobenzene molecules. (A) *Trans*-state and *cis*-state of the azobenzene molecule. (B) The cyclic photo-isomerization of the azobenzene molecule. (C) The state of azobenzene molecules from isotropic *trans*-state to the "hole-burning" state. (A–C) is adapted from (*47*).

The *trans*-azobenzene is distinguished by its planar rod-like configuration, whereas the cis-azobenzene is characterized by the formation of an angle of around 90° between the two phenyl rings. From a thermodynamic standpoint, the *trans*-state is the more favorable configuration. Consequently, under conditions of darkness or regular ambient illumination, azobenzene molecules are predominantly in the *trans*-state. Conversely, the cis-azobenzene exists in a metastable state due to its tendency to revert to the *trans*-state through thermal or photon absorption. Notably, the photo-switch in azobenzene molecules is fully reversible, rapid, and efficient, representing one of the most efficient photoreactions known to date (*17*). The mechanism of the photo-switch may involve a general rotation or inversion about the azo linkage (*48*). The geometrical change from *trans* to *cis* induces a change in the occupied volume, where a volume of approximately 0.12 nm^3 or 0.28 nm^3 is required for the transition via the inversion or rotation, respectively (*17*).

1.1.2 Photo-orientation

The photo-switching of *trans-cis* and *cis-trans* in azobenzene molecules is associated with broad and overlapping absorption bands, which typically fall within a range of 350–550 nm (*18*). Consequently, illumination of a monochromatic light source, such as a laser with a wavelength within the indicated range, will result in the initiation of a cyclic photoisomerization process. The continuous cycling of *trans-cis-trans* results in a distinctive statistical phenomenon, known as "photo-orientation". In general, the azobenzene molecule exhibits a tendency to orient itself (the long axis of the *trans* molecule) perpendicular to the electric field vibration (polarization of light) while undergoing the *trans-cis-trans* isomerization, as illustrated in Figure 1.1(B). This is due to the dipole interaction of the trans molecules with the polarized light. Indeed, the probability of photon absorption on this molecule varies as $cos^2\varphi$ (φ represents the angle between the light polarization and the azo dipole axis) (*17*). In other words, the probability of light absorption is highest for molecules with their axes parallel to the polarization, and lowest for those forming a right angle with it. During this chaotic and super-fast motion (in the order of picoseconds (*17*)), each time a molecule absorbs a photon, it undergoes a random re-orientation. Figure 1.1(C) depicts the evolution of the state of molecules over a significantly larger time frame. Initially, the molecules are randomly oriented. Following the illumination with a linearly polarized light, the molecules gradually orient themselves perpendicular to the direction of polarization. In the final stage, as illustrated in Figure 1.1(C), all molecules are aligned orthogonally with the polarization direction, resulting in minimal molecular movement due to the drastic depletion of the photon absorption probability, which is typically described as

"orientation hole-burning". It is noteworthy that the application of circularly polarized light can be employed to achieve a random distribution of molecular orientation states (*17*, *18*), as illustrated in the initial configuration depicted in Figure 1.1(C).

1.2 Light-Driven Mass Migration in Azopolymers

1.2.1 The light-induced surface reliefs on azopolymers

The most intriguing phenomenon emerging from the photoactive properties of azobenzene molecules is the photoinduced mass migration observed in azobenzene-containing polymer systems. The phenomenon was initially observed by two independent research teams (*21*, *22*), who created a periodic surface relief on an azopolymer film by illuminating a sinusoidal intensity pattern of light produced by the interference of two p-polarized beams (Figure 1.2(A)).

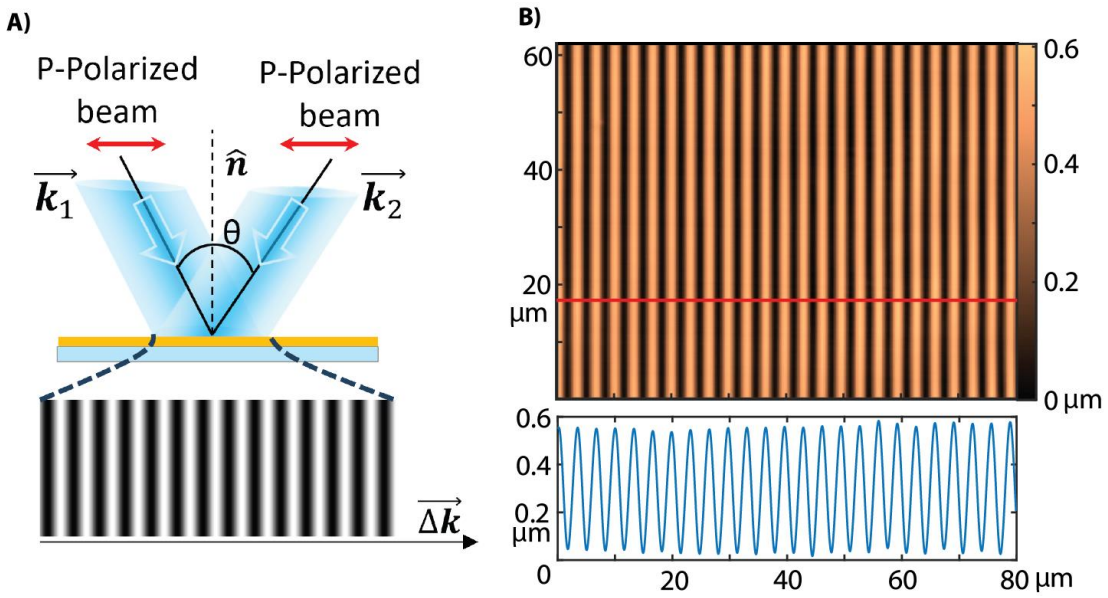

Figure 1.2 Surface Relief Gratings. (A) The typical *p-p* two-beam interference system. (B) The morphology and the surface profile of surface relief gratings after an exposure from the interference pattern. (A–B) are adapted from (*47*).

Figure 1.2(B) displays the typical periodic surface relief (commonly referred to as surface relief gratings or SRGs) with its corresponding illumination pattern. The periodicity of SRGs is in accordance with that of the sinusoidal pattern of light, thereby

replicating the spatial intensity variation on the surface. Two distinctive characteristics are exhibited by light-induced surface reliefs in azopolymers. Firstly, the light-induced surface relief on azopolymers can be triggered by a low power beam, which is insufficient for a blasting or destructive process (*17*, *18*, *20*). Secondly, the non-thermal aspect of the surface patterning on azopolymers has been demonstrated by some studies, which have shown that the surface relief occurs well below T_g (*17*, *18*, *20*).

1.2.2 Intensity and polarization dependence

The mass migration of azopolymers exhibits a strong dependency on the intensity gradient and the polarization of light. The effect of these two properties of light is an inseparable component of the surface relief. However, in any given instance, one property can have a more pronounced effect on the surface relief than the other, depending on the beam configuration and/or the surface state. The simplest case in which the mutual effect of these two parameters can be observed is in the formation of micro-pits induced by a focused Gaussian beam (*49*, *50*). The initial illustration will be Figure 1.3(A) showing the micro-pit that is induced by a focused Gaussian beam of circularly polarized light. As can be observed in the profile of the micro-pit, the surface area that experiences the peak of the intensity tends to form a pit with negative amplitude relative to the initial surface level. Conversely, a lobe formation that is circularly surrounding the pit exhibits a positive amplitude. This lobe is the result of a more general phenomenon that occurs in light-induced surface relief on azopolymer: mass tends to migrate from a higher intensity of light to a lower intensity. In this example, the circular polarization of the beam produces an isotropic mass migration in all directions, resulting in a non-preferential orientation of the surface features. When a linearly polarized Gaussian beam is employed instead of a circular one, a comparable micro-pit is formed, but with a directional feature, as shown in Figure 1.3(B). This straightforward illustration demonstrates another characteristic of light-induced mass migration in azopolymers. The material tends to be transported in the direction of the electric field vibration (polarization direction).

A particular surface configuration can provide a further illustration of how the direction of the electric field predominantly guides mass migration, despite the absence of a significant intensity gradient of light. In this configuration, micro-sized scratches are inflicted on the azopolymer surface in an orthogonal manner prior to illumination with light. The introduction of these scratches creates a “structural discontinuity” on the surface, enabling the surface to capture the lateral directionality of mass migration (*51*). Figure 1.3(C) illustrates the evolution of the morphology of the scratch following exposure to a homogeneous beam with linear polarization along one of the scratch axes.

The scratches oriented orthogonal to the polarization exhibit a gradual filling and flattening, while the parallel scratches remain largely unaffected.

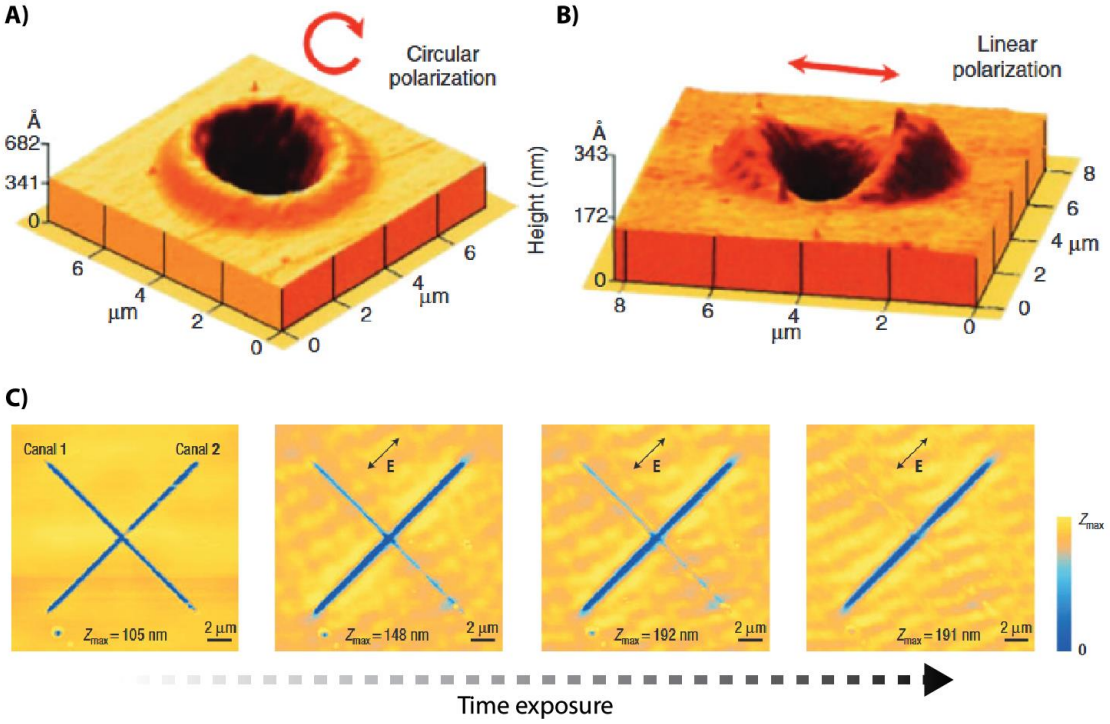

Figure 1.3 Intensity and polarization-dependent of mass migration in azopolymers. The surface reliefs on an azopolymer surface after an exposure of a focused gaussian beam with (A) circular and (B) linier polarization. (A–B) are adapted from (*49*) with permission from AIP Publishing. (C) The polarization-dependent of mass migration in the case of crossed nano-tunnels. (C) is adapted from (*51*) with permission from Nature.

In order to reveal the fundamental mechanics behind directional mass migration, various studies have been proposed, which are beyond the scope of this thesis. However, they are summarized in review papers (*18*, *20*). A recently proposed model, referred to as the "orientation approach", suggests the underlying mechanism behind this directional mass migration (*23*). The orientation approach provides an interpretation of directional mass migration in typical azopolymer systems, wherein azobenzene molecules are attached in the side-chain configuration. In the case of linear polarization, the polarization-dependent mass migration is caused by the alignment of the azobenzene molecules in the side chain configuration, which is perpendicular to the direction of the electric field vibration. During the *cis-trans-cis* cyclic isomerization process, the azobenzene

molecules gradually align their axes perpendicular to the polarization direction. Simultaneously, the main chain of the azopolymer exhibits a tendency to straighten up perpendicular to the main axis of the azobenzene molecules, as illustrated Figure 1.4(A). The straightening and alignment of the main chain results in the formation of tensile stress that is oriented parallel to the direction of polarization. This tensile stress acts as a driving force for mass migration in the direction of polarization. This phenomenon was further demonstrated in a simple configuration, in which a micro-post was deformed along the polarization direction (Figure 1.4(B)). In the case of circular polarization, there is no directional preference across the transverse component of the beam. However, the azobenzene molecules tend to gradually align perpendicularly with the wavefront (i.e., the plane where the polarization lies) or parallel to the propagation vector of light. This same mechanism occurs at this level regardless of the polarization state, resulting in the straightening and alignment of the main chain of the azopolymer perpendicular to the propagation vector of light. In the absence of a preferred direction, the tensile stress within the azopolymer volume is distributed equally in all radial directions (Figure 1.4(B)).

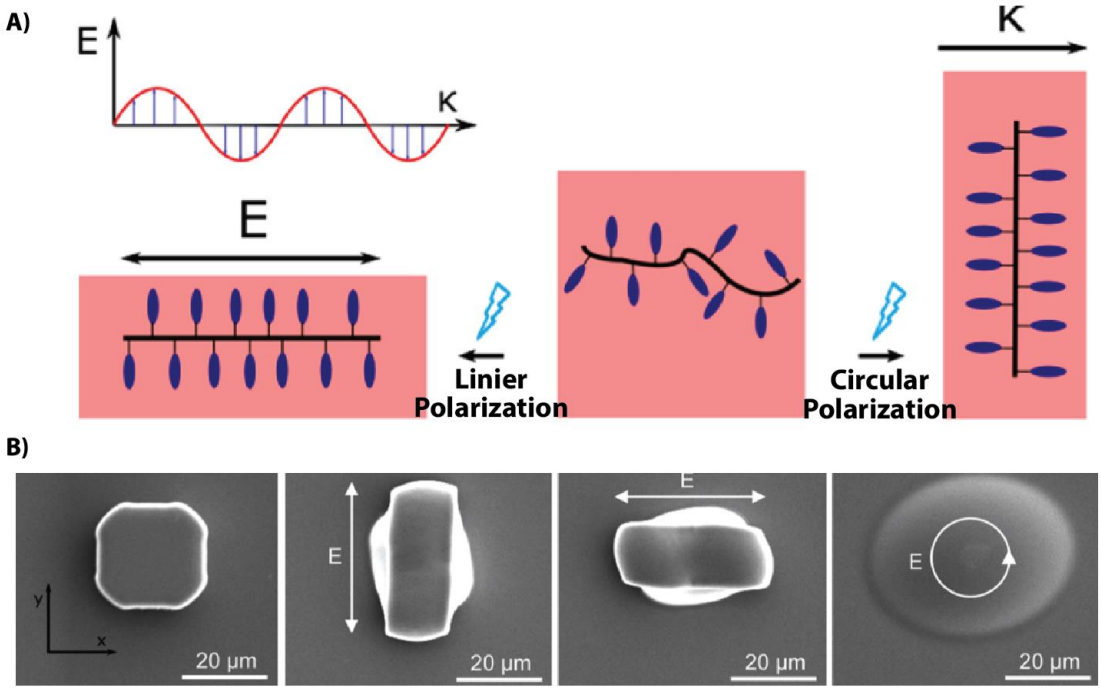

Figure 1.4 The orientation approach. (A) The schematic illustration of the alignment of azobenzene molecules and the main chains of the azopolymer after an exposure of a homogeneous beam with linier polarization or circular polarization. (B) The micro-post

after the illumination from light with different polarization states. (A-B) are adapted from (*23*) with permission from ACS Publications.

1.3 Light-driven Surface Patterning on Azopolymers

In the context of using azopolymer for the creation of structures on surfaces, two distinct strategies are typically employed: the use of a flat surface and the utilization of a pre-patterned surface. The latter approach offers a distinctive capacity to generate diverse, intricate three-dimensional micro-architectures. This section presents an introductory overview of the utilization of azopolymer flat surfaces for surface patterning. It outlines the advantages and disadvantages of this strategy and, most crucially, highlights the limitations of this approach in producing complex three-dimensional micro-architectures on surfaces.

1.3.1 Spontaneous surface reliefs gratings (SSRGs)

In the context of the experimental configuration, the most straightforward approach to surface patterning is the formation of spontaneous surface reliefs. This phenomenon occurs when a free flat surface of azopolymer is illuminated with a beam of homogeneous intensity (*24–26*, *52*). Spontaneous surface reliefs (commonly designated as spontaneous surface relief gratings, SSRGs) on azopolymers can be characterized as surface modulations exhibiting a range of sizes, from hundreds of nanometers to micrometers, and exhibiting a variety of organizational patterns, from random-like to regular-like, contingent on the specific parameters under consideration. One of the parameters that exerts a significant influence is the polarization state. The formation of a one-dimensional grating-like structure is a result of linear polarization, wherein the grating vector is oriented orthogonally to the polarization direction. A circularly polarized beam induces the formation of a two-dimensional micro-node, which, depending on the time scale, can range from an irregular to a hexagonal-like formation. Another optical parameter, such as wavelength, has been demonstrated to regulate the periodicity and size of the protrusions observed in SSRGs (*24*). The intensity of the laser beam determines the rate of growth of the SSRGs (*25*). From the standpoint of materials science, the thickness of the azopolymer film can influence the modulation and periodicity of the SSRGs (*53*).

1.3.2 Surface relief gratings (SRGs)

Surface relief gratings (SRGs) have been the subject of extensive research and investigation. The immediate generation of a periodic superficial configuration that reflects the intensity distribution of light or the periodic polarization variation represents a compelling concept for the fabrication of large-scale functional surfaces. In the case of two-beam interference, the periodicity (P) can be controlled by the smallest angle (θ) formed between the incident beams and the beam wavelength (λ), as described by Bragg's equation: $P = \lambda/[2\sin(\theta/2)]$ (*54*). The modulation of the grooves is related to the fluence of light (a combination of intensity and time), with modulation ranging from tens of nanometers to 1.7 micrometer (*18*, *55*). The non-permanent process of light-induced surface relief on azopolymers represents a novel pathway for the generation of more intricate surface patterns. Another SRG can be induced on an azopolymer surface that has already undergone patterning through the use of sequential illumination, a process known as multiplexing. The result is a complex two-dimensional superficial relief. The number and organization of each multiplexed illumination determines the formation of multiplexed SRGs.

1.3.3 Formation of arbitrary surface reliefs

The formation of surface reliefs like SSRGs and SRGs demonstrates that the evolution of different surface features is heavily influenced by the manner in which the field of light is engineered. This indicates that if a field with intricate characteristics can be engineered, the surface morphology in turn will likely be capable of capturing it. One promising strategy for light manipulation is the use of computer-generated holography (CGH). The method relies on a spatial light modulator (SLM) to modulate the wavefront of the light and on an accurate Fourier transform algorithm to produce any 2D spatial intensity pattern of light in the sample plane. The significant benefit of this approach is that the intensity pattern of light can be meticulously designed and regulated by a computer using standard computer graphics software. By employing this technique, Oscurato *et al* (*30*) were able to showcase the potential of combining azopolymer and CGH for the production of intricate surface reliefs with high precision and adaptability, as illustrated in Figure 1.5(A). Moreover, Reda *et al* (*31*) employed the flexibility of CGH to produce holographic surfaces (Figure 1.5(B)). Instead of imparting the holographic image to the surface as demonstrated above, the surface now contains an accurate pattern (Figure 1.5(C)) that is designed to produce a holographic image in the far field through a probe beam (Figure 1.5(D)).

The ability to spatially distribute the intensity of light at the micro-scale has significant potential for surface patterning, as demonstrated in the above example. Chapter 3 of this thesis adopts this technique to introduce an innovative strategy for reshaping pre-existing microstructure. By enabling the localization of intensity, the study in Chapter 3 has demonstrated the capacity to produce diverse micro-architectures with deterministic characteristics.

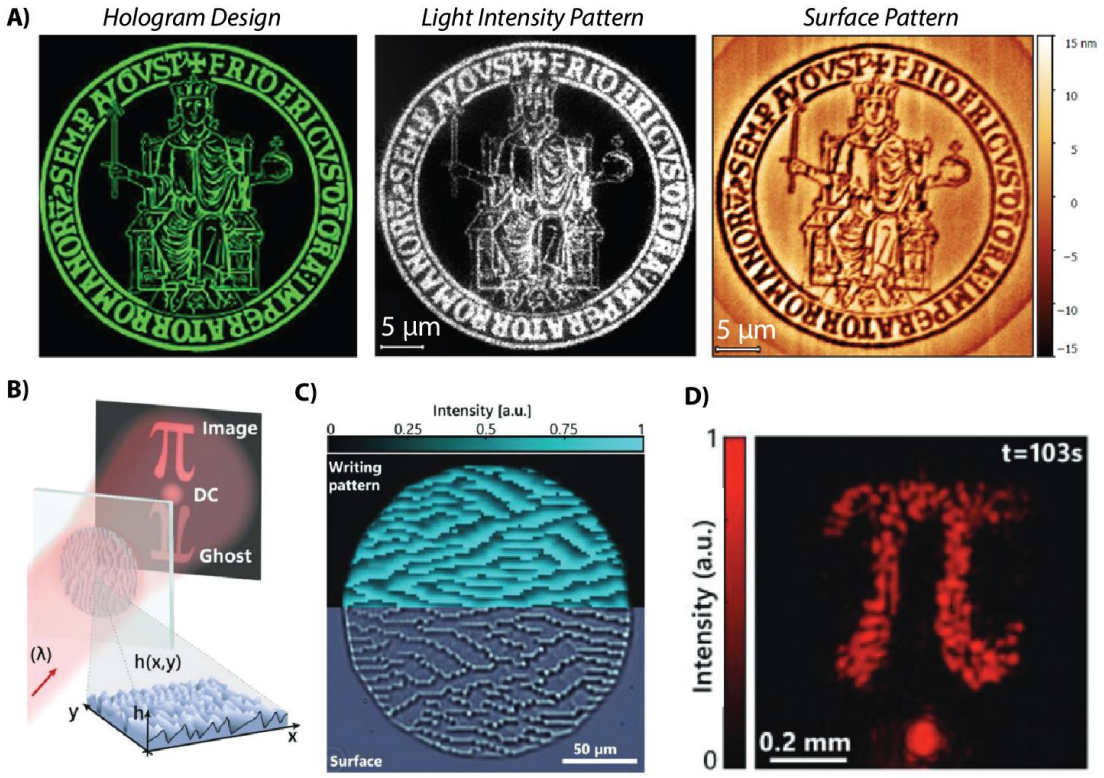

Figure 1.5 Accurate Design and Arbitrary Surface Relief. (A) The basic demonstration of computer-based holography to write an arbitrary pattern on the surface. Adapted from (*30*) with permission from Nature. (B) The experiment design of computer-based holography for making reprogrammable holographic masks on azopolymer surface. (C) The holographic pattern to write and the written pattern on azopolymer surface and (D) the far-field image produced when the surface is challenged with a probe beam. (B–D) are adapted from (*31*) with permission from Wiley.

1.4 Pre-structured Azopolymer Strategy for Complex 3D Architectures

The aforementioned approaches exemplify a multitude of strategies that can be utilized to create functional surfaces for a vast array of applications. However, these strategies are constrained in their ability to control the three-dimensional (3D) architecture of the microstructures. This limitation stems from the fact that they utilize the flat surface as

the initial state. The light-induced mass migration originating from a flat surface gives rise to the formation of modulations that are parallel to the normal axes of the surface, which means that the greatest degree of control that can be achieved with azopolymer flat surfaces is in the organization of these modulations on a 2D plane (parallel to the surface plane). The modulations typically exhibit a sinusoidal groove (in 1D SRGs) or bump-like architecture (in SSRGs and multiplexed SRGs).

As discussed in the Introduction, 3D micro-architectures play an important role in a variety of applications. Due to their intricate nature, 3D micro-architectures can interact with their surroundings in ways that are distinct from their planar counterparts, let alone the bulk version of the material. A variety of lithography techniques are available for the creation of complex 3D microarchitectures on surfaces. As previously discussed in the Introduction, two-photon lithography represents a standard technique for the creation of complex 3D micro-architectures. The serial nature of two-photon lithography renders it well-suited for the construction of microscale 3D intricate architectures, but this approach is inherently time-consuming and not yet scalable. In contrast, techniques that employ a parallel nature can produce large-scale surfaces at a relatively fast pace, but they often exhibit a lack of architectural complexity. For instance, mask-based photolithography is a prominent example of this limitation.

The light-induced mass migration observed in azopolymers provides a distinctive mechanism that is rarely observed in other photo-responsive materials. The combination of intensity-polarization sensitivity in azopolymers can be employed in a variety of strategies. The polarization dependency phenomenon is the dominant factor influencing mass migration when a discontinuity is introduced at the surface. This mechanism endows the surface with the ability to capture the vectorial properties of the field of light. In consideration of these findings, a number of studies have investigated the potential benefits of creating pre-structured azopolymer surfaces prior to illumination. By combining experimental parameters, namely different architectures of the pre-structured microstructures and different configurations of the field of light, a range of strategies can be derived. This section will present the strategies that have been developed based on pre-structured azopolymer surfaces to create complex 3D micro-architectures.

1.4.1 Polarization-based reshaping of pre-structured azopolymer surface

The polarization dependency of directional mass migration in azopolymers is most effective when it is used on a surface that contains lateral discontinuity. The current strategies are oriented towards the reshaping of micro-architectural arrays on the surface

in the form of a localized nano/micro-volume system, which is predominantly prepared using soft lithography. The most notable aspect of this approach is that the configuration of the micro-volume system and the illuminating beam can be varied, which results in a vast range of distinctive complex 3D microarchitectures.

As the first illustration of the potential of this approach in general, Figure 1.6(A) summarizes a strategy to make intricate 3D features on the micropillars using a simple illumination scheme. In this study, a micropillar array that created preliminary using soft lithography is illuminated by a collimated beam with circular polarization (*33*). The application of the circular polarization beam results in the outward movement of mass in a uniform manner across all radial directions. Simultaneously, a field-gradient effect causes the upper layer of the micropillar to be driven at a significantly faster rate than the deeper layers (Figure 1.6(B)). This results in the formation of a mushroom-like 3D structure, as illustrated in Figure 1.6(C). This architectural type has been observed in nature, such as on the skin of the springtail insect (*8*), which can induce a superomniphobic effect (*33*).

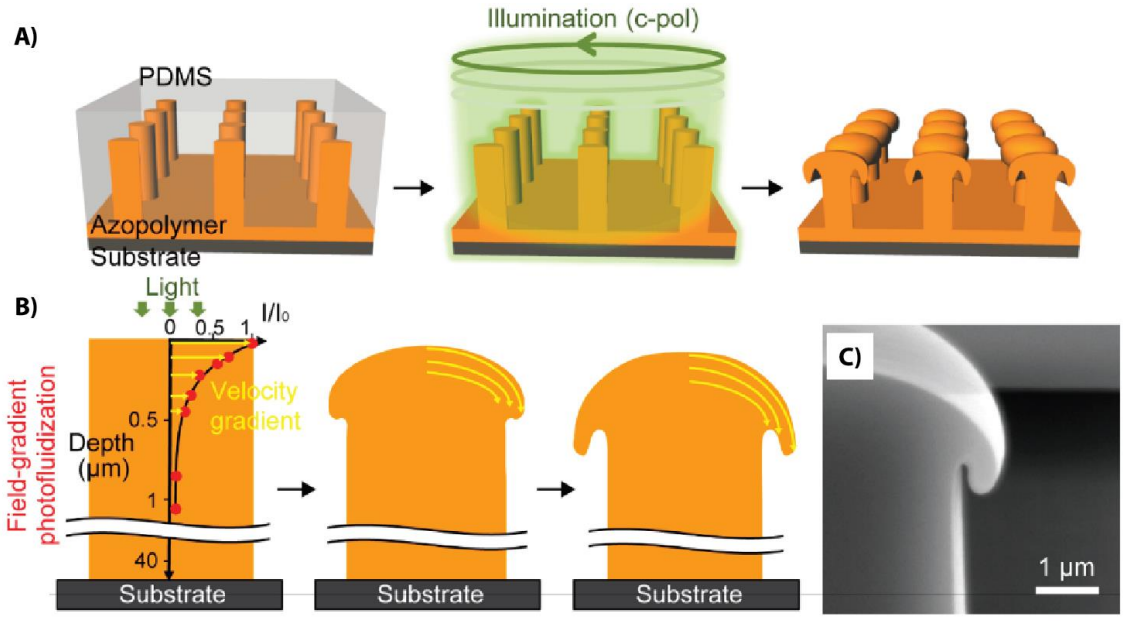

Figure 1.6 The mushroom-like microstructure fabrication. (A) The experimental steps from left to right: stamping micropillar with PDMS stamp, illumination of collimated beam with circular polarization, and the resulted mushroom-like microstructure array. (B) The illustration of field-gradient mechanism and its effect to the top of the micropillar, and (C) the SEM image of the mushroom-like architecture. (A–C) are adapted from (*33*) with permission with ACS Publications.

The primary phenomenon responsible for the formation of mushroom-like structures is the gradient-field effect, which arises from the exponential attenuation of light as it propagates within the volume of the azopolymer (Figure 1.6(B)). This results in a speed-gradient of photodeformation at different depths within the micropillars. Chapter 2 of this thesis employs this phenomenon as the foundation for developing a new lithographic parameter for controlling the three-dimensional architecture of micropillars. This study will expand upon the field-gradient effect by implementing variations in wavelength of light. As different wavelengths have varying penetration depths within the azopolymer volume, this variation will induce varying degrees of gradient-field effect, ultimately resulting in diverse three-dimensional microstructures.

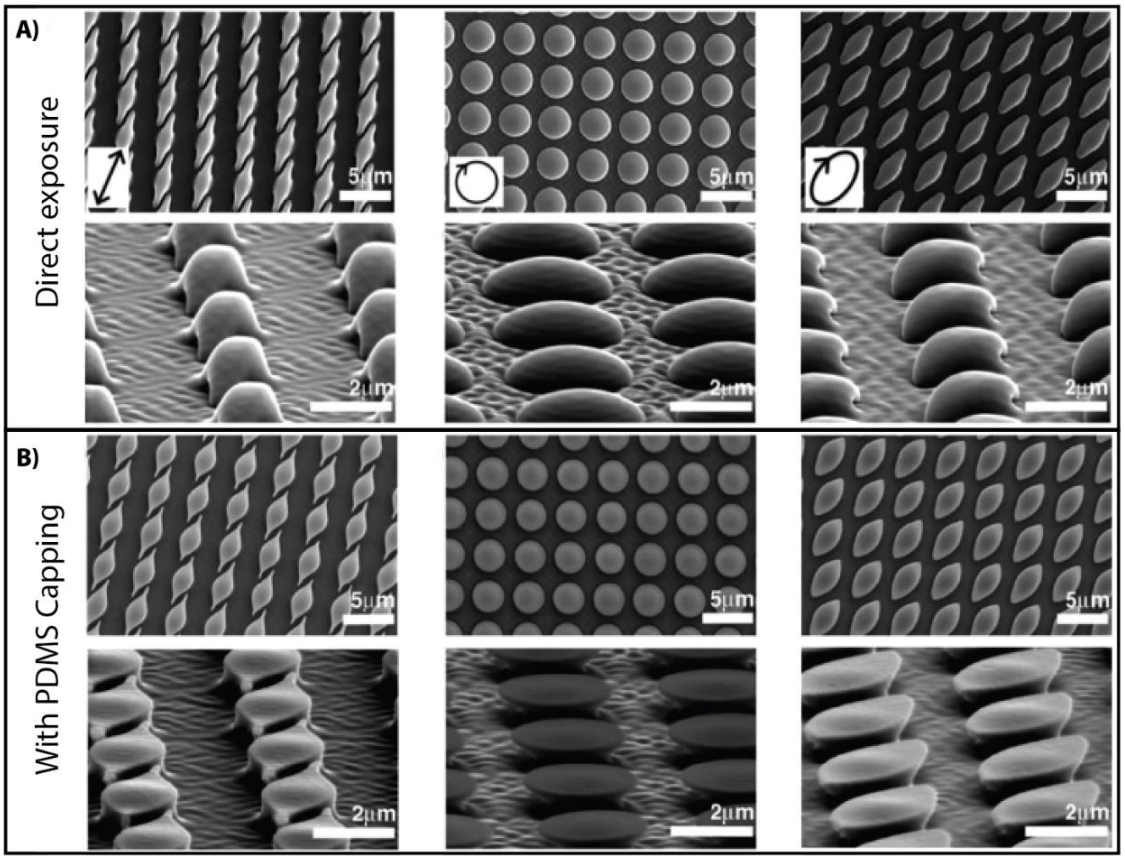

Figure 1.7 The effect of different polarization state to the deformation of the micropillar. (A) The top view and slant view of reshaped micropillars after an exposure of collimated beam with a linear, circular, or elliptic polarization (left–right). (B) The same case with (A) but with additional PDMS capping on top of the micropillar array during the illumination. (A–B) are adapted from (*34*) with permission from ACS Publications.

When a circular perimeter, such as that of cylindrical micropillars, is illuminated with circularly polarized light, the result is an architectural profile that is isotropic in lateral directions. It is possible to induce an anisotropic profile by exposing micropillars to a linearly or elliptically polarized beam. In general, the lack of circular symmetry of electric field components in the wavefront of the beam results in an unbalanced mass migration, which is predominantly driven in the direction of the largest electric field components. In their study, Lee *et al* (*34*) presented three general states of polarization in the beam and their effects on micropillars, as illustrated in Figure 1.7(A). These results demonstrate that the state of polarization can result in significantly different degrees of anisotropy in the final microarchitectures. Additionally, this study explored the effect of PDMS capping to constrain micropillar morphology during the reconfiguration. The addition of PDMS capping resulted in a flat top surface (Figure 1.7(B)), while the anisotropic shapes were similar to those observed in the absence of PDMS capping.

Another approach, while using the same experimental configuration as works reported above, focuses attention on the strong regime of the photodeformation. Rather than investigating the individual architectural characteristics of the micropillar, it focuses on reshaping individual micropillars to create a large surface with interconnected structures. An example is the approach that uses a linearly polarized collimated beam over a large area of the surface (*37*). The objective is to consider the direction of linear polarization in relation to the direction of the “lattice” within the 2D array of micropillars, and to expose the micropillar array for an extended period until they are merged (Figure 1.8(A)). Figure 1.8(B) illustrates the formation of a one-dimensional grating resulting from the merging of adjacent pillars along the polarization direction. This figure depicts the resulting diffraction patterns in the far field for various periodicities and relative directions of vector gratings. Another study also investigated the emergence of novel architecture from the initial structure following exposure to the beam. In the study conducted by Wang *et al* (*38*), a hexagonal configuration of micropillars was illuminated by a circularly polarized beam, as illustrated in Figure 1.8(C). In contrast to the conventional approach of stopping the exposure until the pillars have undergone reshaping, the illumination is maintained even after the pillars have almost flattened, losing their original shape. Intriguingly, throughout the illumination, there are multiple stages where the surface topology undergoes transitions into distinct formations, as illustrated in Figure 1.8(D). This approach offers a simplified fabrication process for producing diverse surfaces.

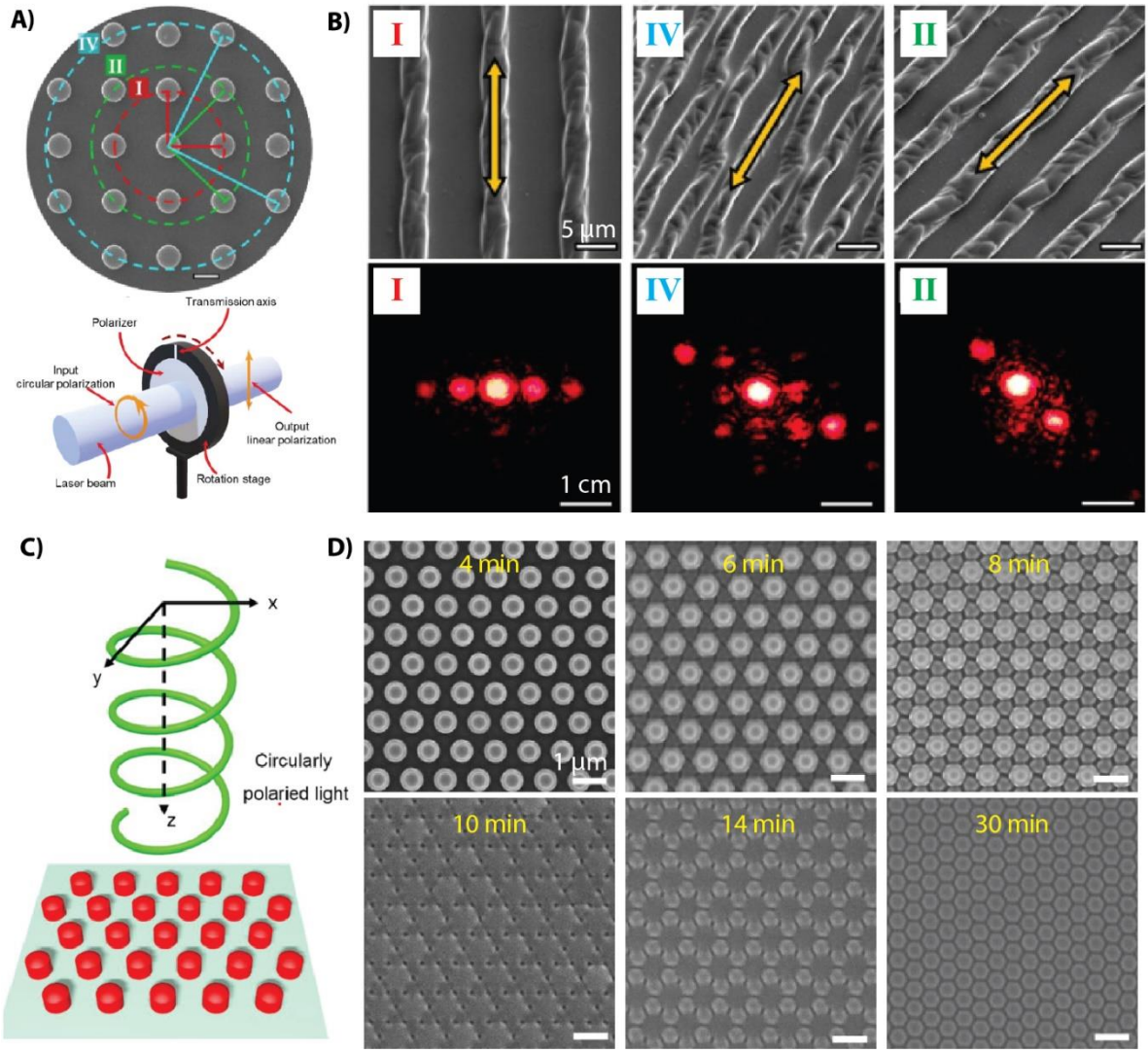

Figure 1.8 The interconnected reshaping of azopolymer-based micropillar array. (A) The experimental strategy of the reconfigurable anisotropic deformation. (B) the reshaped micropillar array coming from the exposure of collimated beam with different relative linier polarization orientations and their diffraction patterns in the far-field after challenged with a probe beam. (A–B) are adapted from (*37*) with permission from IOP Publishing. (C) The experimental setup for topographical transition. (D) The topographical transition of sub-micrometer pillar array at different time points. (C–D) are adapted from (*38*) with permission from Nature.

1.4.2 Unidirectional asymmetry in azopolymer-based micro-architectures

The directionality of mass migration can be harnessed to induce a robust asymmetric feature in the architectural configuration of the microstructures. The objective is to

configure the light field in such a way that the azopolymer-based microvolume is subjected to an imbalance in its photo-induced deformation.

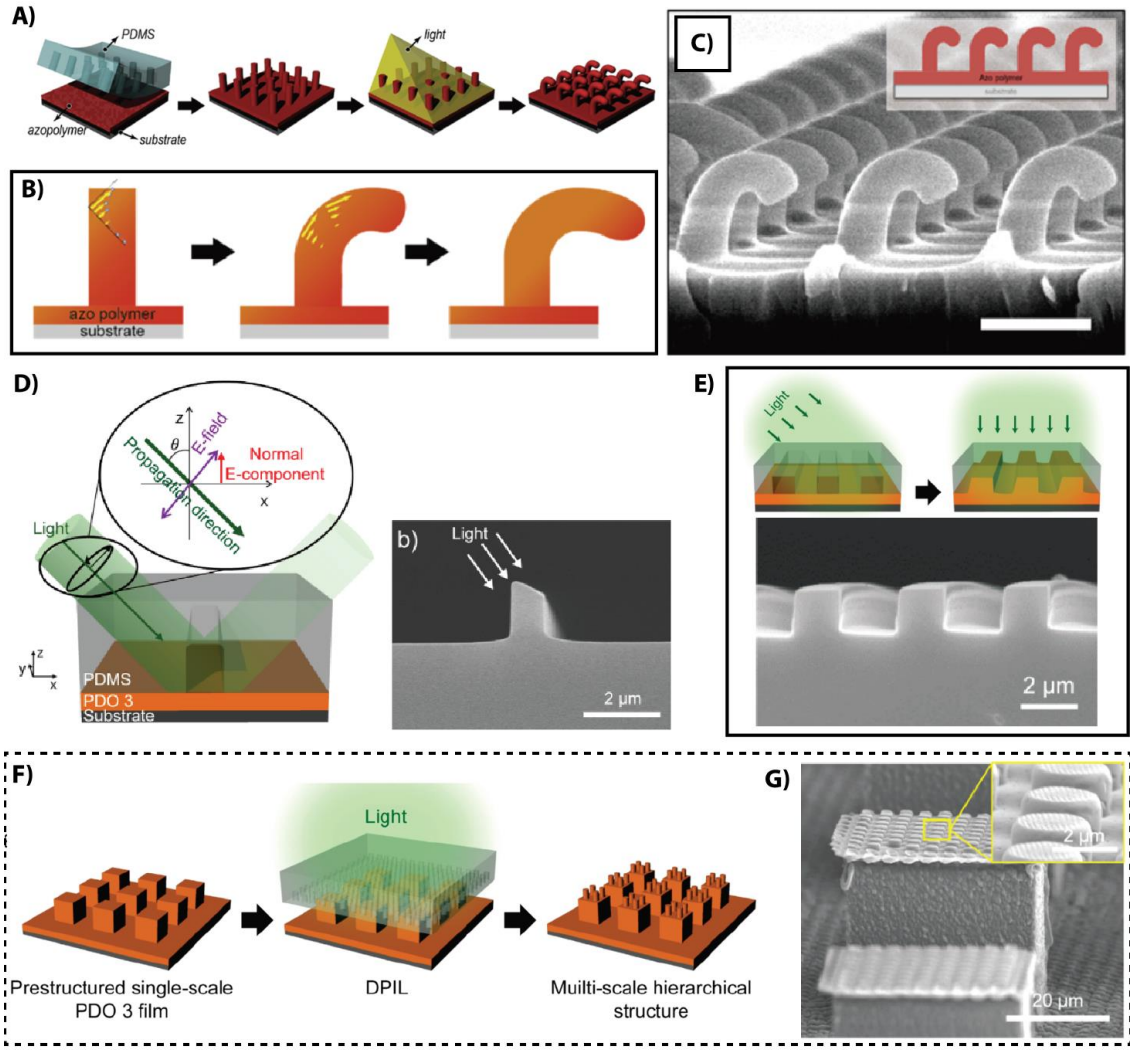

Figure 1.9 Unidirectional strategies for slant micropillars and assisting soft lithography. (A) The experimental setup to make bent micropillars with an exposure with slant beam. (B) The bending mechanism using an unbalanced directional deformation from one-sided exposure. (C) Side view of SEM image of the bent micropillar array. (A–C) are adapted from (*36*) with permission from ACS Publications. (D) The basic concept of vertical-directional mass migration on the azopolymer surface. (E) double-step exposure to achieve a flatten top surface of microstructures. (F) The multi-step strategy and (G) the morphology of microstructures with 3-level hierarchy. (D–G) are adapted from (*56*) with permission from ACS Publications.

Some studies have implemented this concept using a slant beam configuration, whereby the pre-existing microstructure is subjected to a unidirectional driven force by the light

(*32*, *34*, *36*). The initial example is the fabrication of bent micropillars with a slant linearly polarized beam, as illustrated in Figure 1.9(A). The underlying concept of the formation of the bent architecture is the elongation of one side of the micropillar due to the one-sided exposure, with a polarization component direction aligning with the longitudinal axis of the micropillar, as illustrated in Figure 1.9(B). The resulting bent micropillar array is illustrated in Figure 1.9(C). In comparison to conventional lithography, the fabrication of this distinctive "overhanging" three-dimensional (3D) architecture with pronounced asymmetry necessitates the utilization of a 3D-building-capable technique, such as direct laser writing. This approach is often characterized by prolonged processing times and elevated costs.

1.4.3 Light assisted-soft lithography

The directionality of polarization-dependent mass migration in azopolymers can be used in different manner that what discussed so far. It can be used to assist the conventional soft lithography to directly stamp microstructures on the surface from a solid film surface. The key concept is to illuminate the PDMS-azopolymer film system at an oblique angle, rather than impinging upon them from the normal direction, as summarized in Figure 1.9(D–G). This process involves a component of polarization along the longitudinal axis of the mold, which drives the mass to migrate and fill the template, as illustrated in Figure 1.9(D). The initial exposure successfully induced the material to fill the template, but it has a slanted profile on top originated by the tilted illumination. To achieve a final structure that resembles the square profile of the template, a second exposure from the normal incident angle can be employed to level the surface (Figure 1.9(E)). As the light-induced mass migration is not permanent, it is possible to induce multi-level hierarchical microstructures directly onto pre-existing microstructures, as illustrated in (Figure 1.9(F–G). One potential application of this hierarchical structured surface is the regulation of wettability and the self-cleaning effect (*56*).

1.4.4 Other optical and surface design strategies

While the abovementioned studies focused on reshaping positive micro-architectures on the surface, mass migration can also be used to reshape negative micro-architectures on the surface. For example, an array of micro-truncated nano-cones was employed as the initial pattern prior to illumination (*39*). The illumination of a homogeneous beam with circular polarization causes the edge of the nano-cone to move laterally towards the center of the nano-cone. As a consequence of the field-gradient effect, only a portion of

the nano-cone underwent reshaping, resulting in the formation of a distinctive 3D architectural structure, reminiscent of “nano-pottery”. The study demonstrated the functionality of this kind of surface by coating it with nanogold layer. The nano-pottery thus formed became a nano-trap that produced a gold-nanopad on the base of the nano-pottery. This kind of surface can be used to confine light in a deep-subwavelength region (*39*).

Further modifications to the illumination scheme can be incorporated to increase the complexity of the final 3D architecture. In contrast to the conventional beam with homogeneous polarization, an interference pattern derived from a two-beam system can be utilized to induce a grating–like formation on the microstructures. In a related study, Jo *et al* (*35*) implemented a slant interference light with periodically rotating polarization, generated by superimposing a right-circularly and a left-circularly polarized beam. This illumination can impart a denticle architecture, which is typically found on shark skin, and it is used for introducing a low–drag effect into the surface (*35*). Other architectures that have been studied include microspheres (*41*, *57*) and breath figures (*42*).

1.5 Azopolymer Synthesis and Fabrication of Pre-structured Surface

As stated in Introduction, the main parts of this thesis (Chapter 2–Chapter 4) will explore the same principle as most of the work reported above, that is to use the pre-structured azopolymer surface for the material system. Hence, this paragraph will give a summary of the basic concept and experimental procedures from synthesizing the azopolymer used in this thesis to fabricating the pre-structured azopolymer surface.

1.5.1 Synthesis of azopolymer

The azopolymer used thorough this thesis is a side-chain covalent azopolymer, which forms amorphous thin films when spin-coated or deposited by drop casting and soft molding on glass substrates. Its chemical structure is illustrated in the inset of Figure 1.10. The synthesis of the azopolymer was carried out by the group of Prof. Fabio Borbone - Department of Chemical Sciences, University of Naples "Federico II", with whom I collaborated throughout the Ph.D. program. The synthesis includes radical polymerization of the monomer (E)-2-(4((4-methoxyphenyl)diazenyl)phenoxy)ethyl acrylate that has photoresponsive property, following the established procedure (*58*). In summary, (E)-2-(4((4-methoxyphenyl)diazenyl)phenoxy)ethyl acrylate (1.00 g, 3.06 mmol) and 2,20-azobis(2-methylpropionitrile) were dissolved in 4 ml of N,N-

dimethylformamide in a vial that was sealed under vacuum after three cycles of freezing and thawing. The solution was maintained at 70°C for 48 hours and then transferred into 100 ml of methanol. The polymer was filtered, washed with methanol, dissolved in chloroform, and precipitated in hexane. Additional physicochemical properties, including the molecular weight and thermal analysis of this azopolymer, can be found in ref (*32*).

1.5.2 The fabrication of pre-structured azopolymer surface

The pre-structured pattern on azopolymer surfaces is typically prepared using soft lithography, whereby a PDMS stamp containing a negative pattern of the intended microstructures is employed. Figure 1.10 summarizes general workflow of transferring the negative version of the intended microstructures from a PDMS stamp to the surface of the azopolymer film. In general, the stamping process starts with the deposition of a few drops of azopolymer solution on a substrate. A PDMS stamp then is gently placed onto the azopolymer solution, forming a sandwich of PDMS/azopolymer/substrate. This allows the solution to infiltrate and fill the negative pattern on PDMS surface. After a drying process which is typically done by letting the solvent of the azopolymer solution completely evaporate, the PDMS stamp then can be peeled mechanically. After this final step, the azopolymer film with microstructures array is obtained.

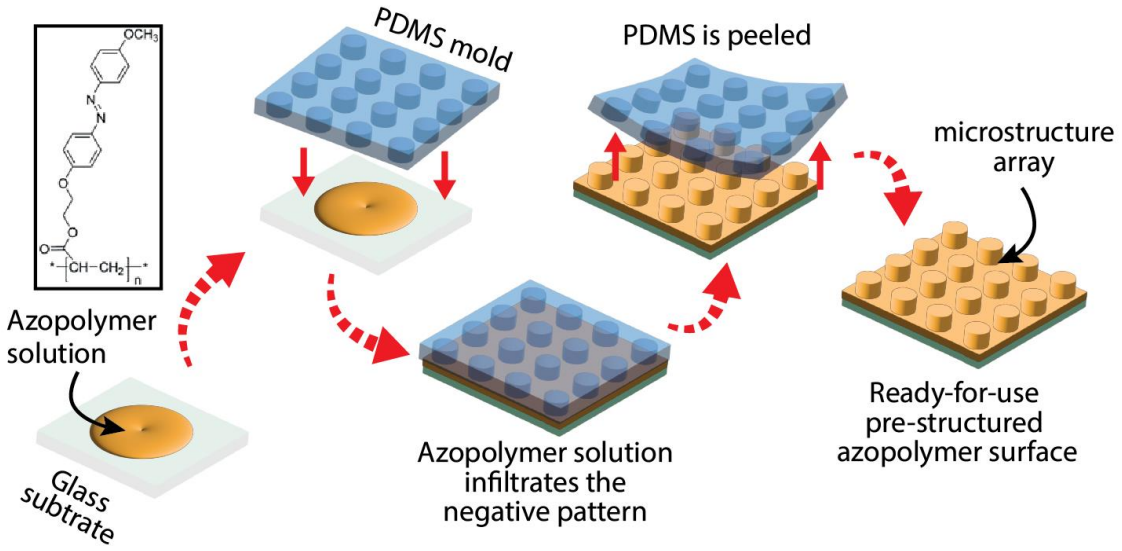

Figure 1.10 The chemical structure of azopolymer used in this thesis and the typical procedure to fabricate pre-structured azopolymer surface using PDMS-based soft lithography.

In detail, the initial step involves the creation of a PDMS stamp with a negative pattern of the surface in accordance with the desired configuration. A silicon wafer with a cylindrical micropillar array arranged in a square lattice (with designed height (*h*), diameter (*d*), and pitch (*p*) depending on the specific need in the experiments) was utilized as the master template for the molding process. Prior to use, the silicon wafer was subjected to an anti-stick treatment, whereby its surface was exposed to silanizing vapors (trichloro(1 H,1 H,2 H,2 H-perfluorooctyl)) for a period of 90 minutes at a temperature of 125°C within an airtight glass container. Subsequently, the container was left open for an additional 90 minutes at 150°C to facilitate the removal of residual vapor. The PDMS utilized for mold fabrication was prepared by blending the elastomer (Sylgard 184, Dow Corning) with a curing agent in a 10:1 weight ratio and subsequently placed in a vacuum chamber to remove the air that had become entrapped in the mixture during the blending process. The resulting mixture was then gently poured onto the silicon wafer and cured at 80°C for a period of two hours. Finally, the solidified PDMS was carefully detached from the wafer, thereby obtaining the negative pattern of the micropillar array.

In the next step, the negative pattern on the PDMS stamp can be transferred onto the azopolymer surface by following the specified procedure. A small quantity of a 10 wt% solution of the azopolymer in 1,1,2,2-91 tetrachloroethane was applied to a clean coverslip, and the PDMS mold was then placed on top of the solution drops, allowing the solution to fully spread into the negative pattern of the micropillar array. The system was then left at room temperature for a period of five hours to allow for the complete evaporation of the solvent through the micropores of the PDMS mold. Finally, the mold was carefully detached, resulting in the formation of the desired micropillar array pattern on the azopolymer film surface.

2 Wavelength as New Lithographic Parameter:

Wavelength-dependent penetration depth to regulate three-dimensional architecture in azopolymer-based microstructures

The emergence of strategies to achieve intricate three-dimensional architectures using azopolymer is primarily driven by the peculiar directionality (polarization dependence) of light-induced mass migration. The directional reshaping of the azopolymer allows for its deformation to be driven in any direction in space with high accuracy. In practice, the directional mass migration is constrained by two principal factors: the ability to engineer the field of light (i.e., the polarization distribution and direction), and the azopolymer-based material system. Paragraph 1.4 in the previous Chapter provides a comprehensive overview of the diverse strategies that employ pre-patterned azopolymer-based microstructures as the initial state, along with various illumination configurations. These strategies aim to drive local mass migration in different relative directions within three-dimensional space (see Figure 1.6 - Figure 1.9). The results are noteworthy, as these works have succeeded in achieving intricate micro-architectures that would otherwise require expensive, intricate, and time-consuming techniques.

A closer look at the reported literature reveals that the gradient-field effect, which arises due to the high absorbance of azopolymers, has the potential to produce complex functional three-dimensional architectures. The study that has investigated this phenomenon in micropillar array is the use of circularly polarized light to produce mushroom-like micro-architecture array (see Figure 1.6 from ref (*33*)). The practical concept of the gradient-field effect is that the light-induced mass migration on azopolymer-based microvolumes is most intense in the top layer and gradually diminishes in a deeper layer of microvolumes. The reduction in light intensity when propagating along the longitudinal axis of the azopolymer-based microvolume is the primary factor contributing to the formation of a robust overhanging feature, wherein the top part of the microstructure is wider than the bottom part. Nevertheless, only a limited number of studies have investigated this phenomenon more in-depth, with the objective of producing complex and controllable three-dimensional features on their microstructures.

This chapter presents the study that aims to further exploit the field-gradient effect in the reconfiguration of azopolymer-based microstructures. However, this study elevates the concept by introducing wavelength of light as the new lithographic parameter to have an additional control for three-dimensional architectures. In general, different wavelengths have different penetration depths (roughly describing how far the light can propagate inside a material volume). Consequently, different wavelengths will induce different levels of field-gradient effect on azopolymer-based microvolumes. The objective of the study presented in this chapter is to introduce the wavelength of light as a new lithographic parameter and to investigate how the variation of wavelength can trigger different 3D microarchitectures. The results included in this Chapter are used as the basis for the paper "I. K. Januariyasa, F. Borbone, M. Salvatore, S. L. Oscurato, Wavelength-Dependent Shaping of Azopolymer Micropillars for Three-Dimensional Structure Control. *ACS Appl. Mater. Interfaces* 15, 43183–43192 (2023)".

2.1 The Penetration Depth of Light in Azopolymer

2.1.1 Azopolymer film fabrication

In order to study the absorbance of the azopolymer, a series of films with varying thicknesses were prepared via spin coating the polymer solutions in 1,1,2,2-91 tetrachloroethane onto glass slides. The azopolymer used in the making of this film is described in Chapter 1.5.1. The concentration and rotation speed of the polymer solution were varied in order to produce films of different thicknesses, with the concentration ranging from 80 mg/mL and 2500 rpm to 180 mg/mL and 300 rpm.

2.1.2 The penetration depth of light inside azopolymer bulk volume

Prior to applying the variation of wavelength to the pre-structured azopolymer surface, it is essential to conduct a thorough study on the attenuation of light of diverse wavelengths as it propagates within the bulk volume of flat azopolymer films of varying thicknesses. This will serve as the foundation for the subsequent design of the experiment, which will utilize an azopolymer-based pre-patterned micro-volume surface.

Figure 2.1(A) illustrates the absorption spectrum of the azopolymer within the ultraviolet-visible range (wavelengths between 300 and 600 nm) as measured by a spectrophotometer (Jasco V560). The absorption of the azopolymer is entirely determined by the optical properties of the embedded azobenzene molecules. It exhibits a broad maximum centered around 350 nm and decreases to negligible values above

600 nm, where the polymer becomes essentially transparent. The considerable variations in absorbance for light with wavelengths ranging from UV (300 nm) to green (550 nm) indicate notable alterations in the depth that light can penetrate within the volume of the film before being fully absorbed. This phenomenon is elucidated by the well-established Bouguer-Lambert-Beer (BLB) law (*59*). According to this law, the intensity *I(z)* of the light that is transmitted from the surface (at $z = 0$) to a depth z within the azopolymer film is diminished as follows:

$$I(z) = I_0 e^{-\frac{z}{\delta}} \tag{2.1}$$

where I_0 represents the intensity at the surface, while δ denotes the penetration depth. The latter defines the location where the incident light intensity is reduced by a factor of *1/e*, approximately equal to $0.37I_0$. Given that the penetration depth is directly linked to the absorption coefficient $\alpha = \alpha(\lambda)$ of the dispersive material, it is evident that the penetration depth $\delta = \delta(\lambda)$ is also wavelength-dependent, with $\alpha(\lambda)$ and $\delta(\lambda)$ denoting the absorption coefficient and the penetration depth at a given wavelength λ, respectively.

In the present study, four discrete wavelengths were selected for investigation: λ_{375} = 375 nm, λ_{405} = 405 nm, λ_{488} = 488 nm, and λ_{532} = 532 nm. These are highlighted in the spectrum curve in Figure 2.1(A). These wavelengths span the majority of the non-negligible absorption region of the azopolymer spectrum, allowing for a comprehensive investigation of the impact of light penetration depth ($\delta(\lambda)$) on the final 3D architecture of reshaped azopolymer-based microstructures.

In investigating the extrapolation of $\delta_i \equiv \delta(\lambda_i)$ of the azopolymer at the four wavelengths λ_i, the UV-vis transmittance spectra $T(d) = I(d)/I_0$ of flat azopolymer films were measured across a range of thicknesses (0.3-6.0 µm) to obtain a comprehensive representation of the data. The transmittance spectra were acquired using a PerkinElmer Lambda 900 spectrophotometer. The results are presented as colored dots in the plot of Figure 2.1(B) for each λ_i. The corresponding penetration depths, δ_i, were obtained by fitting the data with respect to the film thickness with a negative exponential function (dashed lines in Figure 2.1(B)), according to the BLB law in equation (2.1). The values of δ_i are presented in Figure 2.1(C), accompanied by a quantitative graphical visualization of the light attenuation in the azopolymer volume, which allows for a direct comparison of the different behaviors in the exponential intensity decay upon propagation across the investigated wavelength range.

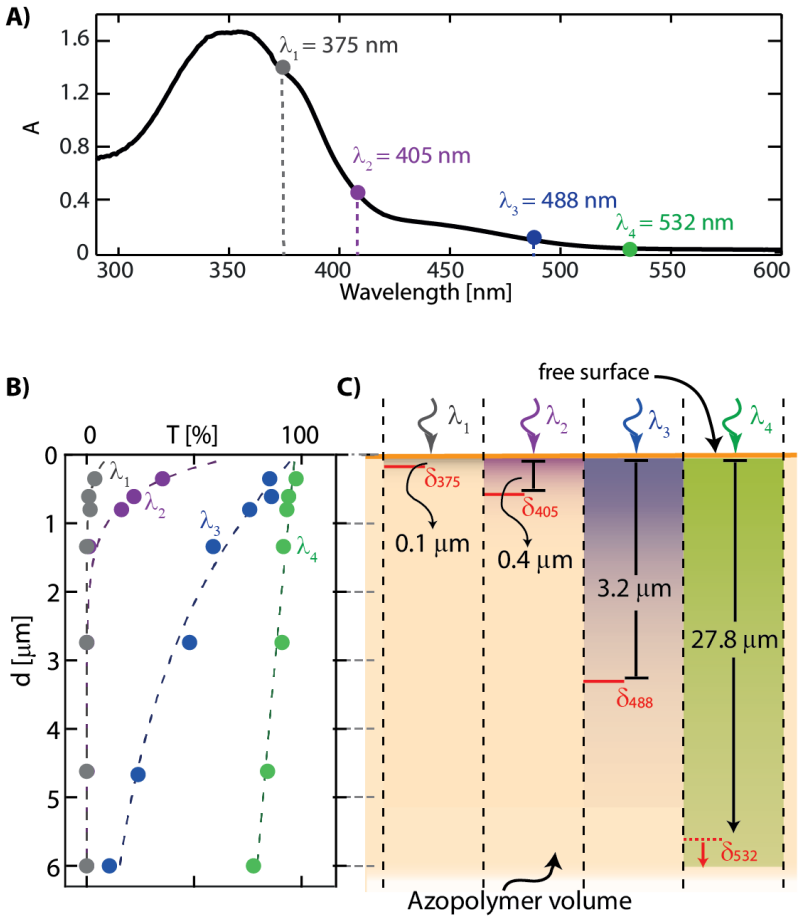

Figure 2.1 UV-Visible spectra and penetration depth analysis on bulk azopolymer. (A) UV-Visible absorbance spectrum of the azopolymer and the inset image of its chemical structure. (B) transmittance values measured (dots) at the selected wavelengths for different azopolymer film thicknesses *d*. Dashed lines are the result of data fitting with the BLB law. (C) Illustration of the different penetration depths of light at the selected wavelengths in the azopolymer volume.

As hypothesized, the analysis demonstrated considerable variations in the penetration depths. The light with a wavelength of 375 nm (UV) exhibited the smallest penetration depth among the tested wavelengths, with an estimated fitted depth of approximately 0.1 µm. In contrast, the wavelength of 532 nm (green laser) demonstrated a markedly different behavior, with a penetration depth of 27.8 µm. The difference in penetration depth between these two wavelengths reached two orders of magnitude, indicating that they could induce significantly different effects when applied to the azopolymer-based microvolume.

2.2 Penetration Depth as a Parameter for Controlling the 3D Architecture

The next phase of the study will entail an analysis of the impact of varying penetration depth on the three-dimensional architecture of an azopolymer microvolume. As previously discussed in Chapter 1, particularly in Section 1.4, the effective photo-reconfiguration of azopolymer-based microvolumes relies on two essential conditions. The first requirement is an irradiation configuration with a polarized light field that has a vectorial component in the plane of one of the microvolume surfaces. The second is the presence of discontinuity on the surface, which means dealing with localized microvolumes. This allows for the observation of global deformation of the azopolymer microvolume along the direction of light polarization. The configuration achieves maximum deformation efficiency when the polarization direction is orthogonal to the boundaries of the microvolumes.

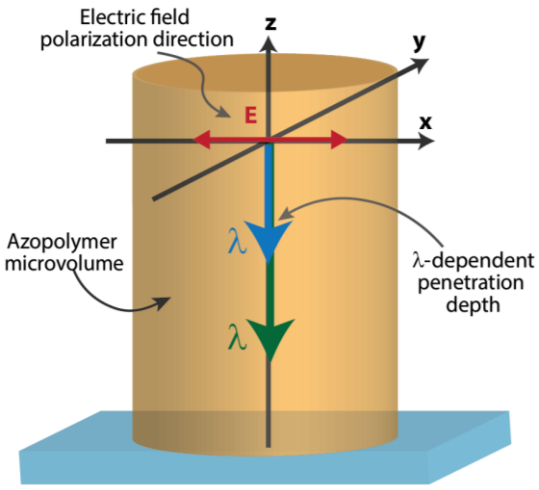

Figure 2.2 Scheme of the 3D reshaping of an azopolymer microvolume using different wavelengths of light irradiation. The electric field, oscillating in the x-axis, can propagate to different wavelength-dependent positions in the z direction, triggering the pillar reconfiguration from different depths in the microvolume.

The two aforementioned conditions are typically met in the experiments by irradiating an array of azopolymer-based microstructures with linear or circular polarized light at normal incidence, resulting in lateral deformation of the top surface (on the *x-y* plane) of the microvolume. The schematization of this process is illustrated in Figure 2.2. While previous studies have focused on varying the polarization states and incidence angle to achieve additional control, this study incorporates the penetration depth of light as a

newly introduced lithographic parameter. The consequence of a wavelength-dependent penetration depth is that different wavelengths can reach varying depths within a microvolume, thereby inducing distinct deformations in the azopolymer-based microvolume. From a practical standpoint, the impact on the final 3D architecture is in direct correlation with the wavelength of irradiated light.

2.2.1 The optical setup and the fabrication of pre-patterned micropillars

To quantify the influence of light wavelength on the three-dimensional configuration of azobenzene microvolumes, an experiment was devised by adapting the methodology illustrated in Figure 2.2. Four distinct and co-propagating diode lasers at the wavelengths λ_i were employed to irradiate a pre-patterned azopolymer surface (375 nm (Oxxius LBX 375), 405 nm (Coherent OBIS 405 LX), 488 nm (Coherent OBIS 488 LS), 532 nm (Laser Quantum Opus 532). The collimated beams from each laser passed through a broadband quarter-wave plate and a fixed linear polarizer, subsequently impinging orthogonally on the sample plane with a linear polarization in the x-direction. The optical setup is illustrated in Figure 2.3(A), wherein the various lasers utilized in the experiment are depicted, for simplicity, as a single wavelength-switchable laser. The intensities of the lasers were adjusted to account for the significant variation in deformation dynamics resulting from the azopolymer's total light absorption at different wavelengths. The intensities measured at the sample plane were as follows: I_{375} = 90 mW/cm², I_{405} = 70 mW/cm², I_{488} = 160 mW/cm², and I_{532} = 4 W/cm². Each irradiation experiment was conducted with collimated beams of approximately 4.0 mm in diameter. The light-induced reconfiguration experiments were performed by exposing identical films with the prepatterned micropillar surface to each wavelength λ_i. Throughout the experiment, the polarization and the angle of incidence were maintained constant, while the exposure dose was increased to obtain tunable degrees of deformation in the direction of the light polarization.

The preparation of the prepatterned azopolymer surfaces was achieved through the fabrication of a square array of cylindrical micropillars via standard soft lithography (see Chapter 1.5.2). A micropillar template with a height of H_0 = 10 µm was selected for investigation of scenarios where the penetration depth was significantly shorter, comparable, or much longer than the initial height of the microvolumes. The pillar diameter and the array periodicity were 5.0 µm and 10.0 µm, respectively.

2.2.2 The wavelength-dependent 3D micro-architectures

Based on the ratio of the pristine height H_0 (approximately 10 µm) of the azo micropillar to the measured penetration depths δ_i, at least three distinguishable architectural families of deformed microstructures are expected to emerge, as illustrated in Figure 2.3(B). The penetration depths of λ_{375} and λ_{405} (0.1-0.4 µm), λ_{488} (3.2 µm), and λ_{532} (27.8 µm) can be considered relatively "very short", "medium", and "very long" with respect to the micropillar height, respectively. This categorization provides a straightforward predictive tool for the final micropillar architecture. The distinctive three-dimensional morphologies of these structures are determined by the different fractions of the original volume that can move effectively under irradiation with different wavelengths.

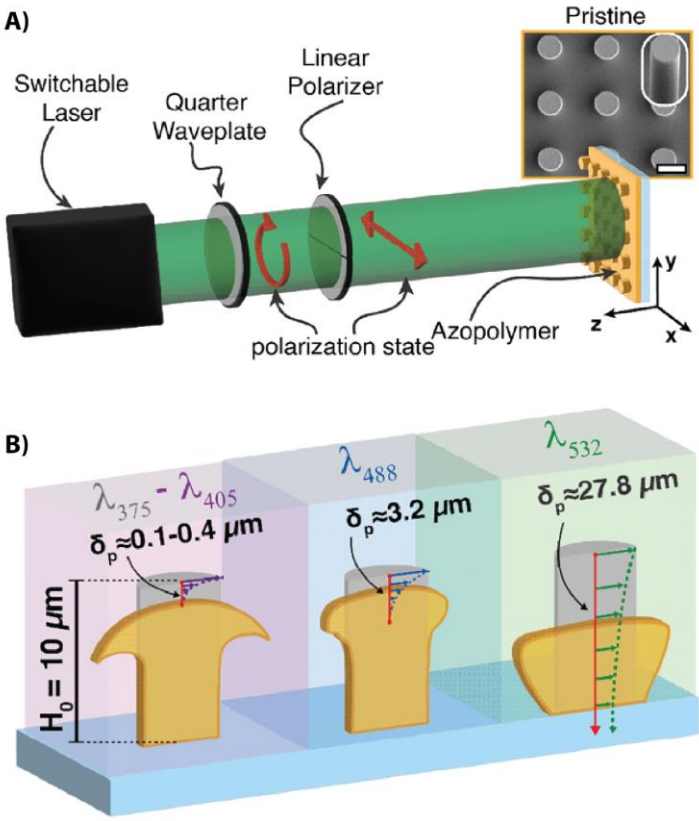

Figure 2.3 The irradiation setup and the morphology of the reshaped micropillars at selected wavelengths. (A) Irradiation scheme of the experiment. The top and side view SEM images in the inset show the morphology of the pristine surfaces used in the experiment (scale bar = 5 µm. (B) Qualitative illustration of the decaying intensity profiles of the selected wavelengths and their effect on the 3D geometry of the reconfigured pillars.

To demonstrate the applicability of this straightforward reasoning to a real physical system, a series of characterizations were conducted on the surface morphology of the samples after exposure using a scanning electron microscope (SEM, FEI Nova NanoSEM 450), as shown in Figure 2.4(A–B). As anticipated, exposure to light resulted in the formation of asymmetric structures exhibiting elongation along the direction of polarization. Figure 2.4(A) shows that the increase in exposure time led to greater surface elongation, although the observed projected in-plane (*x*–*y*) morphology remained substantially similar across the tested wavelengths. This behavior has been employed in several studies that aimed to produce light-induced anisotropic microstructures on the azopolymer surface. For example, in reference (*37*), the focus of the this study is to reshape the micropillar array until they are merged and form a new interconnecting morphology on the surface. This type of strategy does not put the three-dimensional architecture of the final structure as the main attention.

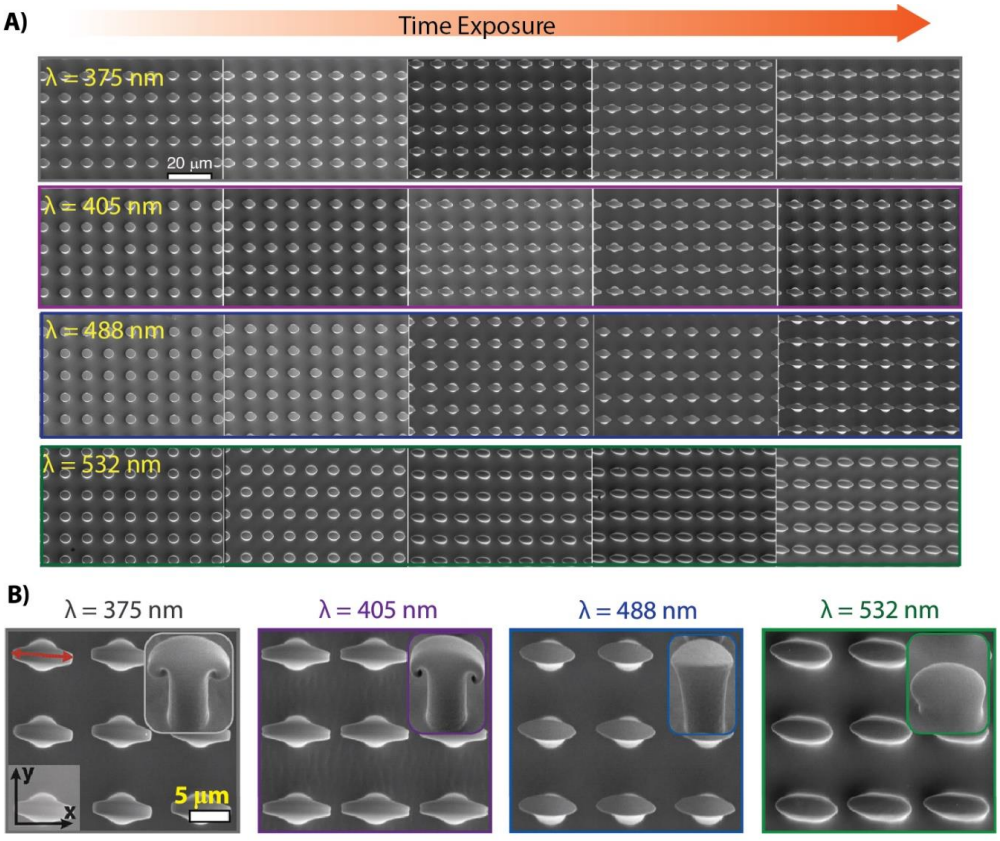

Figure 2.4 The morphological analysis of the reshaping micropillar array. (A) The evolution of *x-y* projection view of the reshaped micropillar array as the function of the exposure time. (B) SEM images of the top view of the reshaped micropillars at the selected wavelengths. The red arrow in the first panel indicates the direction of light polarization. The insets show the side view of a corresponding micropillar.

However, the scanning electron microscopy (SEM) side views of the micropillars in the insets of Figure 2.4(B) demonstrate significantly divergent three-dimensional architectures, in agreement with the hypothesis presented in Figure 2.3(B). In particular, the λ_{375} and λ_{405} treatments yielded comparable three-dimensional micropillar structures with a pronounced overhanging aspect. For these two sets of microstructures, the deformation was observed to occur exclusively in a region around the top surface of the micropillars, resulting in a curled shape on both sides of the microstructure, which became evident after a relatively brief exposure dose. The structures irradiated at λ_{532} exhibited markedly disparate results. In this case, the photodeformation involved the whole micropillar volume, giving rise to shorter and larger micropillars elongated in the *x*-direction, even at the bottom level. Finally, light at λ_{488} induced a relatively intermediate 3D deformation regime, involving the migration of a considerable portion of the initial microvolume while maintaining a distinct cylindrical structure at the bottom level.

2.2.3 Quantifying the evolution of the 3D micro-architectures

To grasp the idea of the controllability of the final architectural configuration, a set of measurable geometric parameters (p, h, l_b, β, and γ) were conceived, as collectively described in Table 2.1 and illustrated Figure 2.5. These parameters have been designed in order to capture the essential features of the different photo-reconfigured microstructures. Each of these parameters can be measured from the SEM images, and their geometrical meaning will be discussed individually below.

Parameter	Definition
Height	
H_0	The original height of the pristine micropillar
H	The height of the reshaped micropillar measured from the base level to the highest point in the structure
h	The height ratio of deformed micropillar to the original one (H/H_0)
P	The height of the micropillar's fraction that is unaltered, measured from the base to the highest point of unaltered micropillar

p	The ratio of the unaltered height to the total of the original micropillar (P/H_0)
Base Diameter	
L_0	The original base diameter of the pristine micropillar
L	The base diameter of the reshaped micropillar
l_b	The ratio the reshaped base diameter to the pristine one (L/L_0)
Ellipse of the top view	
L_M	The major axis of the ellipse from the top view projection of the micropillar
L_m	The minor axis of the ellipse from the top view projection of the micropillar
A	The ratio of the major to the minor axis of the ellipse from the top view projection of the micropillar (L_M/L_m)
The angle of curvature	
β	The deflection angle of the deformed micropillar in the top layer
γ	The curling angle feature happening in deformed layer of the micropillar

Table 2.1 The summary of the geometrical parameters and their definitions

It is noteworthy that in the experiments only the exposure dose was varied in order to achieve a gradual increase in the microvolume deformation. The significant discrepancies in the total light absorption of the azopolymer resulted in markedly disparate deformation dynamics across the various wavelengths. To ensure the reliability of the comparative analysis, all geometric parameters were subsequently examined as a function of the *x*-*y* strain (A) of the top surface, which was calibrated to lay within the same range for micropillar reconfigured at all the used wavelengths. The strain A was calculated from the top view SEM images as the ratio of the major axis L_M to the minor axis L_m of the approximately elliptical top region of the deformed micropillars (Figure 2.6(A)). This approach enables the direct attribution of the differences in the three-dimensional morphology of the photodeformed structures with

similar in-plane anisotropy to the light penetration depth of each wavelength, independent of the temporal dynamics required to induce deformation.

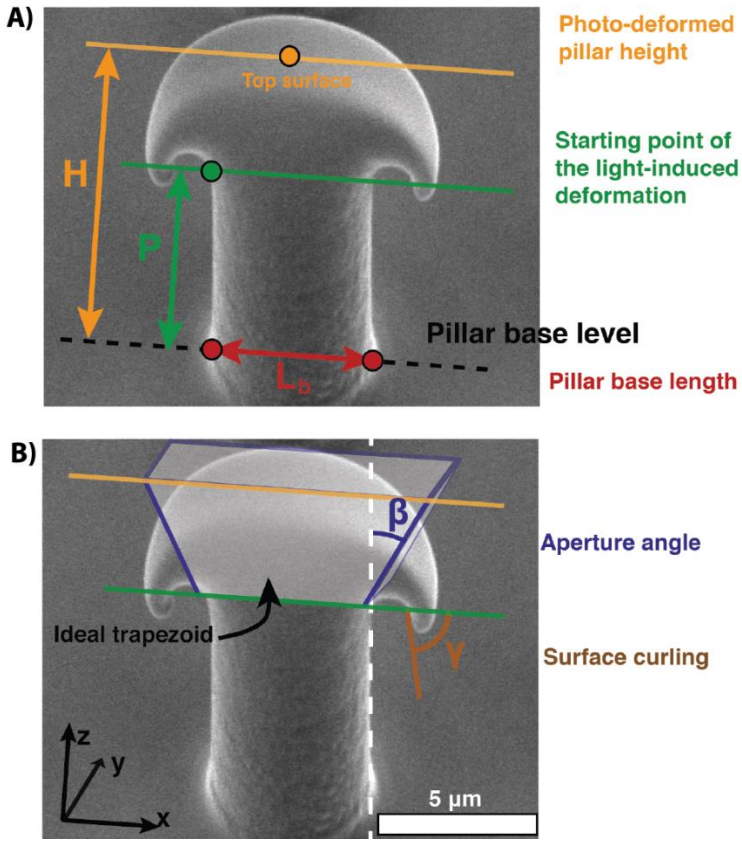

Figure 2.5 The visualization of the geometrical parameters in the real micropillar image, for (A) the length-based parameters (H, P, and L_b) and (B) the angle-based parameters (β and γ).

Parameter p: The residual fraction of micropillars

The physical meaning of the parameter p is to quantify the depth at which light exerts an effect on the micropillar's volume at different time points. The parameter p is geometrically defined in Figure 2.6(A) (see also Figure 2.5 and Table 2.1), which characterizes the fraction of the volume of the original cylindrical micropillar that remains undeformed during the photo-reconfiguration process. It is measured as the ratio of the distance from the pillar base in the vertical direction where the light-induced deformation is initiated (P) to the pristine pillar height H_0 ($p = P/H_0$).

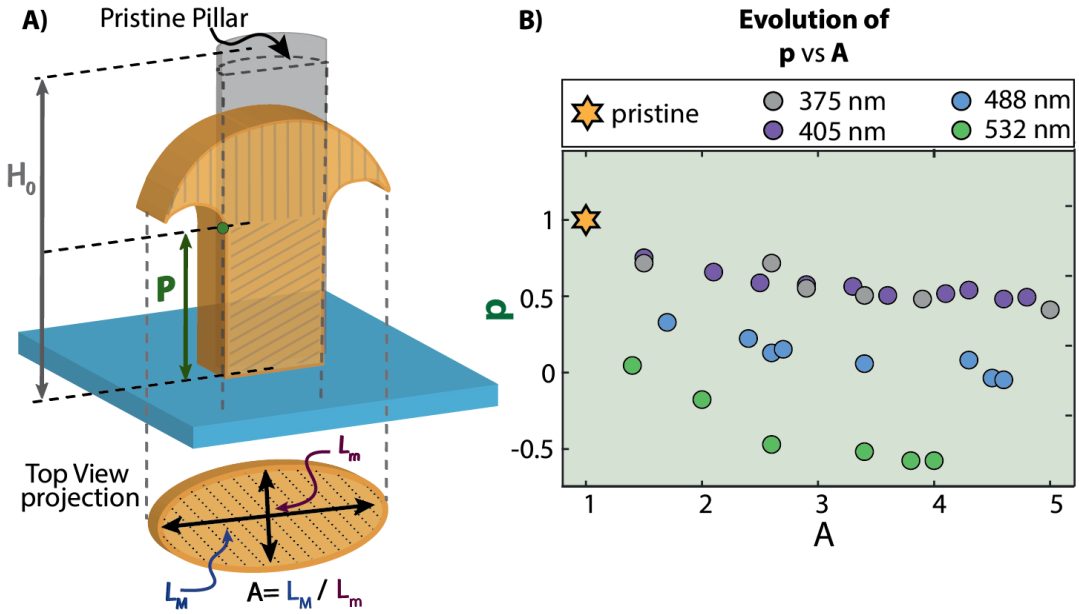

Figure 2.6 Geometrical parameter *p*. (A) The artistic visualization of *p* and (B) its evolution as the function of *A*

From a physical standpoint, the value of p ≈ 1 indicates that only a minor portion of the original volume is deformed, whereas a value approaching 0 implies that the entire original structure has undergone a significant reconfiguration. In the experimental phase, the distance *P* was determined from side-view SEM images by identifying the point of intersection (illustrated by the green dot in Figure 2.6(A) and see further in Figure 2.6(A)) of a line drawn tangent to the lateral pillar surface in the deformed region and the vertical direction. Consequently, *p* can assume negative values, indicating that the intersection point occurs at a position beneath the base of the pristine micropillar.

Figure 2.6(B) demonstrates the evolution of parameter *p* with varying wavelengths λ_i, as a function of pillar strain *A*. Despite the differing dynamics, the analysis reveals a consistent decreasing trend for *p* with increasing *A* observed across all wavelength variations. This finding is a direct consequence of the markedly different light penetration depths and the approximate volume conservation inherent to the light-induced reconfiguration process of azopolymers, which has been reported in literatures (*18*). As the material layers in proximity to the top surface migrate laterally along the electric field direction, the underlying layers within the micropillar volume can be reached by the previously absorbed light, which then initiates movement. This enables the light to penetrate deeper into the micropillars as the exposure continues, resulting in further deformation of the deeper layers, which are identified by a reduction in *p*.

In particular, the evolution of the parameter p at varying λ_i verifies the qualitative morphological assessment illustrated in Figure 2.6(B). The reconfiguration of the pillars at λ_{375} and λ_{405}, both of which exhibit a light penetration depth of less than 5% of the initial height of the azo microvolume, results in a slow downhill trend, as illustrated in Figure 2.6(B). This trend suggests that the deformation occurs primarily in the top layer of the micropillar. Illumination at λ_{488} resulted in a faster decay of p, indicating that half of the initial volume is already affected for $A < 2.0$. This is in agreement with the longer light penetration depth. In contrast to the other cases, the parameter p for the pillars illuminated at λ_{532} decreases from the value $p \approx 0$ and becomes negative for $A \approx 2.0$. This observation corroborates the hypothesis that the entire volume of the micropillars was immediately reconfigured due to the very long light penetration depth at this wavelength.

Parameters h and l_b: height reduction and base enlargement of micropillars

The parameters h and l_b are defined as the percentage of height reduction, $h = H/H_0$, and the basis deformation, $l_b = L/l_0$, of the photo-deformed pillars with respect to the pristine micropillar, respectively (Figure 2.7(A) and see also Figure 2.5(A)). As depicted in Figure 2.7(B), the curve demonstrates a gradual decline in the evolution of h for all wavelengths as the elongation of the top surface of the pillars becomes increasingly pronounced. This further substantiates the volume conservation mechanism (*60*), whereby a portion of the volume is gradually transported to the side during the reconfiguration process, thereby reducing the actual height of the micropillars. The most striking example of pronounced morphological reconfiguration is evident in the irradiation at λ_{532}, where the rapid decline in the h trend relative to the others is attributed to the involvement of a significantly larger volume of material in the deformation process.

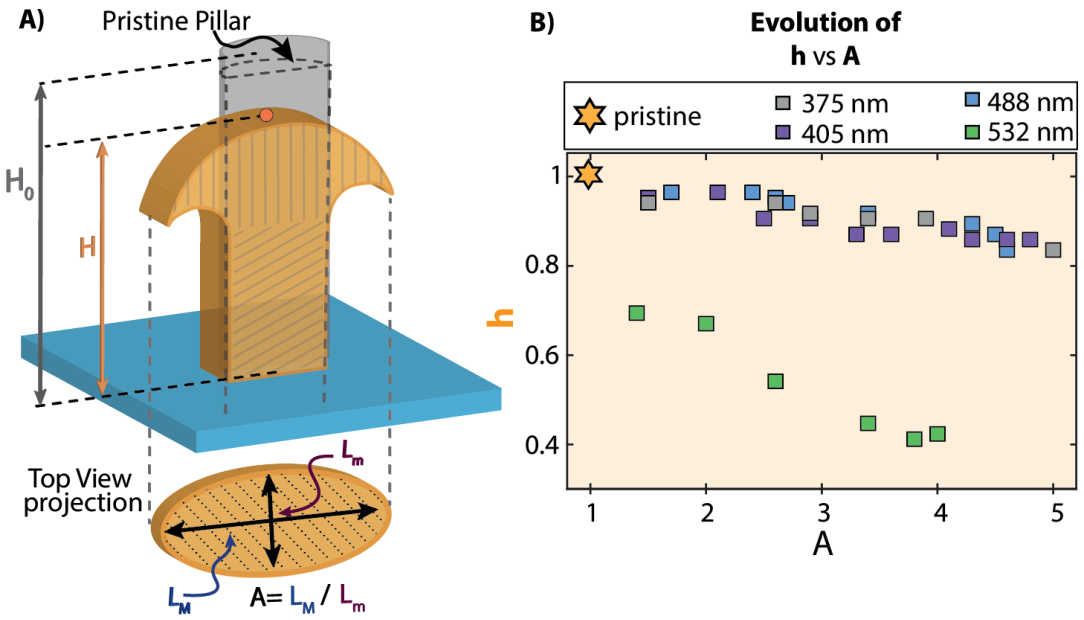

Figure 2.7 Geometrical parameter *h*. (A) The artistic visualization of *h* and (B) its evolution as the function of *A*

Furthermore, at λ_{532}, the base of the pillars was also affected by deformation due to the long penetration depth, as illustrated by the increase in the parameter l_b in Figure 2.8(B) (see Figure 2.8(A) for its geometrical illustration). This observation is consistent with the negative values of the *p* parameter, as illustrated in Figure 2.6(B), which were measured at λ_{532} for $A > 2.0$. As anticipated, based on the limited light penetration depths (in comparison to H_0), the wavelengths λ_{375} and λ_{405} did not reach the pillar base at any deformation strain, resulting in a constant $l_b \approx 1.0$. Ultimately, the intermediate penetration depth for the illumination at λ_{488} affected the pillar base solely in instances of significant volume deformation (l_b increased exclusively for $A > 4.0$), aligning with the concurrent observation of $p \approx 0$. The examination of the trends of these two structural parameters with the deformation strain *A* reinforces the understanding offered by the parameter *p* for characterizing the evolution of the 3D geometry with the wavelength.

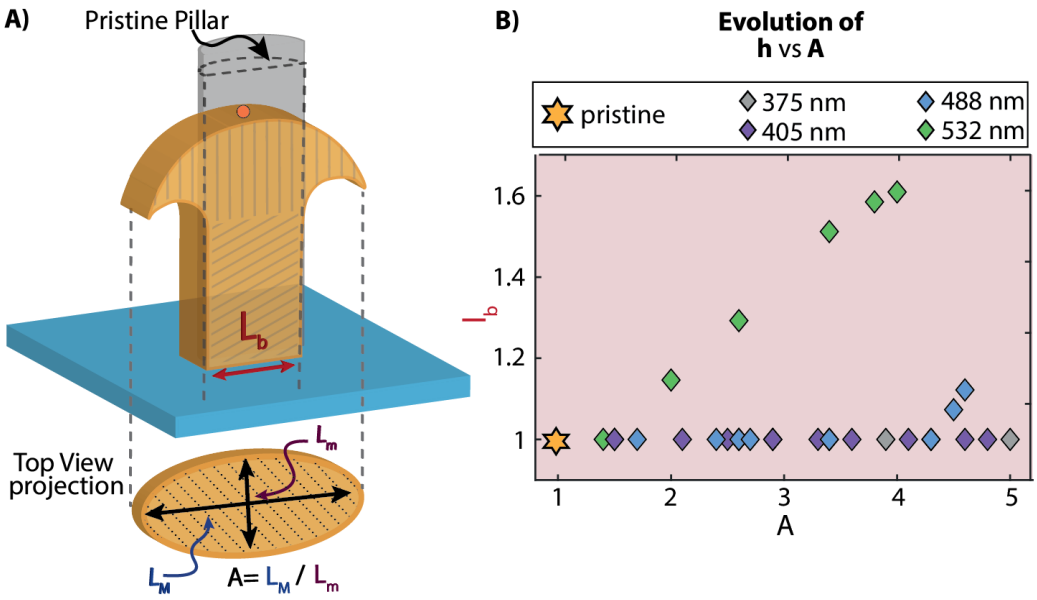

Figure 2.8 Geometrical parameter l_b. (A) The artistic visualization of l_b and (B) its evolution as the function of A

Parameters β and γ: aperture angle and surface curling of micropillars

A defining characteristic of the reshaping micropillar is its innate tendency to form the "overhanging" feature, irrespective of the wavelength employed. This phenomenon can be attributed to the intrinsic nature of the light beam impinging upon the azopolymer-based microvolume from the top. However, the utilization of different wavelengths provides an additional degree of control, specifically regarding the overhanging feature. To systematically assess the impact of varying wavelengths on the overhanging components of the microstructures, two angle-based parameters, β and γ, were introduced.

The β parameter represents the aperture angle of the primary deflection of the lateral pillar surface with respect to the vertical axis. This is the angle of an ideal trapezoid that could be used to approximate the actively deformed volume of the micropillars above the point P (Figure 2.9(A) and see also Figure 2.5(B)). The pristine pillars have an aperture angle $\beta = 0°$, whereas the deformed pillars exhibit increasing values of β.

The parameter γ quantifies the deviation of the structure edges from the ideal trapezoid, thereby characterizing the deflection of the curling edge (Figure 2.10(A) and see also Figure 2.5(B)) with respect to the x-y plane (for which $\gamma = 0°$). In accordance with our sign convention, upward curling is indicated by $\gamma < 0°$, while downward curling is

indicated by $\gamma > 0°$. The pristine cylindrical pillars have $\gamma = -90°$, whereas $\gamma = -\beta$ for an ideal trapezoidal shape.

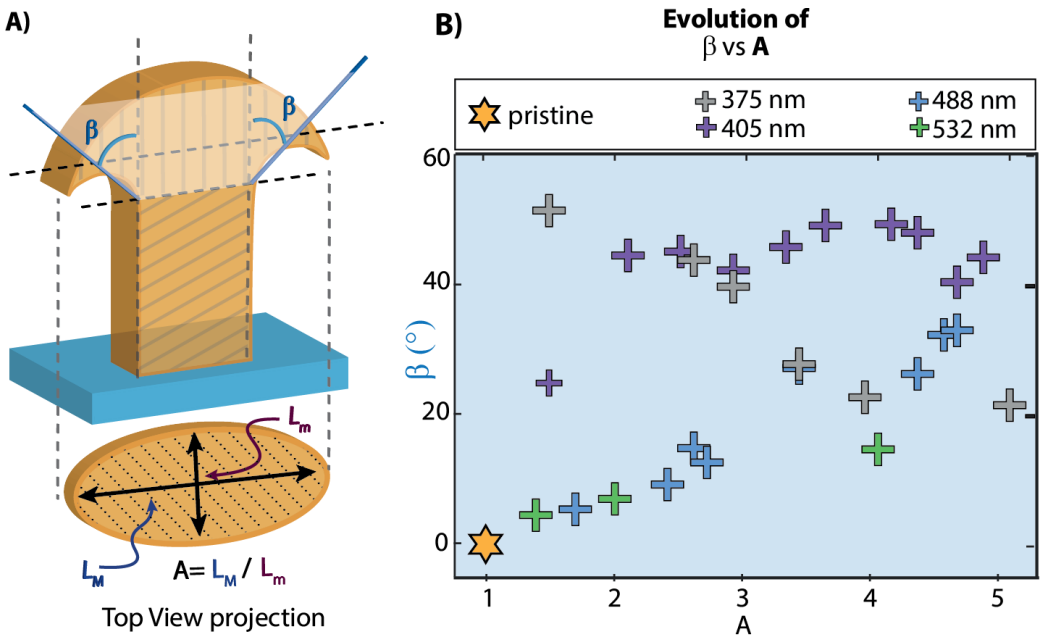

Figure 2.9 Geometrical parameter β. (A) The artistic visualization of β and (B) its evolution as the function of A

The plot in Figure 2.9(A) reveals a gradual increase in the angle β for the deformed structures at λ_{532} and λ_{488}. The higher slope observed for λ_{488} can be attributed to the higher vertical intensity gradient in the pillar volume, which is a consequence of the shorter penetration depth. The abrupt increase of β in the early evolution stages ($A <$ 2.0) suggests that a wavelength with a significantly shorter penetration depth than the H_0 results in a rapid and intense curvature of the edges of the top surface of the microvolume. However, the angle β for λ_{405} and λ_{375} exhibits an irregular trend afterwards, likely due to the curling of the micropillar top surface, which makes the trapezoidal approximation inadequate.

The development of the parameter γ can be classified into two distinct categories: the slow-curling structures observed at λ_{532} and λ_{488}, and the fast-curling structures observed at λ_{405} and λ_{375}. The slow-curling structures are distinguished by $\gamma < 0°$ for each value of A, as illustrated in Figure 2.10(B). In contrast, the fast-curling structures exhibit a transition to $\gamma > 0°$ at an early stage of evolution, resulting in the formation of a pronounced overhanging structure (see Figure 2.10(B)). The curling of the surface is a

consequence of the differing speeds of light-fueled moving mass layers in the azopolymer microvolume, which are subject to a gradual reduction in lateral forces as a result of the field-gradient effect. In particular, the layers in closer proximity to the top surfaces exhibit a higher velocity than those situated beneath them. The penetration depth of light is inversely correlated to the strength of the lateral force gradient, and vice versa. The strong gradient of interfacial forces between the different layers within the azopolymer volume can then cause the surface to curl. This is demonstrated by the fast-curling structures at λ_{405} and λ_{375}, which exhibit a significant degree of curling, in contrast to the structures deformed at λ_{532} and λ_{488}, which display only a negligible curling at any deformation level.

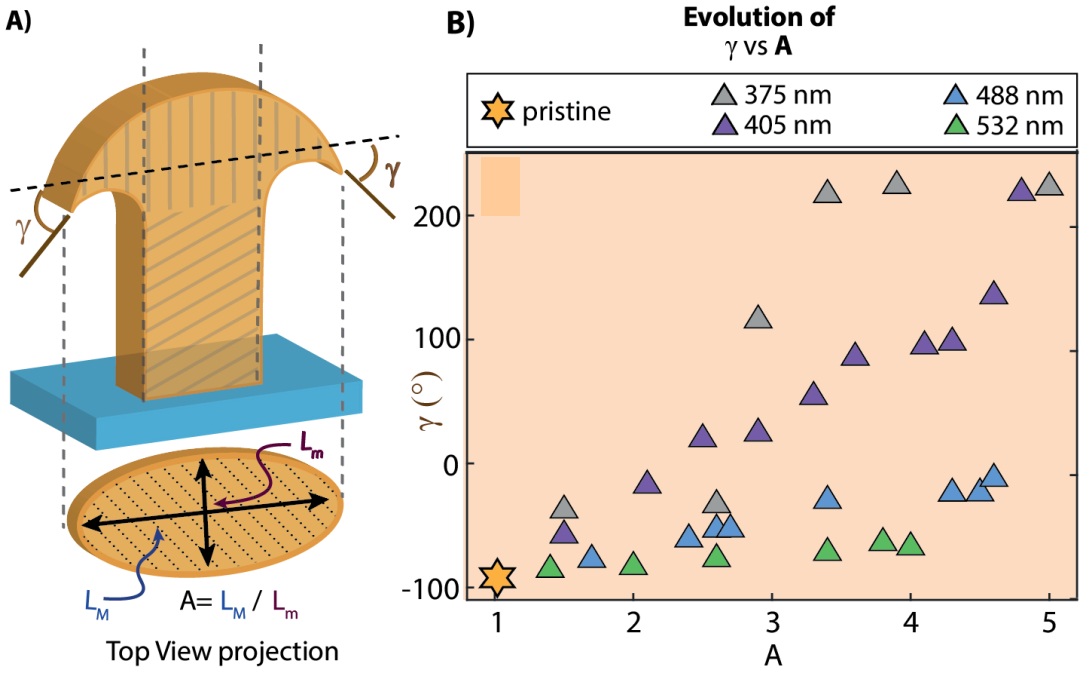

Figure 2.10 Geometrical parameter γ. (A) The artistic visualization of γ and (B) its evolution as the function of *A*.

Control of the three-dimensional pillar morphology

A precise examination of the morphological characteristics of the aforementioned sections can facilitate the deterministic fabrication of diverse, intricate three-dimensional mesostructures. This can be achieved by reconfiguring the azopolymer micropillar array with varying illumination configurations and light wavelengths. It

should be noted that the evolution of the 3D geometric parameters is, however, constrained by volume conservation, which occurs in the light-induced azopolymer reconfiguration process. Nevertheless, the findings of this study indicate that the precise selection of the light wavelength can facilitate the minimization of parameter entanglement, thereby enabling straightforward control over a range of complex 3D microstructure shapes. Furthermore, it is noteworthy that the methodology presented is not confined to the straightforward experimental configuration depicted herein. Alternative irradiation scenarios, including diverse polarization configurations, the incorporation of additional spatial constraints on light-induced mass migration, such as a PDMS capping layer, and the investigation of varying azo microvolume morphologies, can be pursued to generate a multitude of distinctive 3D structures.

2.3 Wavelength-dependent 3D Photo-reconfiguration for Wettability Tailoring

In 1995, Casie and Baxter published a seminal study on the unique wettability effect observed in duck feathers. This effect, known as superhydrophobicity, arises from the structural morphology of the feather surface rather than from a strong hydrophobic agent (*61*). It is a topic of considerable research interest to investigate the impact of three-dimensional mesoscopic roughness on the wetting characteristics of solid surfaces. In addition to the conventional models (Wenzel and Cassie-Baxter) that relate the wetting behavior to the geometric parameters (e.g., pitch, diameter, height) of the surface textures of a given material, numerous studies have underscored the impact of sharp overhanging and re-entrant features that are capable of pinning the triple-phase contact line (*32*, *62*) and inducing superhydrophobic effects (*63*, *64*). To illustrate, the diminution of the pillar height sustaining the roughness-induced hydrophobic wetting Wenzel state can result in a reduction in the observed hydrophobicity, manifested as a diminished contact angle (CA) (*65*, *66*). Conversely, the introduction of overhanging structures can facilitate the retention of air between the solid structures in a Cassie-Baxter state, thereby enhancing hydrophobicity and the contact angle. Generating analogous morphological variations in artificial rough surfaces typically necessitates the utilization of bespoke advanced manufacturing techniques that are not readily adaptable for the generation of opposite wetting behaviors (e.g. both an increase and a decrease in hydrophobicity).

As evidenced in the findings presented in Chapter 2.2, the wavelength-dependent 3D reshaping of azopolymer-based micropillars has the potential to be utilized as a means of altering the wettability of the surface. In particular, the application of two different wavelengths can induce two distinctive wettability evolution pathways from an initial

surface that is pristine. Ultimately, the final surface may exhibit two opposing wettability effects, depending on the wavelength utilized. To this end, the reconfiguration of an array of cylindrical azopolymer micropillars at two wavelengths was employed to selectively induce either an increase or a decrease in the CA of the pristine surface.

In the experimental phase, the surfaces were prepared with a similar geometry to that depicted in Figure 2.3(A), but with a different arrangement (diameter d = 8 µm, pitch p = 12 µm, initial height H_0 = 3.0 µm). Subsequently, the surface was irradiated with circularly polarized collimated laser beams at λ_{375} or λ_{488} to induce isotropic in-plane pillar reconfiguration (*34*). The intensity of the lasers was calibrated to achieve a comparable reconfiguration dynamic at the two wavelengths (50 mW/cm² for both wavelengths). The micropillars underwent reshaping for varying exposure times to assess the evolution of wettability properties. Different exposure times were employed to induce incremental lateral deformation (in the range of 5–120 minutes), while the varying penetration depths of the irradiation resulted in differential deformation of the pillar volume.

It is important to note that the penetration depth of λ_{488} (approximately 3.2 µm) was comparable to that of H_0 (approximately 3.0 µm) in the new pristine array. In contrast, the penetration depth of λ_{375} (approximately 0.1 µm) was significantly shorter. To test the effect of the reconfigured surfaces on their wettability, a custom-built experimental setup was employed for the measurement of the water contact angle (CA). A 2 µL water droplet was dispensed from a microliter syringe (Hamilton) and carefully placed on the sample surface. After approximately 5 s, the contact angle (left and right) of each drop was measured using *ImageJ v1.46r software* with the *DropSnake* plug-in. The measurements were conducted in a temperature/humidity-controlled room. An average contact angle value was extracted from at least five independent measurements for each structured area.

Figure 2.11 illustrates the morphological evolution of the surface and the corresponding contact angle (CA) measurements as a function of time following exposure to the selected wavelengths. Two disparate wetting behaviors are discernible. The reconfiguration at λ_{375} resulted in the formation of mushroom-like pillars with an increasing diameter. As discussed in Chapter 2.2.3, the analysis of the residual undeformed volume fraction indicates that the short penetration depth of the light allowed the preservation of the pillar-like structure and the formation of sharp reentrant features. The measured CA increased from the value of CA = 123 ± 3° of the pristine array, which exhibited a pinned wetting state determined by the geometrical parameters of the pillars (*32*), to CA = 147 ± 3° after 55 minutes of exposure. This is consistent

with the expected enhancement of the Cassie-Baxter wetting state. The observed decrease in CA from the maximum value with longer exposure times can be attributed to a reduction in pillar height (see the trend of the *h* parameter in Figure 2.7(B) for a general comparison). This may facilitate the filling of the air gaps between the pillars with the liquid.

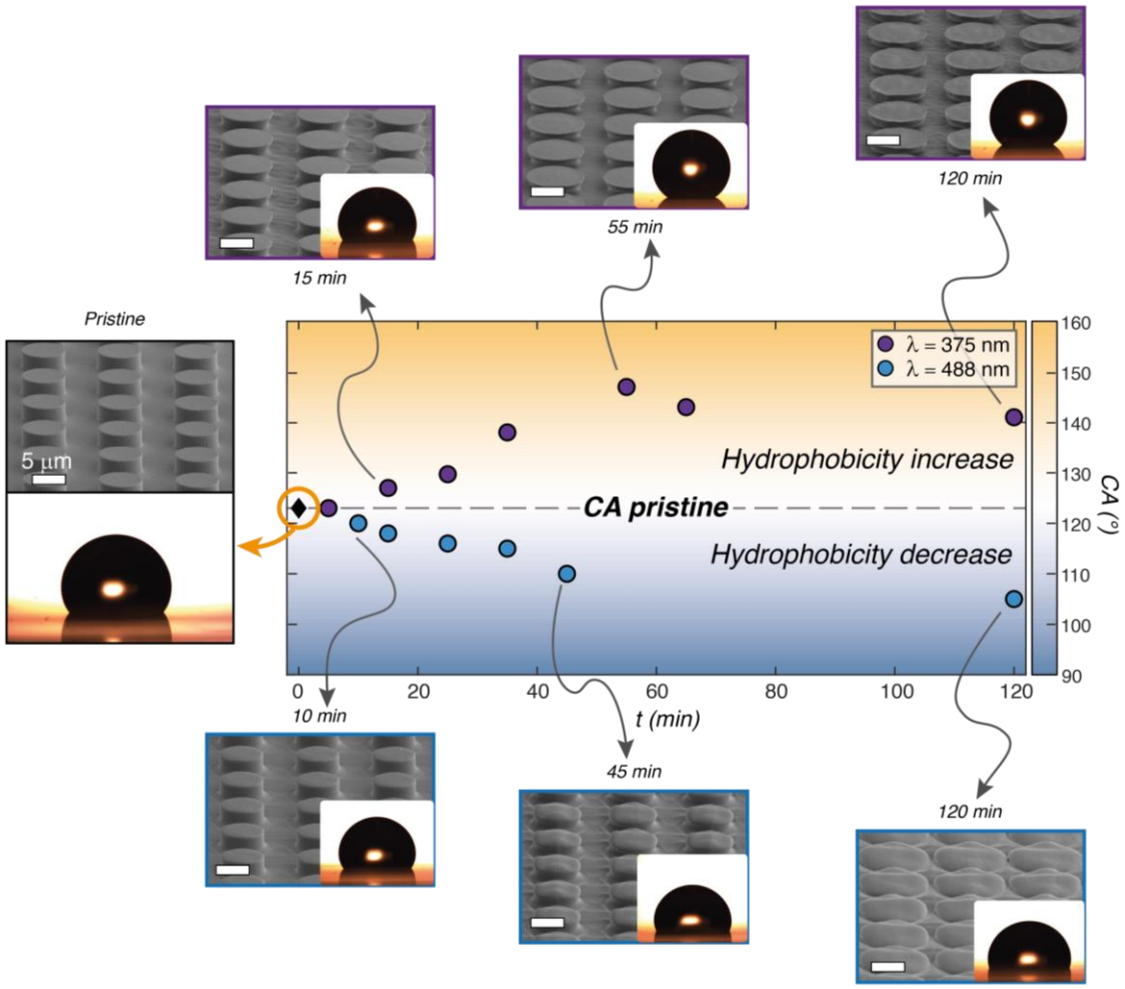

Figure 2.11 The wettability evolution of the photodeformed surfaces. The graph shows the evolution of the Contact Angle (CA) of the micropillars irradiated at λ_{375} (top) and λ_{488} (bottom) with increasing irradiation time (t). For the pristine surface and selected CA values, the tilted SEM images of the 3D reshaped micropillars and their corresponding water CA photographs are shown as a representation of the different regimes.

In contrast, a different trend was observed for the CA of the surfaces that were reconfigured at λ_{488}. In general, the reduction in hydrophobicity observed for this surface can be attributed to the absence of reentrant features and the notable height reduction. Consequently, the surface exhibits a tendency to transition from the pinned pristine state to the Wenzel hydrophobic state, reaching CA = 105 ± 3° after 120 minutes of exposure. At this stage, the micropillars underwent a complete deformation, transforming the pristine cylindrical geometry into flattened dome-like structures. This behavior is consistent with the anticipated microvolume reconfiguration resulting from light beam penetration depths comparable to the initial pillar height. Based on the analysis presented in Figure 2.11, the CA on the specified micropillar azopolymer surface can be precisely tailored within a range of over 40° by exploiting the light penetration depth as a lithographic parameter.

3 Molding 3D Micro-architectures with Light:

Reshaping azopolymer-based micropillars using structured intensity pattern of light

The multitude of strategies for creating intricate three-dimensional architectures using azopolymers gained momentum primarily due to the distinctive directionality response of azopolymer-based microvolumes to light. By modifying the illumination configuration, it is possible to induce different photodeformation effects on azopolymer-based microstructures. Chapter 2 illustrates how a simple manipulation, specifically varying the wavelength of the illumination beam while maintaining other experimental parameters constant, can result in the formation of distinct geometrical architectures in the final microstructures. Additional demonstrations, such as varying the incident angle of the beam, the polarization state of the beam, and polarization-based interference patterns, have been demonstrated to yield diverse three-dimensional micro-architectures (see Chapter 1.4).

Despite the intriguing results yielded by these strategies, some limitations arise due to the monotonous characteristics of the illumination scheme employed. Firstly, they lack *geometric diversity*. This characteristic is defined as the capacity to generate a multitude of geometric forms through a single methodology. In the case of the aforementioned techniques, the generation of different morphologies requires either the introduction of additional illumination steps or a modification to the optical configuration. Secondly, they lack the capacity for *localized patterning*, as they are only able to produce a uniform morphology across a large area in a single exposure step. Indeed, numerous technologies, including optical component manufacturing (*67*) and information encoding (*68*), depend on the ability to create structures on demand in specific locations or groups, with varying configurations, including shapes, relative orientations, and spatial arrangements.

In order to achieve the capabilities of *geometric diversity* and *localized patterning*, it is essential to utilize a light-matter interaction that can be spatially triggered with precision and flexibility. Computer-based holography (CGH) has been demonstrated to produce arbitrary spatially intensity patterns of light and has been demonstrated to produce functional surface patterns based on azopolymer flat surfaces (see Chapter 1.3.3). The

capability of designing spatially intensity patterns of light can be utilized to impart geometric diversity and localized patterning capability into the photoreconfiguration of the azopolymer-based microstructures in a straightforward and one-step procedure.

The fundamental concept of employing a spatial intensity pattern on a pre-structured surface is to facilitate a rational design of the spatial light distribution in accordance with the geometric dimensions and configuration of the microstructures.

This study investigated this concept by employing CGH to project rationally designed 2D light patterns onto the surface of an array of cylindrical azopolymer micropillars, which then underwent three-dimensional deformation with an on-demand morphology. The fabrication of microstructures with concave, convex, symmetric, and asymmetric morphologies from a single pristine array has been achieved through a single-step illumination process. Additionally, the on-demand reshaping of multiple micropillars with individualized control of morphology has been demonstrated. The results reported in this Chapter are used as the basis for the paper "I. K. Januariyasa, F. Reda, F. Borbone, M. Salvatore, S. L. Oscurato, Molding three-dimensional azopolymer microstructures with holographically structured light. *RSC Appl. Interfaces* (2024)".

3.1 The Generation of 2D Structured Intensity Patterns of Light

In this study, a custom computer-generated holography (CGH) system was employed for the generation and projection of structured grayscale intensity patterns of light on the micropillar's top surfaces. In general, CGH employs the concept of modulating the wavefront of the initial beam to achieve an intensity modulation in its wavefront (*30*). The capacity of CGH to achieve this depends on the ability of the spatial light modulator (SLM) to modulate the phase of the beam on a pixel-by-pixel basis. In optical holography, the SLM serves a function analogous to that of the holographic plate, which contains the fringe pattern that encodes the field information of the recorded real object. However, the SLM can simulate any fringe pattern by digital means, thereby eliminating the need for real objects to produce holographic patterns (*69*). Consequently, CGH can generate any arbitrary spatial intensity pattern of light with the aid of a computer alone.

Briefly in practice, the CGH setup and how it works follows this procedure (see more details in refs (*30, 31, 70*)). A laser beam with a wavelength of 491 nm (emitted from a Cobolt Calypso laser) was expanded, collimated, and impinged upon a phase-only spatial light modulator (SLM, Holoeye Pluto). The beam was then modulated with a calculated phase profile (kinoform). Subsequently, the modulated beam from the SLM was propagated through a *4f* lens configuration, specifically designed to produce a

demagnified image of the field at the SLM plane in the back focal plane of a microscope objective (Mitutoyo, 50X, NA = 0.55). This configuration enables the projection of a tailored holographic illumination pattern onto the surface of the target micropillars. The light field distribution was designed from a bitmap grayscale image (1080×1080 pixels), which reproduced the target distribution of light in the sample plane. This was created with conventional image processing software. In order to ensure that the diameter of the micropillar's top surface was accurately represented, each grayscale pattern was designed within a circular area with a diameter of $D_0 = 2R_0 = 19$ pixels. This corresponded to approximately 7.4 µm in the holographic pattern. This value was obtained through a conversion factor of 1 pixel ≈ 0.39 µm, previously determined for our experimental setup (*30*, *31*). Subsequently, the grayscale image was employed to calculate a set of 1,000 independent kinoforms through the implementation of an iterative Fourier transform algorithm (*71*), founded upon the Mixed Region Amplitude Freedom (MRFA) extension of the standard Gerchberg-Saxton phase-retrieval algorithm (*72*). To mitigate the impact of speckle noise inherent to hologram reconstruction, the independent kinoforms comprising the calculated set were displayed sequentially on the SLM at a frame rate of 30 Hz. The aforementioned time average has been demonstrated to reduce the roughness of an irradiated azopolymer surface (*30*, *31*, *70*). In the typical reconfiguration experiments, an array of 7 × 7 circular holograms of diameter D_0 was used. These holograms were designed with different geometries and grayscale values in the position corresponding to the 7 × 7 azopolymer micropillars on the surface.

3.2 Applying Holographic Intensity Patterns on Azopolymer Microstructures

In order to realize the concept of utilizing the holographic pattern for three-dimensional reshaping of azopolymer-based micropillar arrays, an experimental approach was devised and illustrated in Figure 3.1(A). The initial array of cylindrical micropillars was replicated on the azopolymer surface using soft molding through a PDMS stamp (see Chapter 1.5 for further details). Subsequently, a two-dimensional holographic light pattern generated by CGH was employed to illuminate the micropillars.

The distinguishing feature of the technique presented in this study is that the photodeformation of microstructures is no longer predominantly influenced by the directionality of polarization, as previously demonstrated in Chapter 1.4. Instead, it is driven by the gradient intensity of light. To briefly recall the mechanics of this phenomenon, light-induced mass migration in azopolymer tends to transport from a high intensity field to a low intensity field. In the case of circularly polarized light, which is the case in this study, there is no directional preference for mass migration. Nevertheless, this approach allows for the introduction of unconventional

microarchitectures, such as asymmetrical architectures, through the manipulation of local gradient intensity distributions, which will be discussed in greater detail later in this chapter. In fact, the micro-architectures that can be produced from this strategy are not easily feasible using polarization-based approaches (see Chapter 1.4).

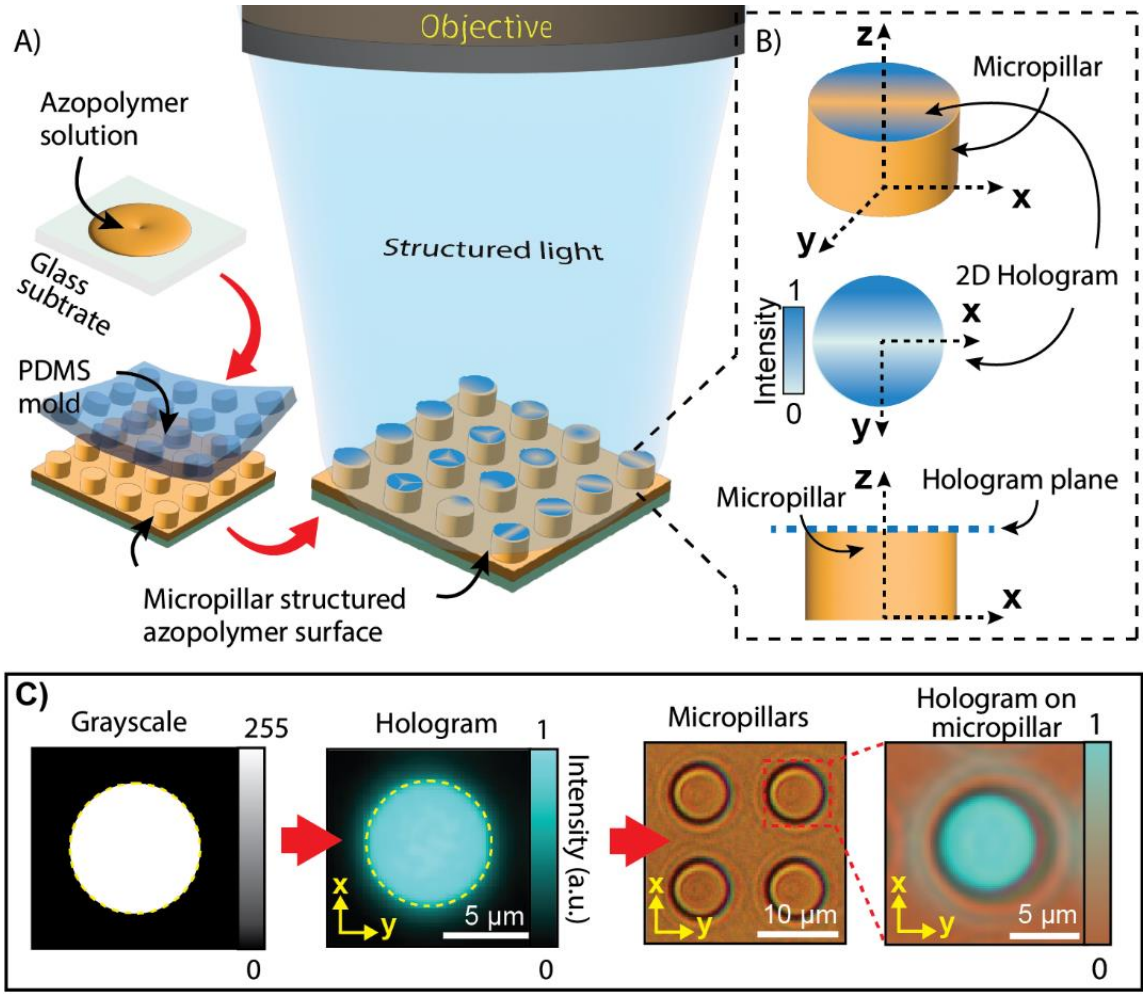

Figure 3.1 Reshaping micropillars using 2D holographic light intensity patterns. (A) The general steps of the experiment: (from left to right) the deposition of the azopolymer solution on a glass substrate, stamping with a PDMS mold to produce the azopolymer micropillars on the surface, and the illumination with the 2D hologram. (B) The illustration of the alignment procedure between a holographic pattern and a micropillar's top surface. C) (from left to right) The initial design of a grayscale pattern (R_0 is the radius of the circular grayscale design), the experimental holographic pattern in the sample plane obtained from an average of 1000 frames of the holographic movie, the experimental brightfield optical image of a group of micropillars before illumination, and the image of the hologram focused on a micropillar's top surface after alignment.

The key concept of the technique is the ability to design a hologram with a tailored size with respect to the top surface of the micropillar. In practice, it is necessary to have the ability to align the designed intensity pattern of light with the geometric parameter of the pre-existing micropillars on the surface in a precise manner. To achieve this, the illumination pattern was accurately positioned in three dimensions by moving the azopolymer films using a motorized sample stage. Specifically, the sample was translated along the axial direction (z) in order to align the top surface with the reconstruction plane of the hologram, as illustrated in Figure 3.1(B). In this plane, maximum resolution and contrast are achieved for the intensity gradients in the light pattern, thereby maximizing the effectiveness of the light-induced reconfiguration process. It is important to note that at the wavelength used in this experiment, the penetration depth of light is approximately 3.2 µm, which is greater than the height of the pristine pillars (about 2.8 µm). Moreover, the depth of field (approximated to be λ/NA^2) of the microscope objective utilized to project the holographic pattern is within the same range. This configuration permits the deformation of a considerable portion of the micropillar volume, where the axial intensity gradient plays a comparatively minor role with respect to the transverse gradients in the illumination.

To present a general overview of the workflow of the method, the initial implementation of this work involved the design of a circular uniform area with a uniform grayscale level, as illustrated in Figure 3.1(C). Subsequently, the grayscale image is fed into the CGH calculation algorithm, which provides the phase profile utilized for hologram reconstruction via the SLM. Typically, a reconfiguration experiment involves directing the hologram towards the sample plane and aligning it with the top surface of a micropillar, facilitated by the integrated brightfield microscope configuration within the holographic system. Figure 3.1(C) illustrates the intensity pattern of the hologram and the outcome of the alignment for the specified homogeneous intensity distribution. It is noteworthy that the light distribution and relative positioning can be readily adjusted, as will be demonstrated in the subsequent sections.

3.3 Molding Microstructures with 2D Holographic Intensity Patterns

3.3.1 Photodeformaton from localized intensity patterns

To grasp the idea of having 2D hologram as the “photodeformation tool” for azopolymer-based micropillars, a basic demonstration is presented in Figure 3.2(A–D). In this example, circular holographic patterns of identical dimensions to those of the top surface of the pristine pillars are employed to selectively reconfigure a row of six

micropillars. Figure 3.2(A) depicts the hologram design, which comprises six circles with varying relative grayscale levels (8-bit level in the bitmap image). From this grayscale pattern, six circular holograms with varying relative light intensity levels (0-100%) were produced by the CGH system and used to illuminate a row of six micropillars (Figure 3.2(B)). The outcome of the photodeformation of the sub-array following an exposure time of 15 seconds is illustrated in the AFM image in Figure 3.2(C). The varying intensity of the holograms at the same exposure time results in disparate deformation rates of the micropillars' architecture, as depicted in Figure 3.2(D).

This introductory demonstration is designed to provide a more detailed understanding of the general reconfiguration process of an individual micropillar within an array when it is subjected to a localized intensity pattern of light. Firstly, it is necessary to understand the response of a single micropillar to a localized, homogeneous intensity pattern. Figure 3.2(B) illustrates the three-dimensional morphological evolution of the micropillar from its initial state (0% intensity pattern or no illumination) to its reconfigured state induced by the circular hologram with a relative intensity of 60%. The micropillar undergoes three-dimensional reconfiguration, resulting in a reduction in height and an expansion in diameter in relation to its original geometry. This is a consequence of the approximate preservation of the polymer volume during the light-induced mass migration, accompanied by isotropic pillar elongation in the polarization plane. This mechanism has been successfully modeled in previous theoretical works on the assumption that the polymer undergoes viscoplastic deformation driven by light-induced stress (*23*, *73*, *74*). Furthermore, the same response has been observed when the entire pillar array is irradiated with an extended homogeneous, circularly polarized beam, as demonstrated in previous studies (*32*, *75*).

The localized control over the spatial intensity distribution is demonstrated to be a robust tool when it is applied to induce a localized photodeformation in each of the micropillars within the affected area, as illustrated in the AFM results presented in Figure 3.2(A). The linear increase in the relative intensity level in the hologram (Figure 3.2(A)) results in a nearly linear decrease in height and an increase in diameter of the illuminated pillars of the same array. It is noteworthy that the exposure time can also be varied, thereby providing spatially selective control over the exposure dose and the reconfiguration dynamics of azopolymer microstructures (see Figure 3.2(C–D)). In comparison to conventional strategies, the degree of deformation is contingent upon the exposure dose, which can be calibrated by regulating either the light intensity level or the exposure time. In experiments with a single beam (*32*, *37*, *76*, *77*), only one of the two parameters is typically varied, resulting in a controlled reconfiguration of the

microstructures in the illuminated area. However, this approach lacks local spatial selectivity.

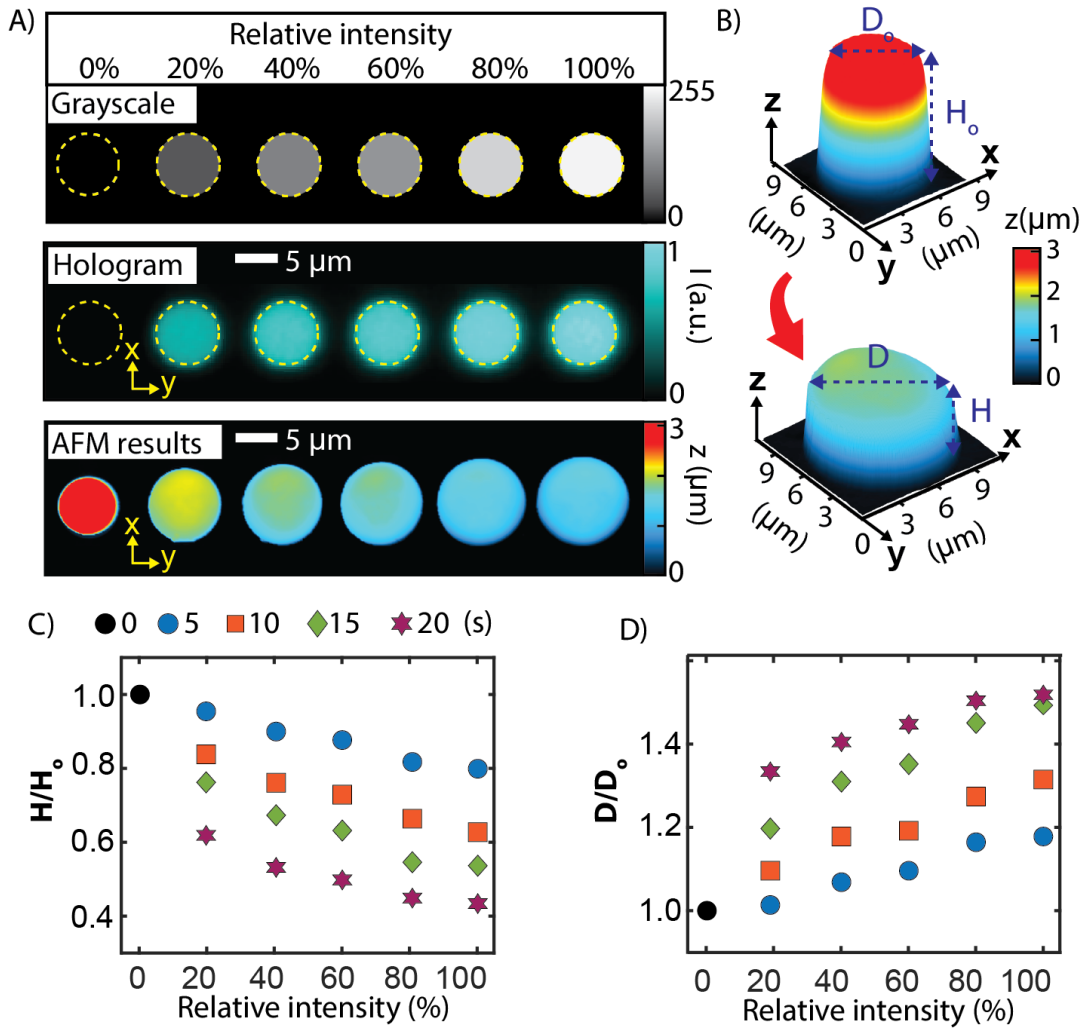

Figure 3.2 The control of micropillar morphology using varying homogeneous intensity patterns. (A) Six different circular grayscale patterns with varying intensity (gray level of 255 = 100%, 204 = 80%, 153 = 60%, 102 = 40%, 51 = 20%, and 0 = 0%), their experimental hologram counterparts, and the top view of AFM results of the reshaped micropillars. (B) The change of the 3D morphology of the micropillar before and after the illumination (60%, 15 s), respectively. The evolution of (C) H/H_o and (D) D/D_o of different intensity levels relative to the time exposure. H_o and D_o are the pristine height and diameter of the micropillar, respectively. H and D are the height and the diameter of the micropillar after exposure to the hologram.

3.3.2 Two-dimensional gradient intensity pattern for geometrical complexity

The localized homogeneous beam illustrated above offers the spatial flexibility of the approach but has yet to demonstrate two aspects of the holographic intensity patterns for photodeformation: geometrical complexity and geometrical diversity. In the configuration depicted in Figure 3.3(A), the circular uniform hologram had a diameter identical to that of the top pillar surface, thereby uniformly reshaping the top perimeter of each pillar in the array. This is achieved by designing the hologram with a radius (R_0) that is approximately equal to that of the pillar. The process produces identical cylindrical architectural structures, wherein the only alteration occurs in the geometrical parameters (i.e., height and diameter). In order to impart geometrical complexity and diversity to the final reconfigured microstructures, a spatially structured intensity distribution with eventual directional gradients is applied over an area smaller than the pillar diameter ($R < R_0$). In the holographic system under consideration, the patterns of light can be systematically modified by designing a spatial variation of the gray levels in the bitmap image used for the hologram design.

Figure 3.3(A) presents an illustrative example of a simple radial intensity gradient (increasing from 100% to 0% relative intensity) that is developed from the center of the pillar to a radius equal to $0.8R_0$. As illustrated in Figure 3.3(A), the radial gradient observed in the experimental hologram generated by the CGH system aligns with that of the grayscale design. In the light-induced reconfiguration experiment, when the azopolymer micropillar is aligned with the center of the radial hologram, the resulting intensity distribution produces a concave deformation in the center of the micropillar, exhibiting radial symmetry (Figure 3.3(B)). The AFM topographic profile and the top view of the scan provide further insight into the detailed reshape of the micropillar (Figure 3.3(C)).

To elucidate the relationship between the spatial intensity gradient and the final morphology of the microstructures, the radius of curvature (R_c) of the surface of the concave reshaped pillar was measured, as illustrated in Figure 3.4(A). The analysis involved varying the exposure time and extension (and, consequently, the local strength) of the intensity gradient. In particular, three radially symmetric linear gradients of radius $0.5R_0$, $0.8R_0$, and R_0 were designed, generating the holographic patterns of Types I, II, and III, respectively, as illustrated in Figure 3.4(B).

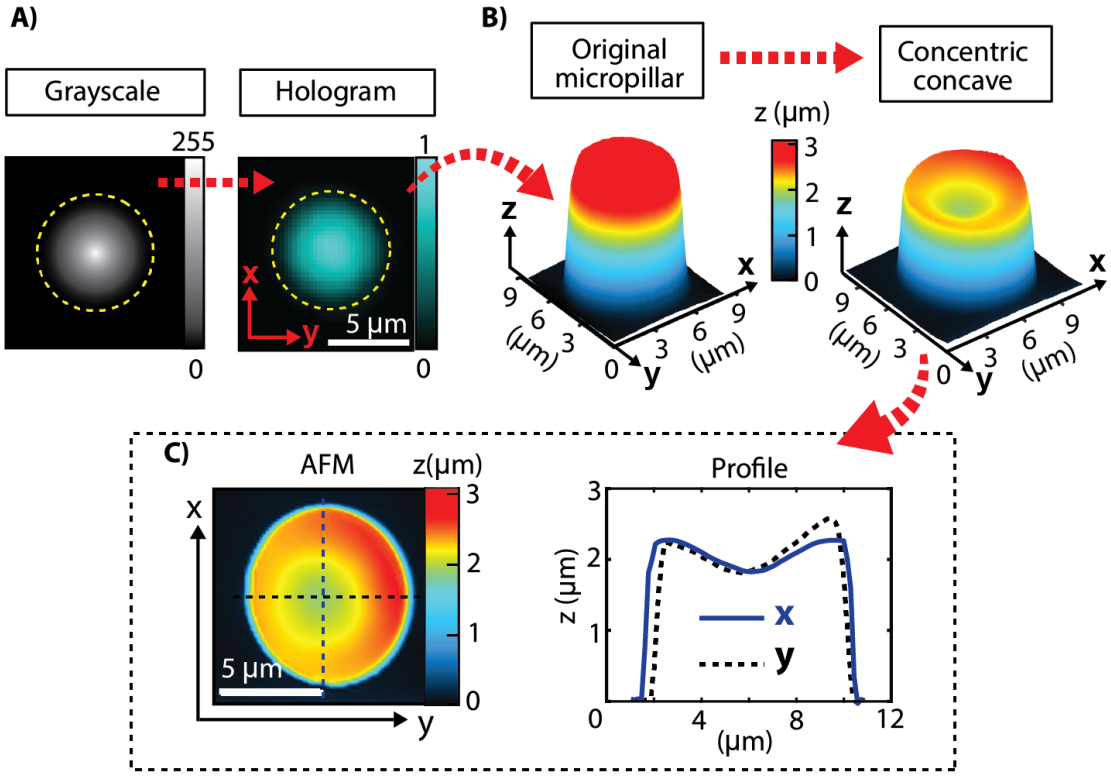

Figure 3.3 Complex microstructural morphology induced by radial gradients of light. (A) The grayscale design of a radial gradient of intensity pattern and the corresponding hologram. (B) The evolution of the micropillar's morphology before (left) and after (right) irradiation, measured by the AFM. (C) Top view detailed morphology of the reshaped micropillar and its topographic profiles along the *x* and *y*-axis.

An additional experimental parameter that can be employed to regulate the final architectural configuration is the time of exposure. This is illustrated in Figure 3.4(E), which depicts the reduction in R_c as a function of exposure time. Figure 3.4(C) depicts the topographic profile for varying exposure times to the Type I pattern. It can be observed that the surface curvature intensifies with increasing exposure time. The variation in intensity gradient extension for a fixed exposure time leads to a reduction in curvature, as illustrated by the evolution of the topographic profiles in Figure 3.4(D) and the measured radius of curvature in Figure 3.4(E).

The above behavior, derived from the general phenomenon, exemplifies a key feature of light-induced mass migration in azopolymers under circularly polarized light intensity gradients. The motion of the material in such an illumination configuration is driven isotropically along the direction of the gradient, with a strength determined by the local intensity gradient. This gradient is higher for Type I holograms than for Type II and III

(Figure 3.4(B)). Consequently, the Type I hologram induces the greatest deformation of the upper surface of the pillar, with the lowest radius of curvature. A longer exposure time results in a higher accumulation of this mass migration effect, thereby increasing the total deformation of the upper surface, but with higher deformation rates for stronger intensity gradients (Figure 3.4(E)).

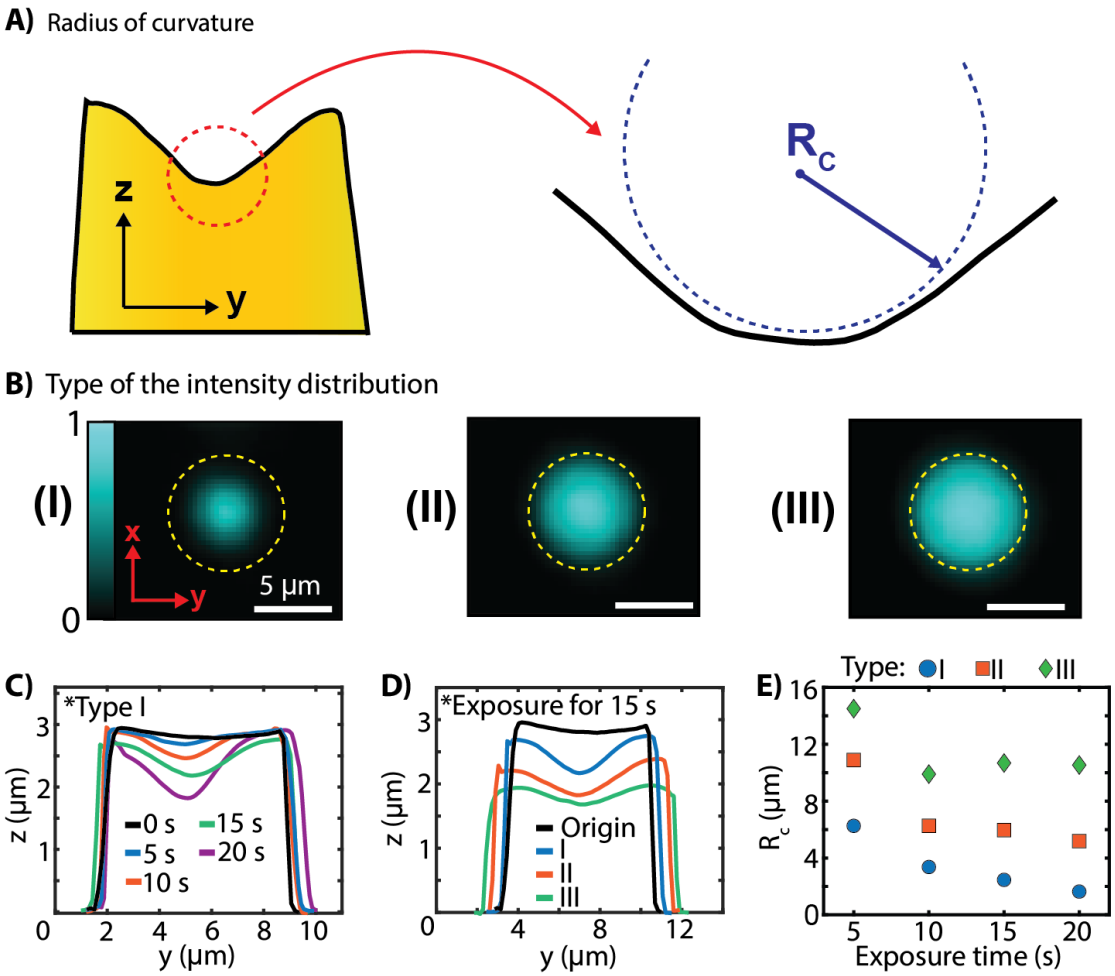

Figure 3.4 Morphological analysis of the intensity gradient-induced photodeformation. (A) The illustration of the geometric parameter R_c. (B) Experimental images of three types of radial gradients of light intensity. (C) The evolution of the topographic profile under type I radial gradient illumination for different exposure times. (D) Topographic profiles of the reshaped micropillars under illumination with different types of radial holograms for 15 s of exposure time. (E) The evolution of R_c versus the exposure time for three different types of intensity distributions.

3.3.3 Deterministic geometrical diversity

The radial gradient demonstrated above highlights the versatility of the holographic technique in inducing complex architectural features in reshaped microstructures. The unique architectural feature of the intensity gradient-induced deformation is the local height modulation, which inversely reflects the relative local intensity experienced by the micropillar. The straightforward relationship between 2D holographic patterns and the final 3D microarchitecture allows for deterministic design of different microstructures by rationalizing the design of the intensity patterns. This approach demonstrates another aspect of holographic-induced photodeformation, namely *geometrical diversity*.

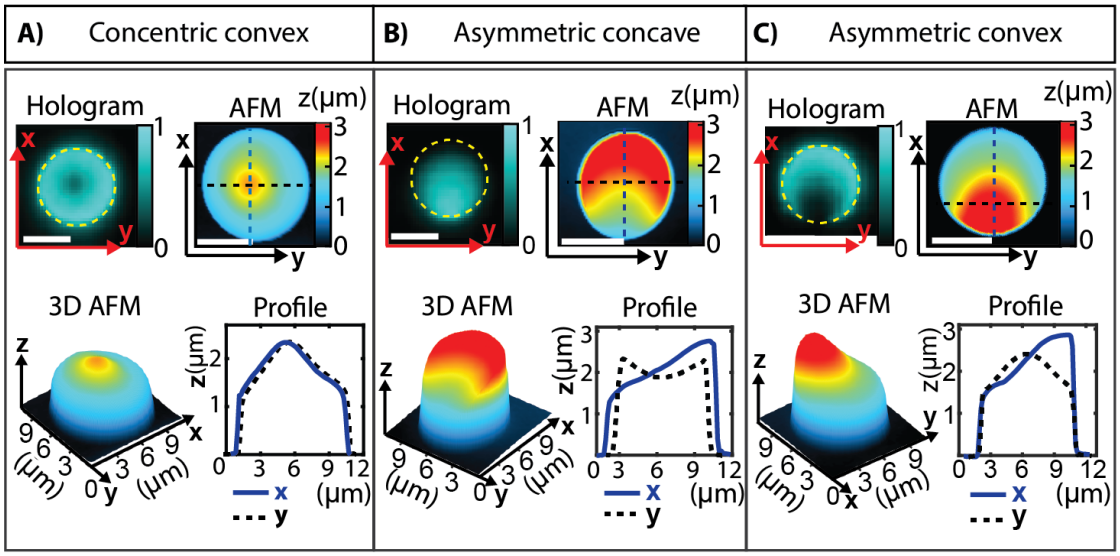

Figure 3.5 Complex reconfigured pillars with (A) symmetric convex, (B) asymmetric concave, and (C) asymmetric convex architectures. All microstructures, characterized by AFM, were produced by 15 s of exposure with the corresponding hologram, shown in the top-left image of each panel. White scalebars corresponds to 5 μm.

Subsequently, deterministic design methodologies were employed to create a series of holographic patterns, which were then used to generate distinct microstructures. As an initial example, the geometric design of the reshaped micropillar can be inverted by reversing the direction of the intensity gradient in the holograms. Figure 3.5(A) depicts a radial gradient pattern designed as the inverse of the pattern presented in the previous section (Figure 3.2(A–C)). This results in a hologram with the minimum light intensity concentrated in the center. The pattern produces a symmetric convex surface profile in

the final morphology, which is the inverse of the concave profile observed in the previous section (Figure 3.2(A–C)).

A further set of light-induced structural transformations is derived from the shifting of the center of the gradient in the hologram, which produces asymmetric three-dimensional architectures. Figure 3.5(B) illustrates an instance where the intensity center in a petal-like hologram has been positioned at the outer edge of the pillar. The configuration of an intensity gradient across the surface of the pillar with an asymmetric distribution result in the formation of an unconventional concave microstructure. This results in a slanted profile along the *x*-axis and a concave profile along the *y*-axis, as illustrated by the topographic profile in Figure 3.5(B). Similarly, the inverse morphology can be obtained by reversing the direction of the intensity gradient in the petal-like hologram (Figure 3.5 (C)). This results in an asymmetric convex structure after the light-induced reconfiguration of the pristine micropillar.

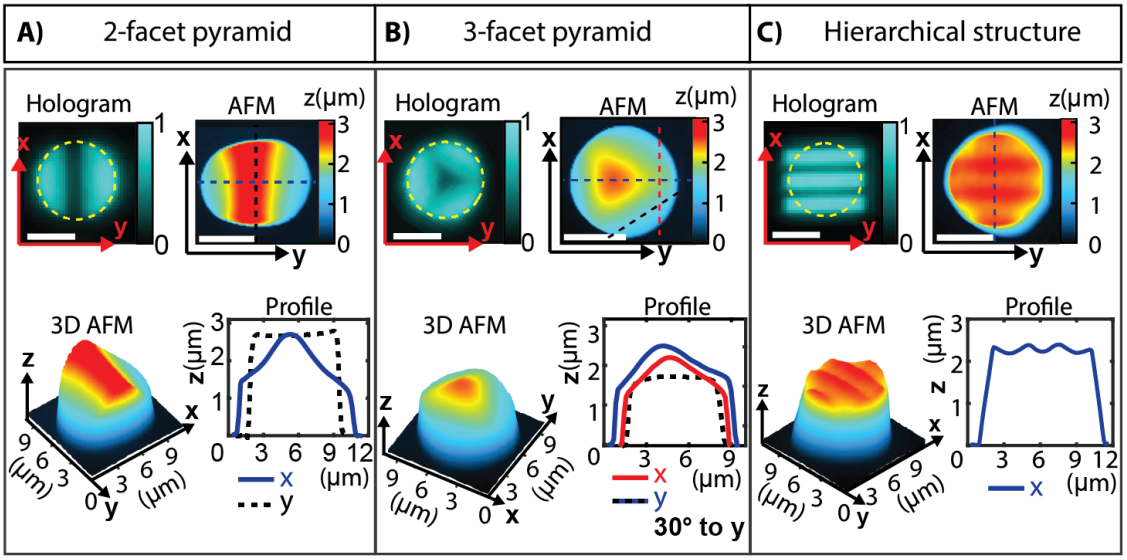

Figure 3.6 Facet-type and hierarchical-type of complex microstructural morphologies: pyramid-like microstructures with (A) 2-facet and (B) 3-facet after 15 s exposure, and (C) hierarchical grating-like morphology after 5 s exposure. All microstructures, characterized by AFM, were produced with the corresponding hologram, shown in the top-left image of each panel. White scalebars corresponds to 5 μm.

Another category of geometry that can be molded from the azopolymer micropillars is characterized by multifaceted designs, as shown in Figure 3.6(A–B). Each facet is a unidirectional intensity gradient that evolves from the minimum intensity at the center

of the circle to the maximum intensity at the perimeter of the circle. This design enables the creation of multiple slanted facets, such as the 2-facet micro-pyramid shown in Figure 3.6(A) and the 3-facet micro-pyramid shown in Figure 3.6(B).

The hologram design could be extended to more complex patterns, thereby further widening the range of achievable geometric diversity. To illustrate this potential, Figure 3.6(C) depicts an example of a hierarchical grating-like texture generated on the surface of the micropillar by a multi-line hologram. The flexibility of the CGH system allows for the generation of more complex patterns (*30*, *31*, *70*). The ultimate limit is determined by the spatial resolution and the gradient strength achievable in the hologram, which are primarily influenced by the characteristics of the SLM, including the number of pixels, the pixel size, and the size of the modulating display.

In comparison to the typical polarization-based strategy (e.g., the study in Chapter 2 and previous studies summarized in Chapter 1.4), the unique architectural features that arise from the local intensity gradient approach are not feasible. The distinctive characteristics derived from intensity gradient-induced deformation can be conceptualized as a deterministic local height modulation across a single microstructure. Despite the fundamental mechanics of intensity gradients of light with circular polarization lacking directionality, the aforementioned demonstrations illustrate that asymmetrical features can be induced by meticulously designing 2D holographic intensity patterns to impart an asymmetric force to the initial microstructure.

3.3.4 Blazed microstructures

As illustrated above, the introduction of an unbalanced driving force across the micropillar can induce an asymmetric architectural configuration. A specific kind of functional asymmetry that can be found on surfaces is a blazed structure, which is a structure that has a facet that is oriented at an angle relative to the normal surface. An example of this can be seen in blazed gratings (*78*). In fact, the fabrication of such architecture in micrometer and submicrometer scale is not straightforward (*79*).

In this study, a grayscale design with a linear gradient from grayscale value 0 at one end to 255 at the other end was used to produce a blazed surface on a micropillar array. Figure 3.7(A) illustrates a series of disparate distributions of bright and dark regions within the linear grayscale gradient. A distribution of 50% represents a balance between the two extremes, with 0 occurring precisely at one side of the micropillar's top perimeter and 255 occurring at the other. Figure 3.7(B) depicts the atomic force microscopy (AFM) morphology of eight distinct micropillars following exposure to the corresponding patterns. These variations demonstrate the straightforward control over

the portion of the micropillar that becomes a slanted facet. A smaller balance percentage results in a smaller partial deformation of the micropillar. In general, a balanced distribution, such as 40-50%, as observed in this study, produces a single slanted facet that utilizes the entire top surface of the micropillar. This deformation tilts the top surface of the micropillar into the direction of the linear gradient of the grayscale pattern.

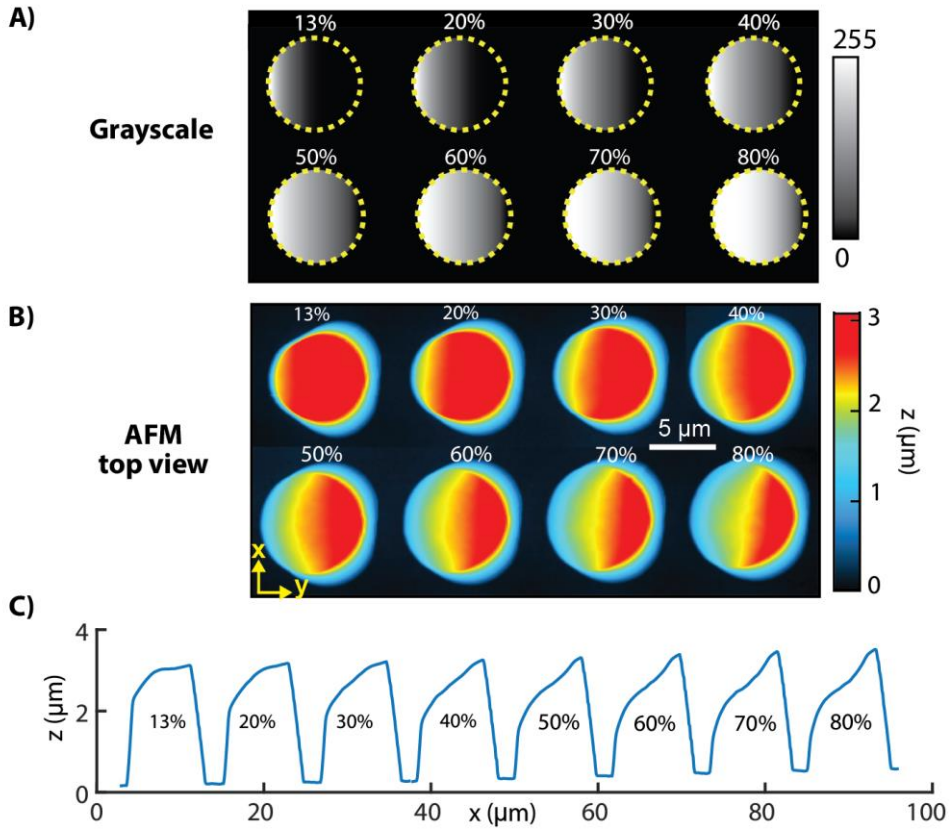

Figure 3.7 The slanted microstructure with different degrees of deformations. (A) Grayscale pattern of linear gradient with varying distribution of bright/dark portion. (B) AFM morphology of the micropillars after exposure to the hologram patterns produced from the corresponding grayscale patterns after 5 s. (C) The profile of the corresponding AFM morphology.

By demonstrating that the linear gradient of a grayscale pattern can "tilt" the top surface of a micropillar depending on the direction of the gradient of the grayscale, it is possible to achieve a deterministic localized rotation of the slant surface direction. To achieve this formation, an array of linear gradients of grayscale patterns with varying relative directions was designed and presented in Figure 3.8(A). This array is designed to

produce the corresponding holographic patterns that illuminate four micropillars in a row. Figure 3.8(B) depicts the atomic force microscopy (AFM) morphology of the reshaped micropillar array. Each was successfully formed into a slanted microstructure with its own relative directions. Figure 3.8(C) provides a closer examination of a slanted microstructure, confirming the rationale behind the linear gradient of grayscale pattern.

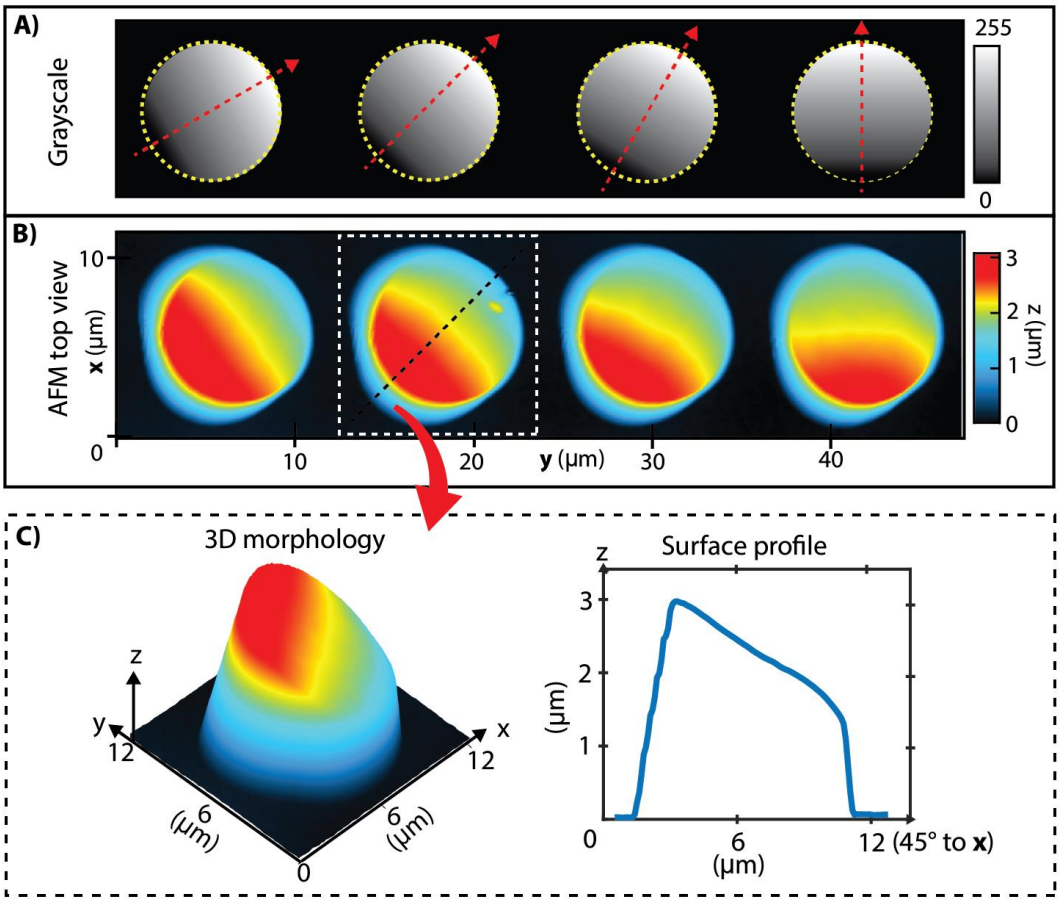

Figure 3.8 The array of rotating slanted microstructures. (A) The grayscale pattern of linear gradient with varying relative angle of the gradient direction. (B) The AFM morphonology of slanted microstructures with different relative directions. (C) The detail observation of a slanted microstructure (AFM 3D view and its profile).

3.3.5 Accurate group-selective capability

The utilization of holographic-induced reshaping on azopolymer-based micropillars has previously been employed to create micro-architectures with intricate designs

(*geometrical complexity*). Additionally, the modification of hologram designs has enabled the production of distinct geometrical shapes (*geometrical diversity*).

It is noteworthy that the holographic configuration enables all types of light-induced reconfigurations to be performed simultaneously for each micropillar within the field of view (FoV) of the optical system (with a diameter of approximately 200 μm in our setup) with a single exposure. The pillars within the field of view can be individually reconfigured by an independent portion of an extended hologram, designed with a desired distribution of light gradients. This capability enables the deterministic reshaping of a group of micropillars with individual structural diversity. In other words, this capability allows for localized-group selectivity, which represents an additional aspect of this approach.

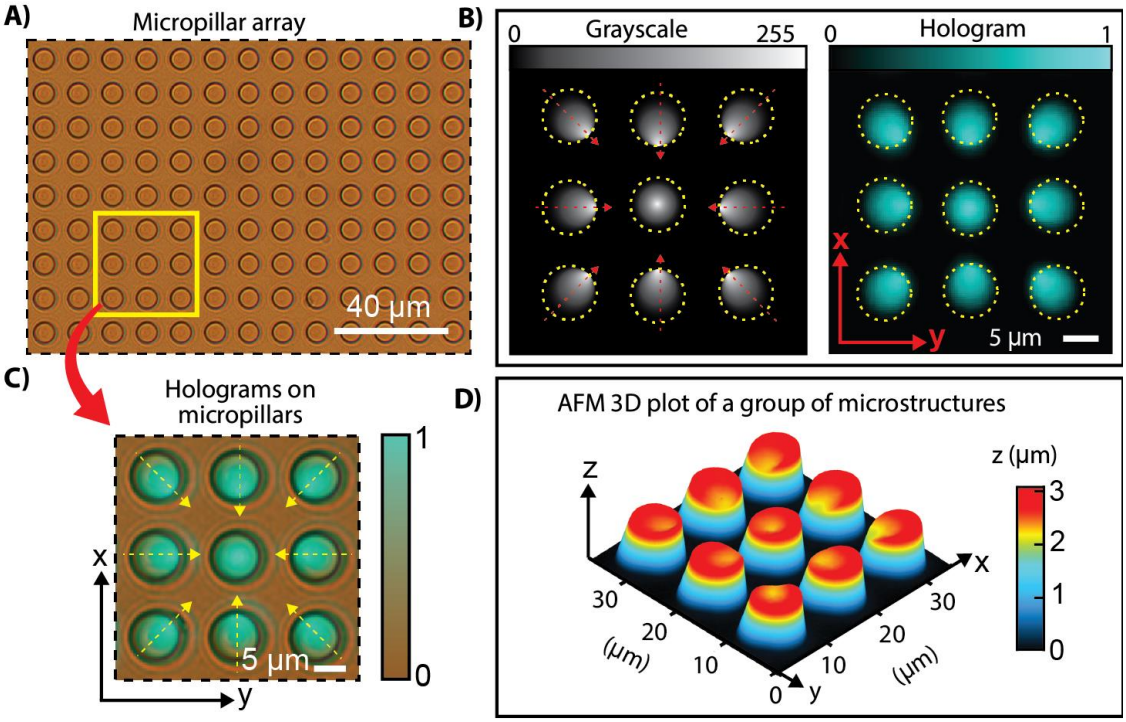

Figure 3.9 Group-selected reconfiguration with different directional morphologies. (A) Brightfield optical image of the pristine microstructure array. The yellow box highlights the region of interest to be reshaped. (B) The grayscale image (design) and the corresponding experimental hologram consisting of a group of asymmetrical circular patterns with different relative gradient directions. (C) The optical image of the selected group of micropillars, illuminated by the hologram. (D) The AFM of the reshaped microstructures after being exposed to the hologram for 5 s.

As illustrated in Figure 3.9(A), the image obtained through brightfield microscopy depicts a region of the initial micropillar array. A group of micropillars may be selected at random from any region of interest. For example, a group of nine neighboring micropillars, as indicated by the yellow box in Figure 3.9(A), has been selected for demonstration purposes. A hologram comprising nine patterns with varying intensity gradients was designed to align with the position of the micropillars (Figure 3.9(B)) and was projected onto the selected azopolymer sub-array (Figure 3.9(C)).

Figure 3.9(D) shows a three-dimensional AFM image of the reconfigured microstructures resulting from holographic irradiation. The final microstructures, as designed, consist of eight slanted concave microstructures with surfaces tilted in different relative directions and one symmetrical concave microstructure in the center.

In the context of the limited range of feasible geometries, a comparable simultaneous group-selective structural diversity on azopolymer microstructures is not accessible with any other optical configuration that has been documented to date. This includes homogeneous single-beam, multistep/multi-beam exposure, and scan-based spot illumination (*32*, *34*, *35*, *75*, *80*). It should be noted that the selective control offered by our holographic reconfiguration could be directly extended to larger areas (beyond the diameter of our current configuration of approximately 200 μm) by using objectives of higher numerical aperture with lower magnification, coupled with high-resolution SLMs. Furthermore, the use of tiling and stitching of the surface through motorized stages allows for the exploration of even larger areas in the range of cm^2, which could be utilized for macroscopic applications.

4 Vectorial Field-Guided Lithography:

Guiding mass migration locally using spatially rotating polarization for micro-architectures with robust orientational features

Photolithography techniques typically employ a variety of light-matter interactions. As discussed in Introduction, two properties of light, namely intensity and wavelength, are well-known for their significant roles in regulating light-matter interactions in conventional photo-responsive materials. The intensity of light represents the primary parameter that can be manipulated to induce surface patterns (*1*, *2*). For example, from mask-based photolithography to induce a spatially controlled polymerization of a photoresist surface by embedding intensity image to the light with physical mask. Another example, direct laser writing, relies on regulating an intense focused beam to induce two-photon absorption-based polymerization. The wavelength of light plays an intrinsic role in the interaction of light with photoresist materials, which exhibit wavelength-dependent absorption.

The aforementioned examples illustrate that, thus far, the available strategies for surface patterning have primarily focused on scalar properties of light, in particular, intensity and wavelength. The polarization of light, associated with the vectorial nature of light, remains mostly unexplored to the surface micropatterning community. One potential explanation for this is the rarity of polarization-sensitive materials useful for conventional lithography (*1*). Azopolymers are renowned for their distinctive photo-mechanical response when exposed to light, which is greatly dependent on the intensity distribution and the polarization of light. This phenomenon has been extensively discussed in previous chapters. Chapter 2 provides a clear illustration of how an azomaterial system can directly capture the directionality encoded in the polarization of the light through the directional reshaping of a system of micropillars.

This chapter has a goal to use the ability of azopolymer-based microstructures to capture the vectorial property of light with unprecedented spatial control. Here, a new strategy to create unconventional micro-architectures on surfaces, which will be called “vectorial field-guided lithography”, is introduced. This technique relies on the use of a

SLM acting as a polarization rotator which is employed by Dr. David J. McGee's laboratory at The College of New Jersey for azopolymer surface patterning (*43*, *81*, *82*). The entire study reported in this Chapter was conducted in that laboratory and forms the basis of an ongoing publication.

4.1 Polarization Rotator and Vectorial Field-Guided Lithography

4.1.1 Polarization rotator

The polarization rotator is an optical system that can impart a spatially rotating linear polarization with any distribution pattern in the wavefront of an incoming beam. Figure 4.1(A) depicts the configuration of the polarization rotator employed in this work. The polarization rotator consists of three main components, arranged in a sequence: the first quarter waveplate (QWP1), a spatial light modulator (SLM, Meadowlark Optics, Inc., phase-only, 1920 pixels in the *x*-direction and 1152 pixels in the *y*-direction), and the second quarter waveplate (QWP2).

In practice, the emitted linearly polarized (along with the *y*-axis) laser beam at λ=488 nm (Coherent Sapphire 488 LP), first pass through QWP1. The fast axis of QWP1 is aligned at an angle of 45° with respect to the *y*-axis, producing a homogenous circularly polarized beam. The fast axis of QWP2 is set at a right angle to the fast axis of QWP1. The SLM situated between the QWPs can be regarded as a matrix of variable phase retarders, dynamically controlled by a computer. The principal work of SLM matrix is that it can only impart a phase delay to the polarization component of light aligned with their fast axis (in this experiment is set parallel to *y*-axis). In this configuration, each pixel of the SLM screen reflects and modulates the incoming beam from QWP1, thereby introducing a phase difference between the two linearly polarized components with spatial control. The phase difference induced by an SLM pixel can be controlled by the applied voltage, which can be assigned by providing a grayscale (GS) value (0–255) as the screen input. The beam reflected from the SLM pixel passes through QWP2, which then converts the phase difference into a rotation of the linear polarization direction relative to the initial polarization direction. In this configuration, the QWP1-SLM-QWP2 setup behaves as a spatially-selective polarization rotator (*43–46*). In this study, the SLM is programmed to provide a polarization rotation of 2π with discrete steps of 1.4°, which corresponds to each of the 256 GS values addressable on the 8-bit SLM. As each pixel of the SLM screen can be assigned to any GS value, a spatial variation of polarization rotation from 0 to 2π can be imparted across the front wave of the beam that is directly reflected from the SLM active screen.

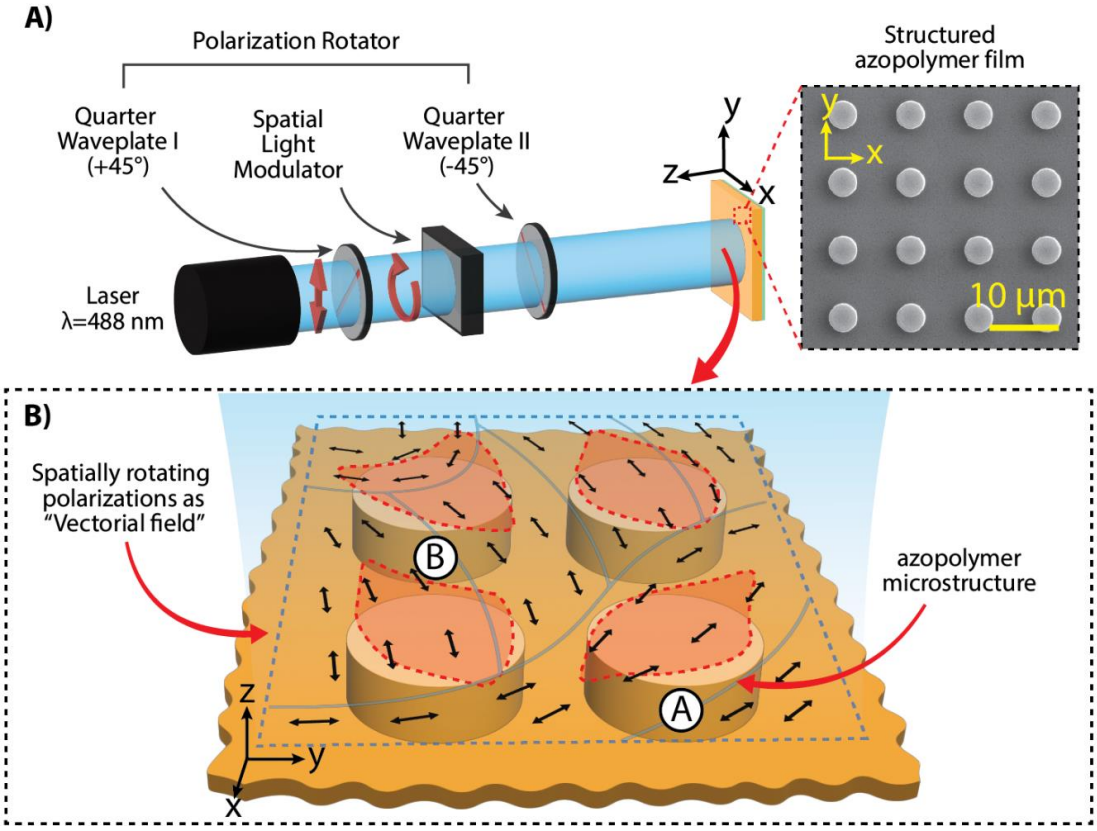

Figure 4.1 The polarization rotator setup and vectorial field-guided lithography. A) The simplified schematic of polarization rotator setup and the morphological image of the micropillar array. B) The artistic illustration of vectorial field-guided lithography.

4.1.2 Vectorial field-guided lithography

To grasp the idea behind the concept of vectorial field-guided lithography introduced here, it is first necessary to direct one's attention to the surface of a pre-structured azopolymer film. Figure 4.1(B) depicts the schematized interaction between a portion of a structured beam wavefield, characterized by a locally varying direction of the linear polarization, and a group of micropillars. To simplify this description, it is more straightforward to localize the interaction between the light field and the micropillar in the plane (*x*-*y* plane) that coincides with the micropillar's top surface. The wavefield with a spatial variation of the polarization rotation at this plane essentially provides an orientationally varying lateral driving force for the mass migration of the azopolymer within the micropillars, similar to the description given in Chapter 2. This allows for the spatially varying polarization rotation to be designed as a "guiding pathway" for mass migration with any arbitrary pattern of "pathways".

To illustrate this concept, let's first consider a single micropillar in Figure 4.1(B) (marked as A). In this example, the guiding pathway is designed as a connected linear trajectory, characterized by smoothly and continuously varying linear polarization (black arrows). In this design, the polarization of light on a single micropillar can be considered approximately homogeneous. Consequently, when the polymer is illuminated with this field, the micropillar's top surface begins to deform laterally on both sides. It is essential to grasp that photodeformation is a dynamic process. During photodeformation, the micropillar undergoes a continuous extension and reaches new coordinates in the *x*-*y* plane, as long as the illumination exists. When the extending portion of the micropillar encounters a new direction of local polarization, it will follow the current polarization direction. The effect is the same as illustrated for a group of several micropillars deformed by a homogeneous expanded beam in Chapter 2. The difference here is that each micropillar can be addressed with a different and independent guiding pathway. Furthermore, the configuration can be extended to more complex guiding pathways, as illustrated in area B of Figure 4.1(B). In this example, the guiding pathway is set to have three orientations relative to a single micropillar, which drives the surface deformation of the micropillar along the three axes dictated by the local polarization direction, eventually giving rise to a triangle-like microstructure. The ability to implement even more complex configurations of guiding pathways for the mass transport in a single pillar depends on the spatial resolution of the optical system with respect to the size of pillar, ultimately determined by the number of SLM pixels and the projection optics for the vectorial light pattern on the polymer film.

The following paragraphs will demonstrate several practical strategies of this new vectorial field-guided lithography for the fabrication of complex microstructures through the light-induced reconfiguration of azopolymer microvolumes. Each strategy encompasses the exploitation of the effect at different spatial scales (from homogenous collective to arbitrary single pillar deformation) and offers varying degrees of structural complexity for diverse functionalities and potential applications in the future.

4.2 Large Scale Formation of Directional Microstructures

The vectorial field-guided lithography offers a wide range of possibilities for directional surface patterning. One such approach is the fabrication of large anisotropic surfaces with flexible directional microstructures. In the simplest implementation of this method, the beam size emerging from the polarization rotator setup (Figure 4.1(A)) is configured to cover an area exceeding 5 mm × 5 mm, compatible with the typical size of the pre-patterned array of micropillars produced by soft molding. This configuration enables the production of a large functional surface with tailorable asymmetry in a single exposure.

This configuration can be regarded as a direct extension of the conventional reconfiguration strategy with homogenous polarized beams described in Chapter 2.

Figure 4.2(A) illustrates a basic spatial polarization configuration that partitions the active wavefield of the reflected beam from the SLM into six adjacent areas with distinct polarization rotations. The relative rotation of the polarization vector with respect to the *y*-axis is defined as **φ**, with the clockwise rotation signed as "+" and the anticlockwise rotation signed as "-". This definition will be used throughout this chapter. While the polarization rotator in this study can introduce a range of polarization rotation from **φ** = 0 to **φ** = 2π (equivalent to the GS level 0 to 255), the linear symmetry of light polarization allows for the use of only the range of rotation from **φ** = 0 to π, which encompasses enough rotation angles for the majority of cases.

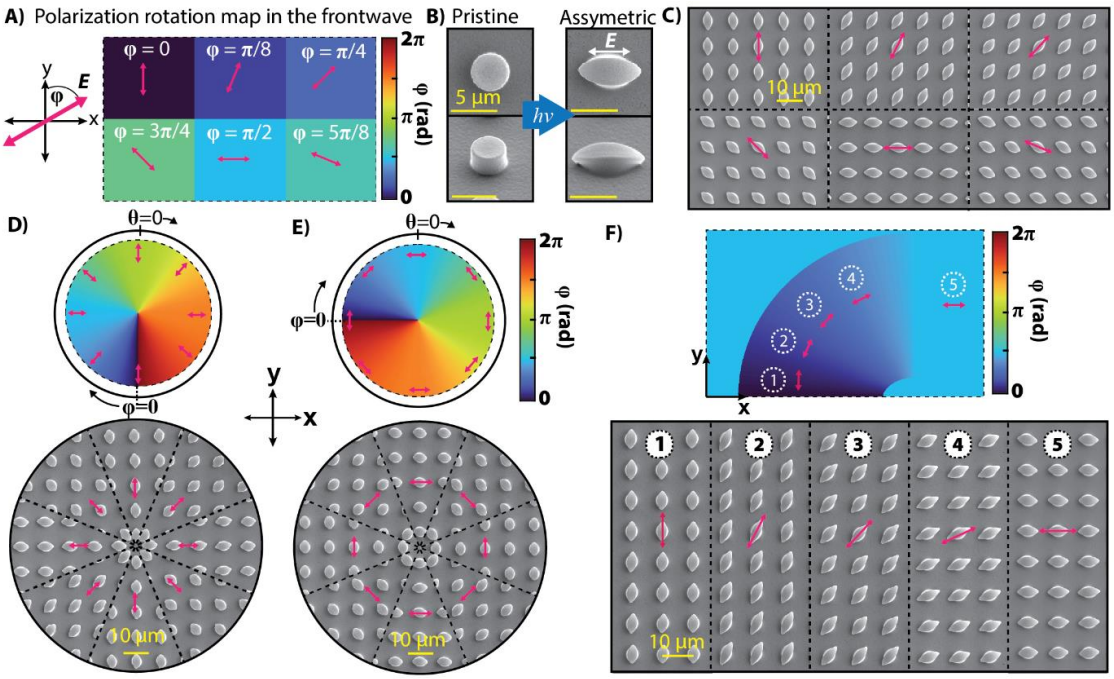

Figure 4.2 The large-scale patterning strategy of vectorial field-guided lithography. (A) Polarization map of six boxes pattern and the definition of polarization rotation angle (**φ**). (B) The morphology of an individual micropillar before (pristine) and after illumination (asymmetric shape) with a linearly polarized light, viewed from the top and the inclined angle (45° respect to the surface plane). (C) The surface morphologies after the illumination from six boxes polarization pattern. The gradual rotating polarization maps and their corresponding surface morphology images: (D) radial rotation and (E) azimuthal rotation pattern. (F) An arbitrary polarization map and its corresponding surface morphology image.

In the experiment of Figure 4.2(A), the active wavefield, which carries the “six boxes” pattern, covers an area of approximately 8 mm × 5 mm at the surface of the sample. It is notable that the entire active SLM matrix is composed of 1920 × 1152 pixels, which are then divided by a 3 × 2 box array in this pattern, resulting in each box comprising 640 × 576 pixels. This indicates that each box simultaneously illuminates a substantial number of micropillars. The designed micropillar array has a diameter of approximately 5 μm and a spacing of approximately 5 μm in a square formation (for further details, refer to the section on azopolymer synthesis and micropillar fabrication in Chapter 1.5). According to the phenomenology of the light induced reconfiguration of microvolumes described above, it can be expected that individual micropillars illuminated by each box will undergo uniform reshaping in a direction parallel to the local polarization direction. SEM (SU5000, Hitachi) images of a single micropillar belonging to the $\boldsymbol{\varphi} = \pi/2$ box (see Figure 4.2(B)) confirm this expectation by showing the typical elongated structure of a reshaped cylindrical azopolymer micropillar. Figure 4.2(C) illustrates the morphology of the entire micropillar array in each polarization box. The SEM images displayed in this figure were collected by sampling an area within each of the six boxes. These morphological results confirm the correspondence between the designed polarization pattern and the map of directional deformation of the microstructures. Although seemingly straightforward, the six-box polarization pattern already provides a glimpse over the significant advance that the proposed field-guided lithography offers over the conventional optical configurations with homogenously polarized Gaussian beams, drastically simplifying the fabrication of microstructures with spatially varying directionality. For comparison, the identical six-box pattern generated here requires six sequential exposures of a linearly polarized Gaussian beam, each assisted by a physical mask to produce the box pattern and an accurate mask-sample alignment.

Figure 4.2(D–E) illustrates an alternative type of polarization map for different spatial configurations of directional microstructures. The six-box polarization map provides an illustration of a discrete distribution of polarization rotation, whereas the demonstrations presented here offer examples of smoothly varying distributions of polarization rotation, with azimuthal and radial symmetries. The different polarization maps can be achieved by modifying the location of the line of reference ($\boldsymbol{\varphi} = 0$) with respect to the origin on the polar axis ($\boldsymbol{\theta} = 0$), the sign of the polarization rotation (clockwise or anticlockwise), and the total rotation ($\boldsymbol{\Delta\varphi}$). Figure 4.2(D) represents a radial polarization pattern, in which the reference line $\boldsymbol{\varphi} = 0$ is designed at $\boldsymbol{\theta} = \pi$ and a total rotation $\boldsymbol{\Delta\varphi} = 2\pi$. This polarization pattern allows to produce a directional microstructure matrix that points radially with respect to the center of the illuminated sample area. Figure 4.2(E) illustrates an alternative configuration of this pattern, with $\boldsymbol{\varphi} = 0$ at $\boldsymbol{\theta} = 3\pi/4$, resulting in an azimuthally oriented microstructure. Surfaces of azopolymer microstructures having

such cylindrical symmetry have been demonstrated using a beam with angular orbital momentum (*40*). However, such a scheme is limited by the static nature of the optical component (Q-plate) used to produce the engineered vectorial beam. The SLM-based polarization rotator discussed in this chapter can produce similar surfaces by designing the polarization maps digitally and implementing them through the SLM, which is intrinsically reprogrammable. This configuration does not require any modification of the optical setup when passing from one polarization map to another, drastically improving the flexibility over the currently used techniques.

Figure 4.2(F) further sustains this claim by demonstrating a large-scale rotating polarization map that mixes regions with azimuthal symmetry (areas marked with numbers 1–4) and regions of homogeneous linear direction (e.g. along the *y*-axis, marked with number 5), not realizable with other technique. The directional morphology of the deformed azopolymer microstructures observed by SEM in each area perfectly agrees with the design of the polarization map.

4.3 Localized Control on Individual Microstructures

The formation of directional microstructures on a large scale, as demonstrated in Figure 4.2, conceptualizes the structured surface as a polarization recorder. The effects of spatially varying polarization rotation can only be observed when the surface as a whole is considered. When observation is conducted in a limited area with a small number of micropillars, the micropillars show an approximately uniform reshaping in a specific direction. These kinds of surfaces are utilized in applications where the functionality of the surface is derived from the collective effect of the constituent microstructures over a large area, such as in wettability. However, many of today's applications favor a localized control over the architecture of a specific small group of microstructures or even a singular microstructure, such as in metasurfaces (*6*), surface information encoding (*83*), and microtrap device (*84*).

The vectorial field-guided lithography presented here can be extended to achieve localized surface reconfiguration control by adding an objective lens before the sample, as shown in Figure 4.3(A). With this configuration, the area of the active wavefield is downsized to an area of about 130 µm × 78 µm (Figure 4.3(B)), which is of the same order as the geometric parameters of the micropillar used in this study (diameter ≈ 5 µm, spacing ≈ 5 µm). Then, individual micropillar can be accurately associated with a particular polarization rotation, as shown in Figure (Figure 4.3(C)). In the experiment, the process of aligning a specific region in the illuminated field and a specific micropillar on the surface is performed using a bright-field imaging system with a CCD

camera and a motorized *x*-*y* stage. Focusing the beam onto the plane of the top surface of the micropillar is performed by carefully moving the sample the *z*-axis with a manual stage.

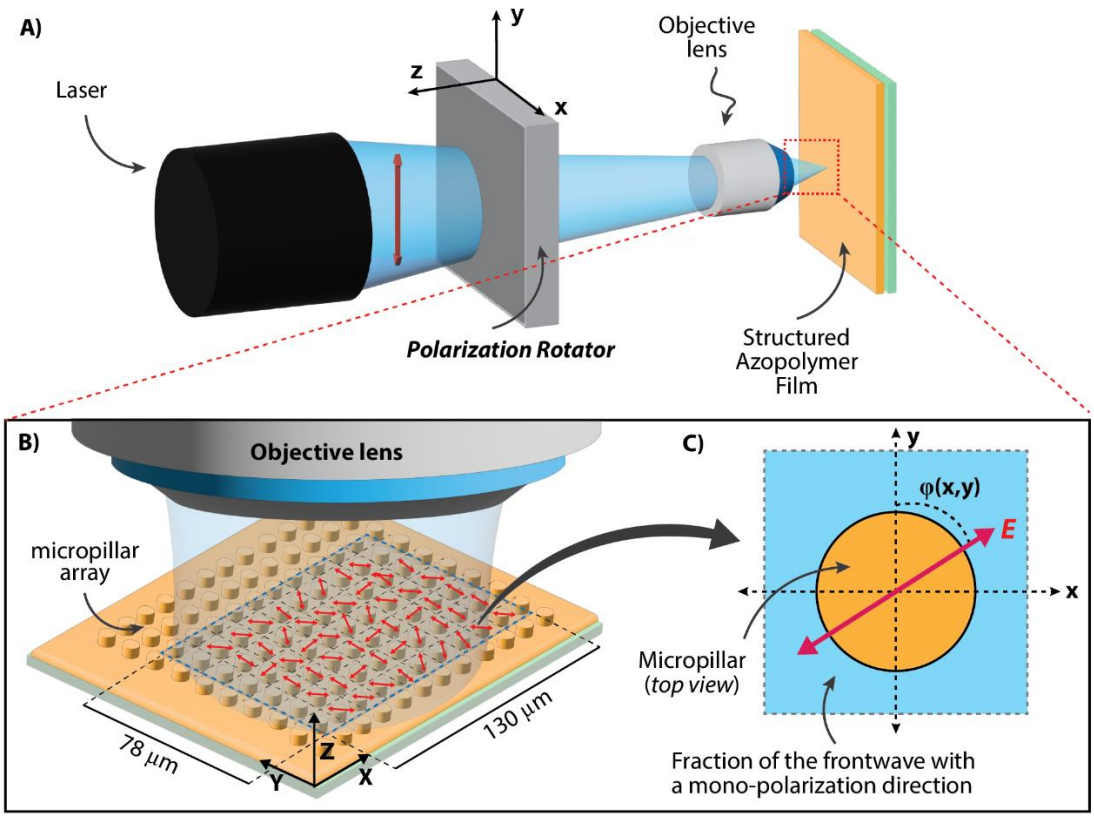

Figure 4.3 Strategy to target singular micropillars. (A) The simplified schematic of the polarization rotator with objective lens. (B) The artistic illustration of the scaled-down beam when reaching the micropillar array. (C) The illustration of a fraction of wavefield with a polarization rotation targeting a micropillar.

To highlight the capabilities of this strategy for increasing the complexity of the final surfaces, Figure 4.4(A) shows first the simplest polarization maps, i.e., homogeneous polarization direction over the entire field of view (left panel: $\varphi = 0$, right panel: $\varphi = \pi/8$). In general, the surface morphology of each polarization map variation shows the expected result where all micropillars within the field of view have been reshaped in the same direction. These formations can be seen as equivalent to the large-scale experiment (paragraph 4.2).

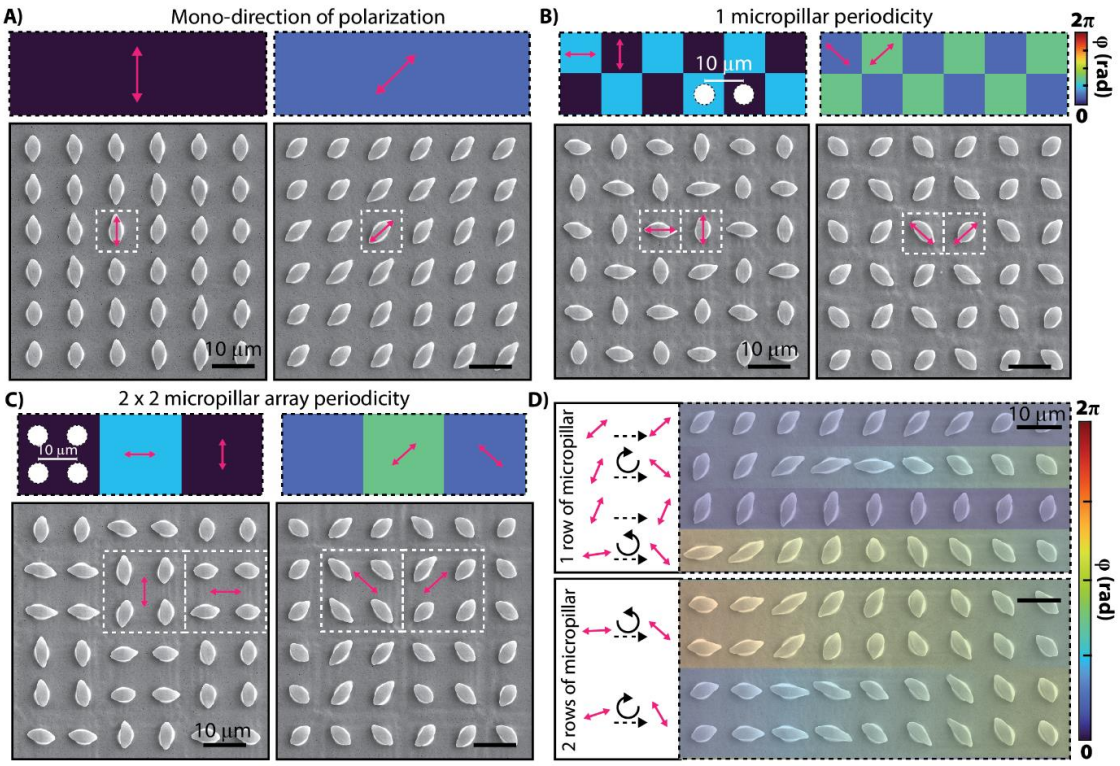

Figure 4.4 The surface morphology of the singular targeting strategy of vectorial field-guided lithography. The polarization maps and the corresponding surface morphology images: (A) Constant polarization rotation across the wavefield of the beam (left: $\varphi = 0$ and right: $\varphi = \pi/8$), (B) the checkboard polarization pattern with 1 micropillar periodicity and (C) 2-micropillar periodicity, and (D) micropillar-row targeting strategy.

However, Figure 4.4(B), demonstrates the real ability of this strategy to target a single micropillar. In this demonstration, a checkerboard polarization map is designed in which the periodicity of the tiles matches the periodicity of the micropillar array. Figure 4.4(B, left) shows that the alternation of one tile with $\varphi = 0$ and the other with $\varphi = \pi/4$, corresponding to horizontal and vertical polarization, respectively, produces a surface that has an alternating directional deformation, of the azopolymer micropillars. Another example, such as an alternating pattern between $\varphi = \pi/8$ and $\varphi = 3\pi/8$ (corresponding to $\mp$ 45° linear polarization), is also shown in Figure 4.4(B, right). The control can be extended not only for a single micropillar, but also for a particular group of micropillars, by extending the size of the pixel binning. For example, Figure 4.4(C) shows the same checkerboard polarization maps as in the previous example, but now each tile is designed to match a 2 × 2 micropillar array, resulting in a unique 2 × 2 periodic array of directional microstructures. As further demonstration of this strategy, Figure 4.4(D)

shows a combination of homogeneous and gradually rotating polarization maps, designed to match individual rows in the micropillar array. The polarization map (2nd and 4th rows) is designed to create a gradual rotation that is captured by the micropillar row, eventually forming a gradually rotating orientation of each microstructure along the row. Figure 4.4(D, below) shows a similar strategy, except that two rows are targeted for a gradual polarization pattern.

4.4 Combining Intensity and Polarization Patterns

The previous paragraphs have demonstrated the flexibility in controlling the directional properties of the azopolymer microstructures derived from the control of the polarization map in the beam, both on a large-scale (paragraph 4.2) and at the level of single microstructures (paragraph 4.3). Nevertheless, an intrinsic limitation of the polarization rotator configuration of this study is its impossibility to introduce spatial intensity variation in the vectorially tailored beam. In other words, the active wavefield area has an approximately homogeneous intensity distribution (assuming that the intensity profile of the original beam before reflection from SLM is also homogeneous), regardless of the polarization map imparted in the beam.

One possible solution to this limitation is the inclusion of a physical mask that can be placed after polarization rotator to introduce a spatial intensity variation mirroring the mask. By designing the mask to match with polarization map in the beam, a complex spatial polarization-intensity distribution can be produced. However, this solution will need a ton set of masks to accommodate any possible polarization map, which means extremely high cost, cumbersome alignment between mask and polarization map, and physically changing mask for each pattern.

In this approach, a less resource-intensive and economically viable strategy is proposed for introducing a combination of spatial polarization rotation and spatial intensity variation simultaneously. The strategy involves the incorporation of a rotatable linear polarizer (LP) within the beam’s trajectory following the polarization rotator, as illustrated in Figure 4.5(A). The underlying concept is to synchronize the linear polarization axis with the polarization map, whereby a portion of the wavefield is extinguished by the LP, while the remaining portion passes through, resulting in a polarization-based spatial filtering effect.

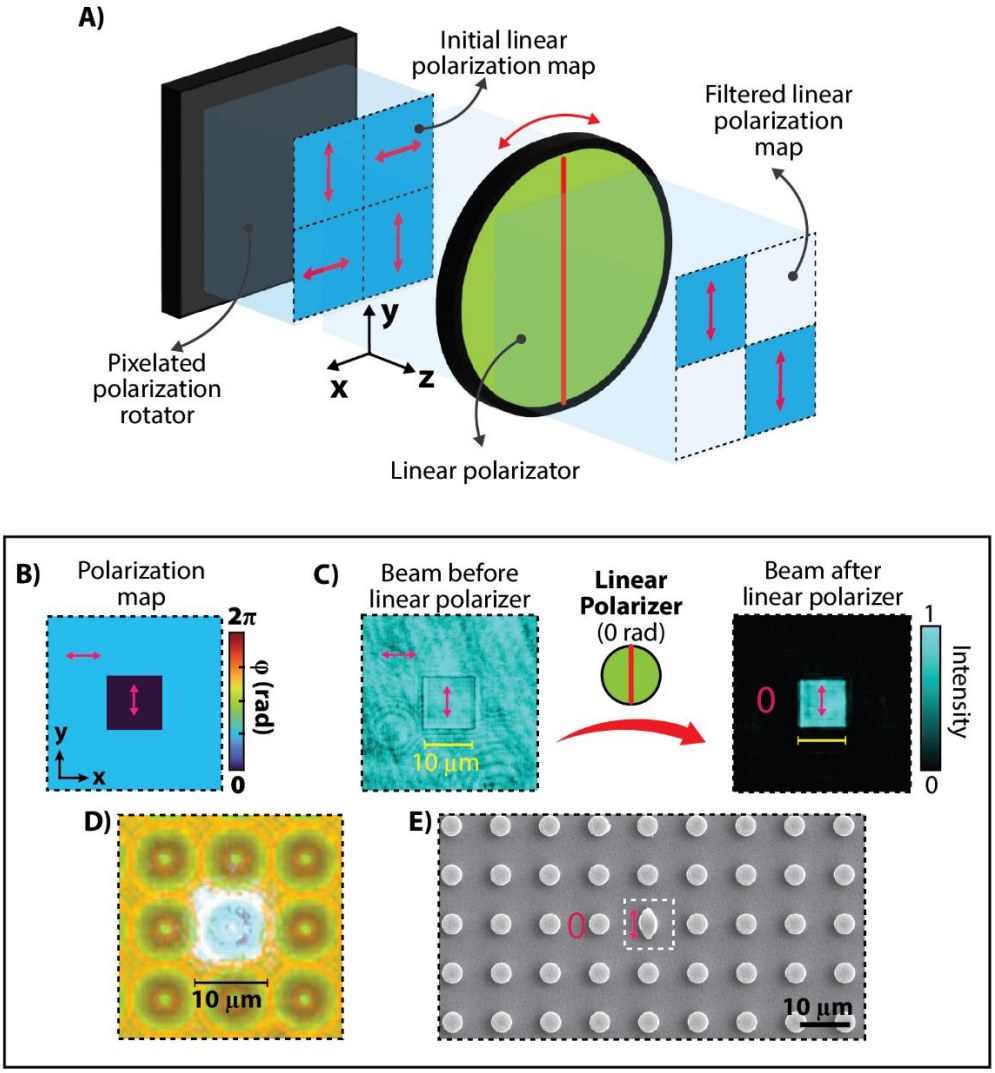

Figure 4.5 The polarization mask strategy. (A) The simplified schematic of the polarization mask configuration. (B) The polarization map designed to target a micropillar and (C) its corresponding beam image before and after the linier polarizer. (D) The filtered beam aligned on a micropillar. (E) The surface morphology of a reshaped micropillar after exposure to the beam.

The most straightforward application of the polarization mask within this study is the reshaping of a single isolated micropillar in an area that remains unaltered. This approach is illustrated in Figure 4.5(B–E). Figure 4.5(B) depicts a polarization map comprising a rectangular region exhibiting polarization rotation at $\varphi = 0$, designed to align with an area encasing a single micropillar. The remaining portion of the active wavefield is set to possess polarization rotation at $\varphi = \pi/4$. In its default configuration

(i.e., without LP), a homogenous intensity profile of the beam on the sample plane is obtained (Figure 4.5(C)). This corresponds to the polarization map depicted in Figure 4.5(B). When the LP is positioned with its transmission axis aligned along the direction of **φ** = 0, it generates a square-shaped intensity profile with polarization rotation at φ = 0, surrounded by null intensity everywhere (Figure 4.5(C)). Figure 4.5(D) provides insight into the alignment of the filtered wavefield and the micropillar array. Figure 4.5(E) displays the surface morphology of the reshaped single micropillar situated in the center of the field of view, while the surrounding micropillars remain unaltered.

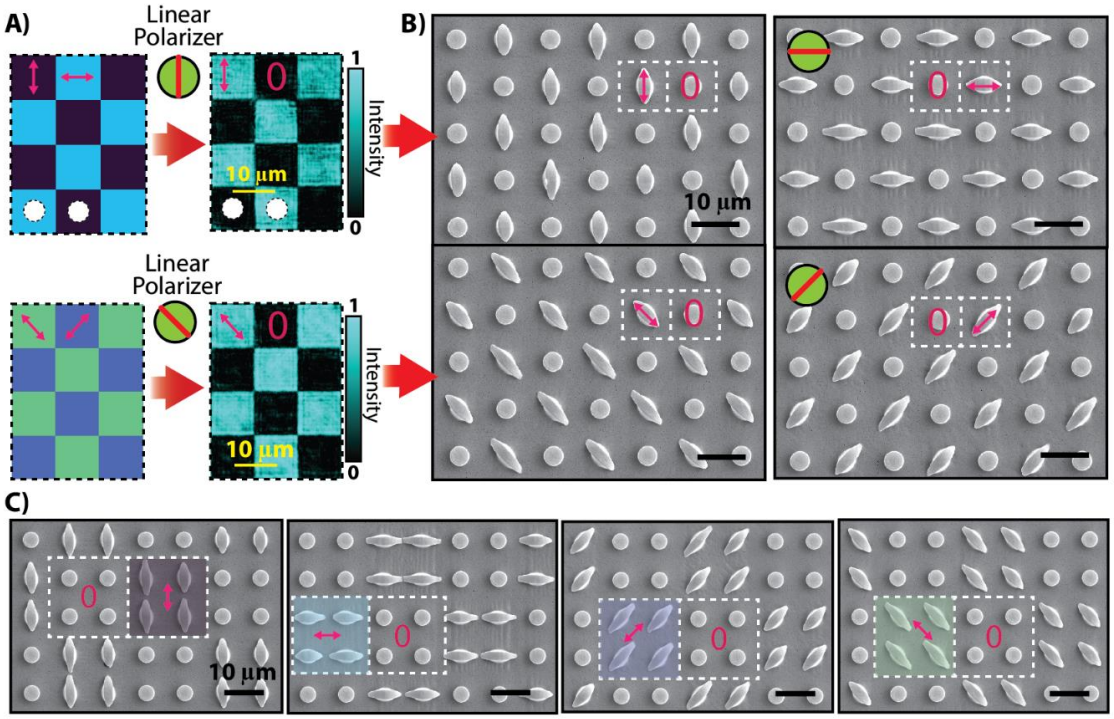

Figure 4.6 The checkerboard pattern combined with the polarization mask strategy. (A) Polarization map of checkerboard pattern and its corresponding beam image after passing through the LP. (B) The surface morphology images after the exposure with the filtered checkerboard polarization pattern. (C) The surface morphology images for 2 × 2 micropillar array periodicity.

Figure 4.6(A–C) presents another instance of a polarization mask strategy in vectorial field-guided lithography. By reusing the idea of checkerboard polarization maps, the polarization mask can be utilized to turn off one of the polarization rotations. Figure 4.6(A) depicts the initial polarization map design and the beam intensity profile on the sample plane after passing through the LP. The axis of LP can be aligned parallel to one

of the polarization directions, thereby producing a periodically alternating pattern of directional microstructures and original micropillars, as illustrated in the surface morphology images (Figure 4.6(B)). Figure 4.6(C) shows the scenario in which each tile is designed to cover 2 × 2 micropillar arrays.

4.5 Higher Complexity of Microstructure Deformation Maps by Multi-Step Exposure

The inclusion of a polarization mask strategy in vectorial field-guided lithography introduces an additional degree of freedom for the control of surface patterning. However, this strategy entails a trade-off, whereby the wavefield that reaches the surface exhibits a single polarization rotation. To reintroduce the flexibility of spatially varying polarization rotation while maintaining the spatial intensity variation, a straightforward solution is to use a series of sequential exposures for different axis orientation of the polarizer. The concept of sequential exposure is illustrated in Figure 4.7, where an arbitrary polarization map target composed of multiple discrete regions, each with its own polarization rotation and dimensions, is shown. In order to achieve the desired pattern, the target polarization map must be broken down into four sequential exposures. The key is to consider each polarization rotation as a distinct exposure. Figure 4.7(B) depicts the four sequential exposures corresponding to target map. For example, the area with horizontal polarization ($\boldsymbol{\varphi} = \pi/4$) can be considered the initial exposure. The target is placed in the same *x*,*y* coordinate plane as the initial polarization map, but the rest of the field of view is replaced with an orthogonal polarization direction with respect to the target bright area. The application of the LP (axis parallel to *x*-axis) effectively blocks the light outside the target box, thereby ensuring that the non-targeted micropillars remain unaffected. This same procedure can be applied to the remaining segments of the target map until all the spatially selective polarization patterns have been imparted to the surface, as illustrated in the surface morphology image in Figure 4.7(C). It should be noted that the number of exposures is solely contingent upon the number of targeted independent polarization directions.

A key feature of this strategy is the possibility to include non-deformed pillars as part of the design of functional surfaces. As an example, Figure 4.7(D–E) illustrates the multi-step exposure technique for the fabrication of periodic patterns of pillars reconfigurations that include, vertically and horizontally elongated, as well as pristine microstructures. In this situation, the target deformation map can be partitioned into discrete units (or cells) that exhibit homogeneous polarization direction and transferred on the surface morphology in two sequential steps. The SEM image in Figure 4.7(E) shows the result of the exposure sequence, confirming the production of the engineered

surface deformation map on the azopolymer micropillars. Figure 4.7(F) shows another example of the deformation map designed with a different scheme and deformation directions, further highlighting the flexibility of the method.

In general, the combination of the polarization masking and the multi-exposure strategy provides the ability to control the spatial localization of the directional morphology of microstructures. This is analogous to the effect of a sophisticated optical configuration that can simultaneously control the spatial distribution of polarization and intensity of the light. In practice, the addition of a rotatable linear polarizer and the implementation of multi-exposure do not result in a significant amount of movement within the optical configuration, similar to the state-of-the art of the configurations used for photo-alignment of liquid crystal cells (*44*, *85*, *86*). The changing of polarization maps is fully controlled by a computer, while the rotation of LP along its own axis can be automatically regulated and synchronized, for instance, with the use of a motorized rotator. Therefore, these extensions to the basic polarization rotator do not compromise the simplicity and compactness of the overall system, while offering an increased flexibility in the design of deformation maps on the surface.

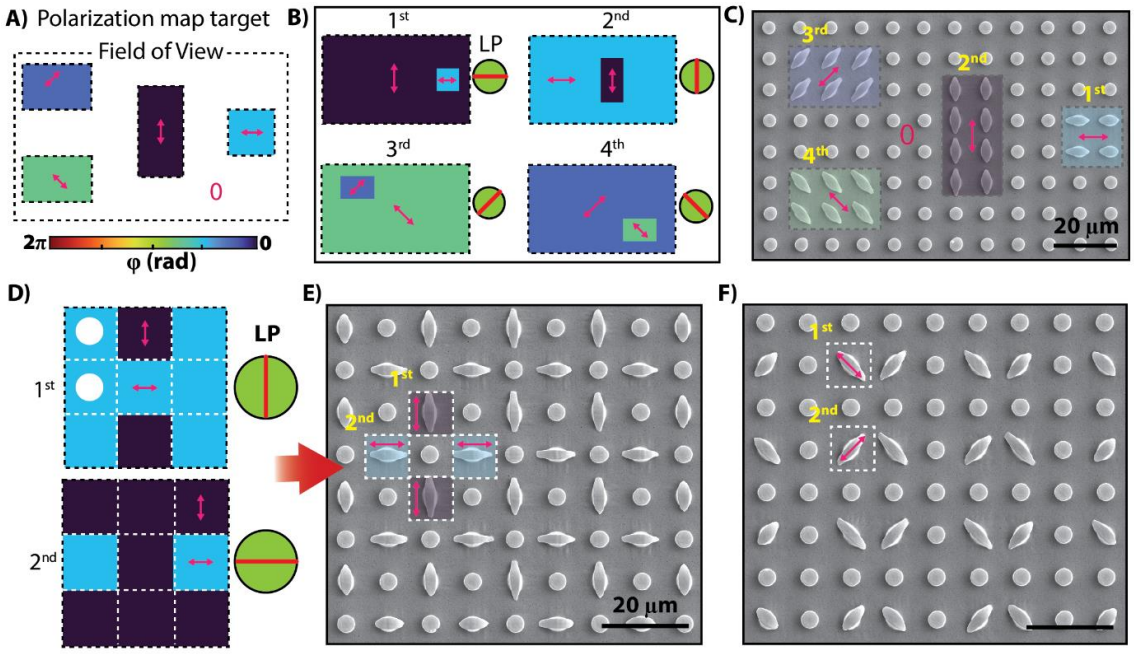

Figure 4.7 Multi-exposure strategy of vectorial field-guided lithography. (A) The polarization map target. (B) The breaking down of the polarization map target to four sequential different exposures. (C) The surface morphology image after the four sequential exposures. (D) The "cell" of the periodic polarization map for each polarization rotation. (E) The surface

morphology image after exposed to the 1st and 2nd exposure. (F) Another example of surfaces with multi-exposure for periodic patterns.

4.6 Micro-architectures with Strong Orientational Features

Thus far, the vectorial field-guided lithography has been shown to perform surface patterning in a highly localized manner, enabling the precise control of directional microstructure formation down to the level of single micropillars. These demonstrations are based on the idea of considering each micropillar as a programable pixel with a monodirectional deformation ability. Therefore, the objective of previous demonstrations has been to control the formation of these pixels as a two-dimensional array on the surface. However, the polarization-dependent stress induced by the light inside an azopolymer-based microvolume is built up from a molecular-level phenomenon, i.e., the alignment of the polymer backbones to the direction of polarization. As the typical size of the pristine pre-patterned azopolymer microstructures is in the range of a few microns and the minimum resolution of the SLM-based polarization rotator can be significantly higher than the microstructure size, we can expect that directional deformations can be independently triggered even in different localities of a single azopolymer microvolume.

Figure 4.8 provides a visual representation of the practical aspects of this idea. The optical configuration of the polarization rotator utilized in this experiment is identical to that employed in the experiments described in Chapters 4.3–4.5, as illustrated schematically in Figure 4.8(A). A micropillar array with a diameter ($\mathbf{D_o}$) of 8 µm and a periodicity ($\mathbf{P_o}$) of 12 µm (center to center distance) is utilized throughout this chapter (Figure 4.8(B) and see Chapter 1.5 for further details of the micropillar fabrication procedure). Figure 4.8(C) illustrates a high-resolution polarization map, achievable with the optical system used here, which varies across the plane of a single micropillar top surface. Given that the micropillars are arranged in a square array, each micropillar is targeted by a square polarization map with an area of $\mathbf{P_o} \times \mathbf{P_o}$, which comprises 178 × 178 pixels of the SLM.

As an initial illustration of the ability of this configuration in controlling the shape of a single pillar, Figure 4.8(D) depicts a gradual polarization rotation across the *x*-axis, which is replicated homogeneously along the *y*-axis. The design of the map consists of setting $\boldsymbol{\varphi}(x = 0) = 0$ (vertical polarization) and a linearly increasing clockwise rotation that produces $\boldsymbol{\Delta\varphi}(x) = +\pi$ at the other extreme of the addressed area, such that $\boldsymbol{\varphi}(x = \mathbf{P_o}) = \pi$ (vertical polarization again). Figure 4.8(E) illustrates the temporal evolution of the micropillar morphology at different steps of a light-induced reconfiguration experiment

from its original shape (**t** = 0) to a boomerang-like microarchitecture. An additional illustration of the polarization map with a similar concept is presented in Figure 4.8(F). In contrast to a continuous increasing rotation, which would complete a half rotation of the electric field, the polarization in this pattern is designed to rotate in a clockwise direction from $\boldsymbol{\varphi}(x = 0) = 0$ (vertical) to reach $\boldsymbol{\varphi}(x = \mathbf{P_o}/2) = \pi/2$ (horizontal) in the pillar center, and then in an anticlockwise direction to reach $\boldsymbol{\varphi}(x = \mathbf{P_o}) = 0$ (again vertical, but with reversed rotation dynamics). This polarization map results in the half-left micropillar being reshaped in a manner similar to a boomerang-like shape, while the half-right is reshaped in the opposite direction, forming a bi-petal microarchitecture (see Figure 4.8(G)). It is noteworthy that this structure exhibits a pronounced chirality feature that emerges from the reversed sign in the polarization rotation.

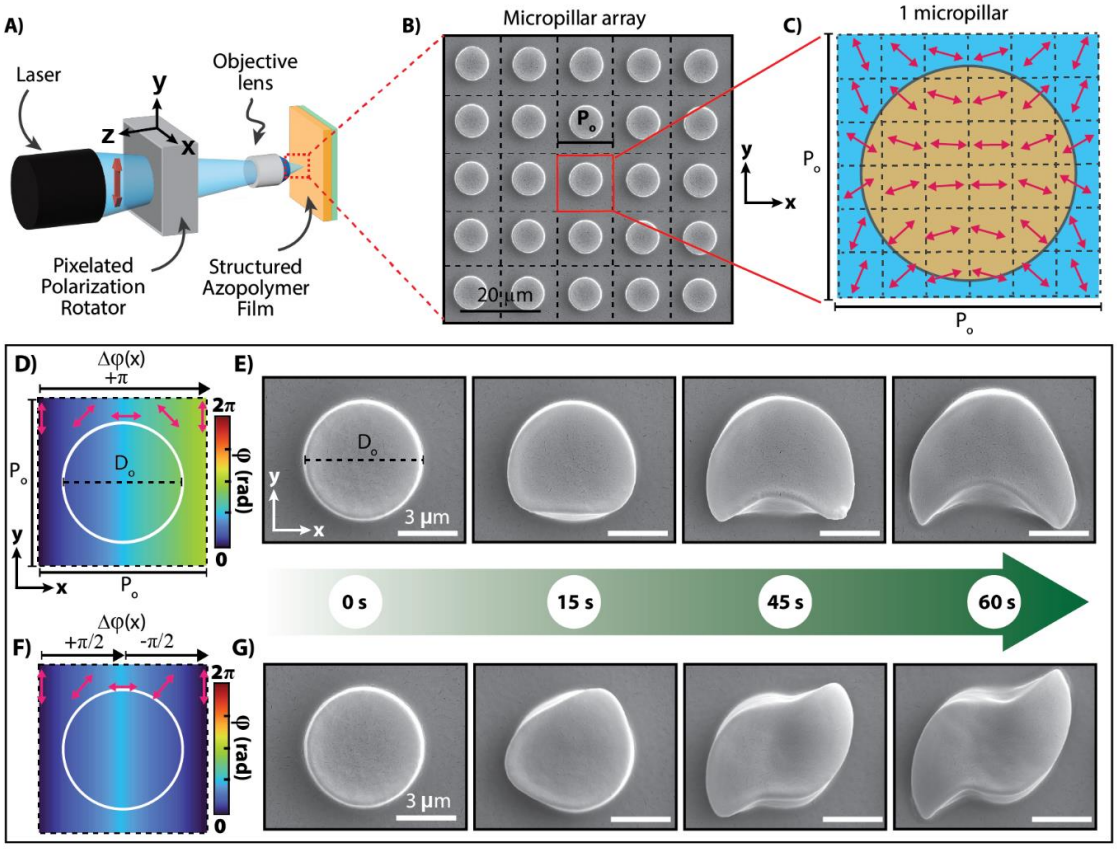

Figure 4.8 Vectorial field-guided lithography applied in a single microstructure. (A) The simplified schematic of the optical configuration. (B) The morphology of the micropillar array. (C) The artistic illustration of the varying polarization rotation across the lateral plane of a single micropillar. (D) The polarization map and (E) the evolution of the micropillar's architecture to boomerang-like shape. (F) The polarization map and (G) the evolution of the micropillar's architecture to bi-petal shape.

Additionally, the two examples in Figure 4.8 highlight a general feature of the vectorial field-guided lithography on a single micropillar. Depending on the sign (clockwise or counterclockwise), the spatially rotating polarization across the micropillar's diameter provides each portion of the micropillar's volume with opposite lateral driving forces. By rationally designing the polarization rotation as a function of the *x*-*y* coordinate, different parts of the micropillar can be guided in varying orientations to form unconventional architectures at microscale.

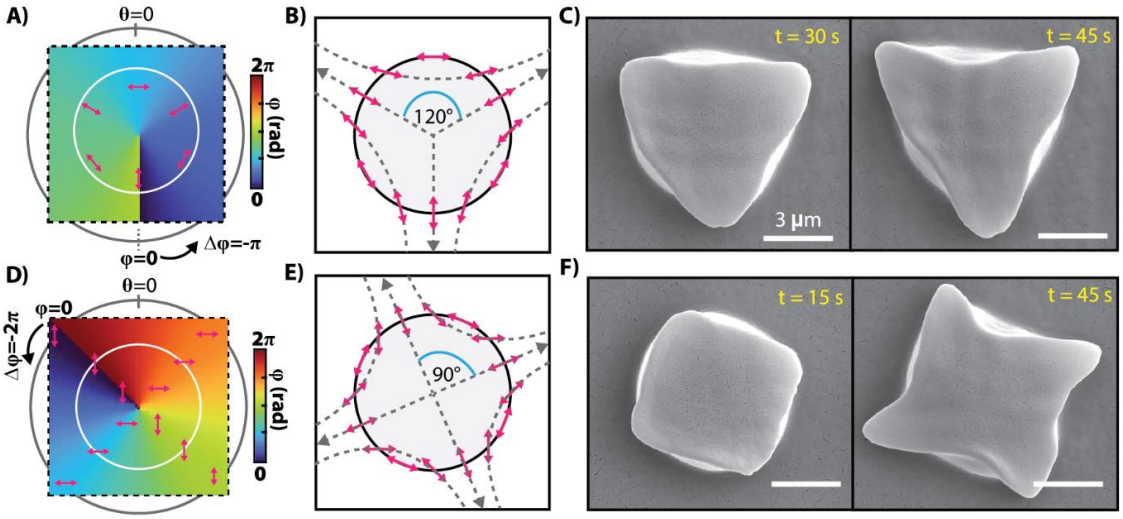

Figure 4.9 Guiding pathways with multi-axis system. (A) The polarization map and (B) the guiding pathways for the three-axis system. (C) The surface morphology of the tri-petal micro-architecture after different exposure times. (D) The polarization map and (E) the guiding pathways for the four-axis system. (F) The surface morphology of the tetra-petal micro-architecture after different exposure times.

To rationalize the connection between the polarization rotation and the morphology of reshaped surfaces, Figure 4.9 depicts two polarization maps characterized by tailored rotations of the polarization direction with respect to the center of the azopolymer micropillar. The polarization map in Figure 4.9(A) is constructed by initiating the rotation ($\boldsymbol{\varphi} = 0$) at $\boldsymbol{\theta} = \pi$, subsequently rotating it counterclockwise for a total rotation of $\boldsymbol{\Delta\varphi}(x) = -\pi$ while completing a full rotation along the polar axis. This polarization map defines mass migration guiding pathways with radially outward driving forces distributed at angles $\boldsymbol{\theta} = \pi/3, \pi$, and $5\pi/3$ (Figure 4.9(B)). Consequently, the micropillar is transformed into a tri-petal microarchitecture, as illustrated in Figure 4.9(C). Figure 4.9(D–F) illustrates a method for creating a tetra-petal micro-architecture with

pronounced chirality. In order to achieve this structure, the polarization rotation is designed to make a full rotation anticlockwise, with a value of $\Delta\varphi(x) = -2\pi$, with $\varphi = 0$ starting at $\theta = 7\pi/8$, as illustrated in the polarization map in Figure 4.9(D). This configuration results in the generation of four emerging driving forces that are orthogonal to the circular micropillar perimeter (Figure 4.9(E)). Therefore, the process ultimately breaks the circular symmetry of the original micropillar, resulting in the formation of a tetra-petal micro-architecture, as illustrated by the surface morphology in Figure 4.9(F). Interestingly, at a higher time exposure (t = 45 s), the tetra-petal micro-architecture shows a chirality feature in the anticlockwise direction. It is also noteworthy that the final shape of the micro-architecture is dependent on time. As the vectorial field-guided lithography is a dynamic process, the time exposure in the experiment can be employed as an experimental parameter to regulate the evolution of the micro-architectures, thereby controlling the morphology of the resulting structures. As illustrated in Figure 4.9(F), an exposure of 15 seconds results in a transformation of the circular micropillar shape into a square-like structure. However, a longer exposure period (45 seconds) is necessary to achieve the desired tetra-petal shape.

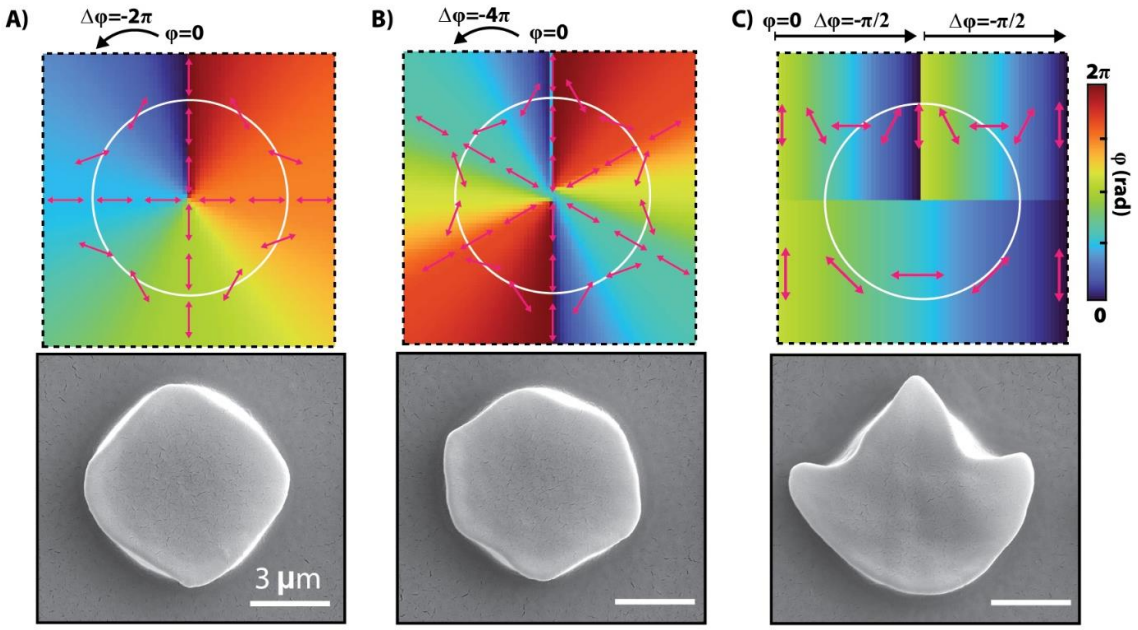

Figure 4.10 Other demonstrations of guiding pathways with multi-axis system: (A) symmetric square micro-architecture, (B) symmetric hexagonal micro-architecture, (C) shark-skin inspired micro-architecture.

Figure 4.10 presents a series of additional demonstrations on azimuthally rotating polarization maps. Figure 4.10(A) is analogous to the "tetra-petal" structure demonstrated above, but with the direction of the emerging driving forces coinciding at the *x*- and *y*-axes. The number of axes of the driving forces can be increased by increasing the rate of rotation of the polarization along the azimuth. In Figure 4.10(B), the polarization undergoes a two-fold anticlockwise rotation along the azimuth axis, with a total rotation of $\boldsymbol{\Delta\varphi} = -4\pi$. This results in the formation of six outward radial driving forces, evenly spaced at 60° from each other, which collectively give rise to a hexagonal morphology, as illustrated in Figure 4.10(B). It is noteworthy that the design is not constrained by linear or circular variations alone. In fact, a nonsymmetric polarization map can be devised to induce a micro-architecture reminiscent of micro-textures found on the shark skin, (*35*) as exemplified in Figure 4.10(C).

In order to extend the variety of microarchitectures that can be formed, the polarization mask strategy can also be applied. Figure 4.11 provides a summary of two examples of asymmetric microarchitectures, created through the combination of spatial polarization and intensity variation. The first example employs a binary pattern comprising two orthogonal polarization rotations: one half with horizontal polarization and the other with vertical polarization. This is illustrated in the polarization map in Figure 4.11(A). By applying the polarization mask with a linear polarizer (LP) axis parallel to the horizontal axis, the final beam exhibits a half-left polarization rotation along the horizontal axis with maximum intensity, and a half-right polarization rotation with null intensity. The alignment of this pattern is performed with the objective of targeting half of the micropillar. The beam's exposure guides the micropillar to undergo reshaping into an asymmetric microarchitecture, as illustrated in the SEM images in Figure 4.11(B). As usual, the degree of asymmetry can be regulated by controlling the duration of the exposure also in this case. A comparable approach, with a less pronounced asymmetric configuration, can be achieved through the implementation of a gradient instead of a binary intensity pattern. In this configuration, the polarization mask is designed to exhibit a constant polarization direction in one half of the pillar, while the other half has a gradual rotation until becoming orthogonal to the first one. This concept is illustrated in Figure 4.11(C) for a linearly increasing rotation angle of the polarization, which produces an intensity variation that follows the Malus's law ($I(x) \sim cos^2 x$). This illumination pattern deforms the left half of the micropillar to a greater extent than the right half, due to the difference in intensity. The surface morphology presented in Figure 4.11(D) illustrates this effect on the final microarchitecture. At a lower time exposure (t = 30 s), the effect is similar to that observed in the binary approach illustrated in Figure 4.11(B). At an exposure time of 60 seconds, the micropillar undergoes reshaping in both directions, with differing degrees of deformation and then of structural anisotropy.

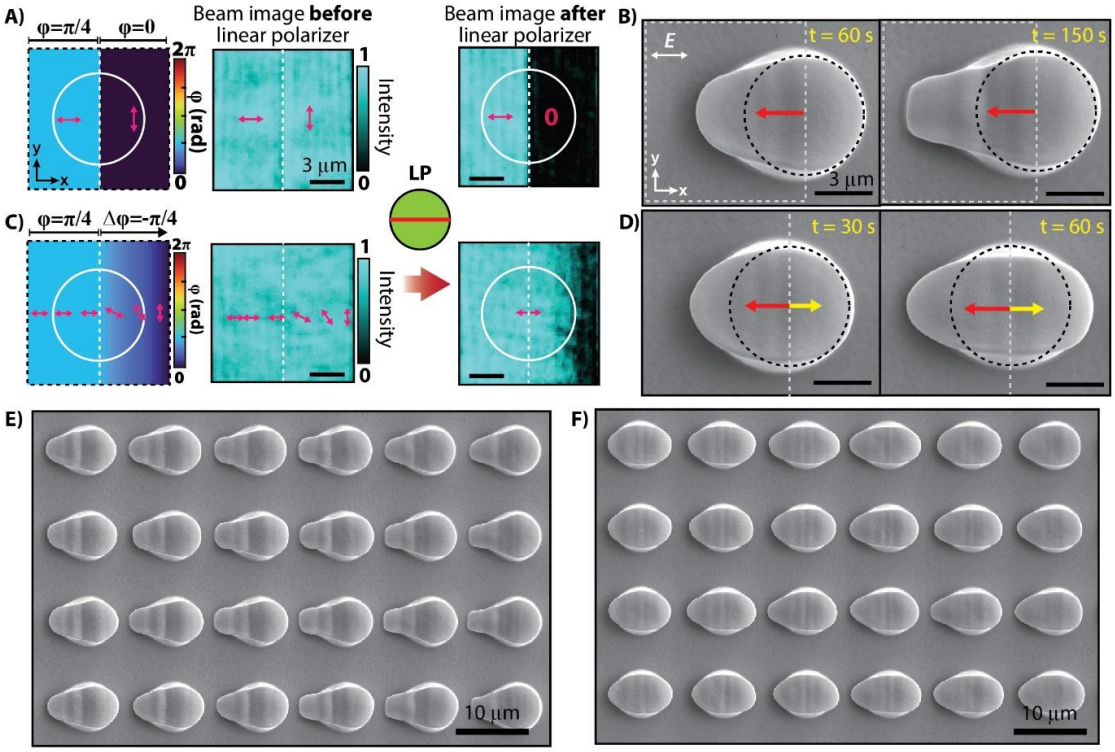

Figure 4.11 The asymmetric micro-architecture using polarization mask strategy. (A) The binary polarization map, its beam image before and after passing through the linier polarizer, and (B) the morphology of the asymmetric micro-architecture after illumination with different time exposure. (C) The gradient polarization map, its beam before and after passing through the linier polarizer, and (D) the morphology of the asymmetric micro-architecture after illumination with different time exposure. The surface morphology of the asymmetric microstructure array produced from (E) binary and (F) gradient approach.

Thus far, the focus has been on the development of unconventional micro-architectures at the individual level. In general, however, these kinds of micro-architectures demonstrate functionality through the formation of an array on the surface. To form an array with a repeating micro-architectural type, the strategy is simply to arrange the individual polarization maps in an array that matches the original micropillar array. As illustrated in Figure 4.12(E–F), the surface morphology of the asymmetric microstructure previously depicted in Figure 4.11(A–D) can be observed in the formation of an array. To illustrate further flexibility, the formation of these micro-architectures in the array can be tailored to have relative different orientations, as demonstrated in Figure 4.12. Figure 4.12(A) illustrates four orientation variations of the

bi-petal polarization map. To illustrate, each orientation is designated to target distinct rows of micropillars. Subsequent to the exposure of this pattern, an array of rotating bi-petal microarchitectures can be obtained, as evidenced by the surface morphology in Figure 4.12(C). The same strategy can be employed to form an alternating tringle-like microstructure formation in the array, as demonstrated in Figure 4.12(D).

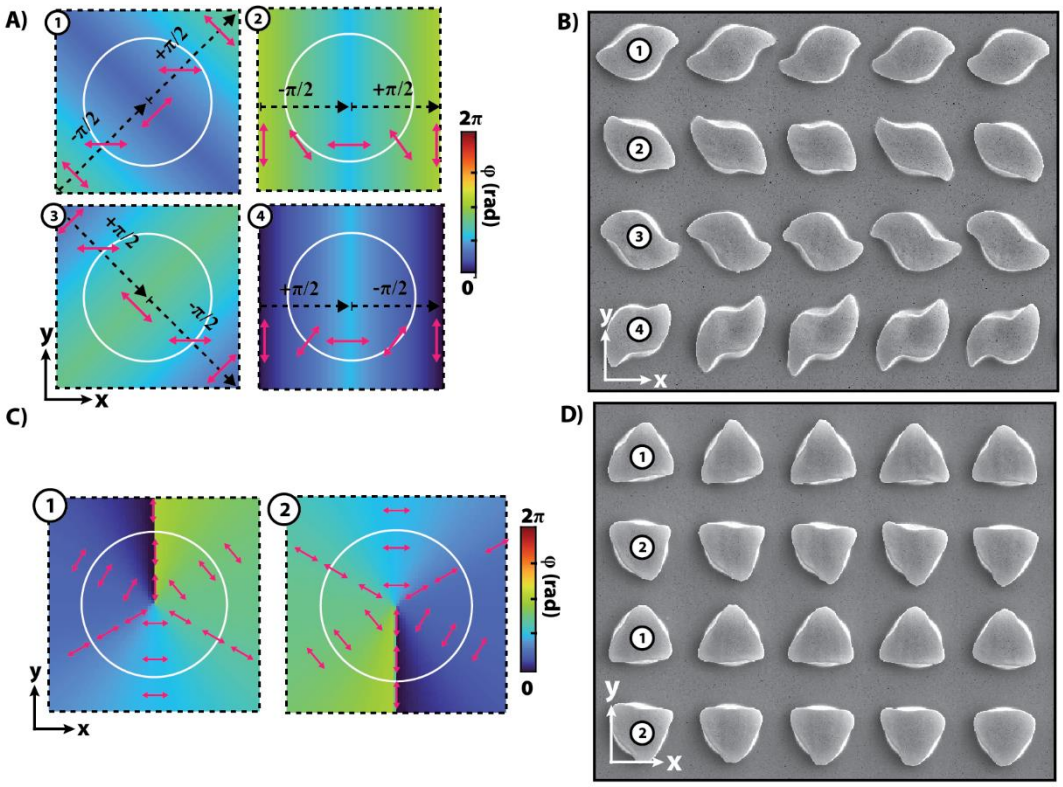

Figure 4.12 The variation of the orientation of the micro-architectures in the array. (A) Four different orientations of the bi-petal polarization map, and (B) the surface morphology of a rotating duo-petal microstructure array. (C) Two variations of the tri-petal polarization map, and (D) the surface morphology of an alternating triangle-like microstructure array.

Conclusion

The role of three-dimensional microstructures on surfaces is becoming a subject of increasing interest for fundamental sciences and technological applications, to a degree that has not been seen before. This is made possible by the advancement of microstructure fabrication techniques that combine different fields of science into an emerging and fascinating field of research. Azobenzene-embedded polymers (azopolymers) have emerged as a distinctive yet potent class of photo-responsive materials for surface patterning. Its potential arises from a light-driven mass migration resulting from a nano-photomechanical process wherein azobenzene molecules undergo a cyclic photoisomerization between their *trans*- and *cis*-state. The mass migration observed in azopolymers differs from the standard mechanism involved in photoresist-based photolithography. Firstly, the light-driven mass migration occurs at relatively low power levels and without any indication of ablative or thermal effects. Secondly, it is not a permanent process, as is the case with other photoresist materials that employ irreversible polymerization. This enables the implementation of distinctive pattering strategies, such as “erase-then-rewrite” and multiple pattern superposition. However, the most notable attribute of mass migration in azopolymers is its dependency on two characteristics of light: intensity and polarization. In essence, the mass migrates from an area of higher intensity to one of lower intensity. In addition to the intensity gradient, mass migration tends to follow the direction parallel with that of the dominant electric field component. A number of studies have employed the properties of the azopolymer-light interaction as a foundation for exploring a variety of strategies to induce diverse surface patterns for a range of applications, such as diffractive surfaces, reconfigurable holographic plates, diffractive color surfaces, and cells guiding.

The applicability of azopolymers for three-dimensional micro- and submicro-architectures on the surface has been demonstrated by a multitude of studies, which have collectively established a new subfield. The fundamental concept is to exploit a pre-existing microstructure on the azopolymer surface, created through soft lithography, prior to illumination. The presence of this pre-existing microstructure on the surface introduces discontinuity, enabling the surface to directly capture the vectorial properties of light (polarization). This concept has been employed in the development of diverse strategies involving various types of engineered fields of light and a range of

morphological shapes of pre-structured surfaces. This thesis explores this approach as the general theme, which then gave rise to three distinct strategies. Each relies on a novel concept for the production of complex three-dimensional architectures.

One strategy for reshaping three-dimensional azopolymer-based microstructures employs the effect of the field gradient when a beam propagates within the azopolymer microstructure volume. This phenomenon arises from the exponential attenuation of light in accordance with the Lambert–Beer law. This results in a distinctive photodeformation phenomenon occurring at the topmost layer of the microstructure, manifesting as an overhanging feature. Chapter 2 introduces the wavelength of the light, which corresponds to the penetration depth, as a new lithographic parameter to address the geometry azopolymer microstructures and elevates the gradient-field effect by conceptualizing it in this way. The fundamental premise of this strategy is that different wavelengths will elicit varying degrees of the gradient-field effect, thereby inducing disparate microarchitectures. A quantitative study of the three-dimensional morphology of a single pristine micropillar array reconfigured with laser beams of varying wavelengths has demonstrated that predictable control over different photo-deformation evolutions is possible. Moreover, the final microvolume geometry can be modified by adjusting the illumination configuration, polarization state, and exposure dose. This allows the creation of completely different three-dimensional architectures with similar isotropic and anisotropic in-plane deformations. To demonstrate the versatility of this wavelength-dependent three-dimensional microvolume reconfiguration in the fabrication of functional surfaces, the hydrophobicity of an original pristine array can be tuned across a wide range of water contact angle values by deforming the microstructures through the use of two distinct light wavelengths.

The potentiality of the pre-structured azopolymer surface can be extended through the implementation of a spatial intensity gradient strategy produced through a Computer Generated Holography (CGH) system. In Chapter 3, it was demonstrated that a rationalized holographic pattern of locally varying intensity can be used to form intricate micro-architectures, rather than relying on the strong directionality of polarization-based photodeformation. The concept centers on the deterministic design of an intensity distribution of circularly polarized light that aligns with the geometric characteristics of the pre-existing microstructure on the surface. By employing this mechanism, micropillars of a single pristine array have been transformed into a multitude of microstructures, demonstrating a variety of morphologies, including concave, convex, slanted, multifaceted, and hierarchical forms. While this study has demonstrated the potential for a range of architectures, it is evident that the technique offers the possibility of an even broader range of morphologies. It is crucial to

acknowledge that the process of reshaping through holographic patterns is contingent upon the geometric parameters of the original azopolymer microstructure. These include the shape, height, and width of the microstructure, as well as the grayscale patterns, light intensity, and CGH configuration. Each of these parameters can be further tuned to achieve specific outcomes. Furthermore, the group-selective capability of the technique was demonstrated by modifying a sub-array of micropillars into asymmetric microstructures with different relative orientations in a single exposure. This capability could be coupled with sample translation to cover a larger area while maintaining complete control over the reconfiguration of individual microstructures.

The directionality of mass migration that follows the dominant polarization component of the field of light has notable potency; however, it has not been fully exploited for the creation of micro-architecture with robust orientational characteristics. In order to harness this power, Chapter 4 employed the polarization rotator technique, based on a programmable Spatial Light Modulator (SLM), which offers a versatile means of generating any spatial polarization distribution within the field of light. In practice, the method relies on the rational design of a two-dimensional polarization map to be addressed to the SLM in relation to the geometric shape and dimensions of the pre-existing microstructure on the surface. The approach allows for the demonstration of multiple strategies, including large-scale patterning, singular targeting, polarization masks, multi-exposure, and modifications to the microarchitecture of micropillars. These examples demonstrate the versatility of this approach for a range of potential future applications. The large-scale patterning technique may be employed in the fabrication of large surfaces with any desired directional microstructure. Such an approach may be employed for surface applications requiring an average effect from the surface's constituents, such as wettability. The capacity to modify the shape of individual microstructures can be utilized in the creation of surfaces that necessitate precise alterations to the directional attributes of their constituent microstructures. The control of singular microstructure reshaping may be employed in the development of metasurfaces and data storage on surfaces. The diverse range of unconventional microarchitectures have a multitude of potential applications. Rather than focusing on a specific field of application, the objective is to present a technique for the production of microarchitectures with pronounced orientational characteristics. As an illustration, asymmetric microarchitectures have the potential to impart directional wettability.

Challenge and Future Outlook

In comparison to existing techniques, the 3D shaping of azo-microvolumes is based on the relocation of a portion of the azopolymer volume to a novel configuration in a straightforward manner that depends on the gradient of the irradiated light pattern and

the relative polarization distribution. This approach allows for the generation of multiple new 3D architectures without the addition or removal of material from the original structure. This process eliminates the necessity for multiple steps and additional materials following the initial treatment, thus avoiding the use of any chemicals that might affect the specific application in question. Nevertheless, this direct approach is only feasible due to the preexisting microstructures on the azopolymer surface. Consequently, this strategy still at the very least requires assistance from other lithography techniques. The primary challenge in creating complex three-dimensional architectures on the surface using solely azopolymers and light remains unresolved.

In order to meet the challenge presented, it is necessary to develop an approach that can realize micro- and submicro-architectures on azopolymer surfaces with a high degree of complexity, diversity, and controllability, solely through the use of light. This suggests that the approach should be capable of performing the lithography process without relying on other lithography strategies prior to illumination. This will result in a reduction in both cost and complexity of the overall process. In order to achieve this capability, it is essential to have the flexibility to control the field of light in both spatial intensity and polarization distribution. Chapter 3 and Chapter 4 have provided examples of the flexibility to control the architecture of microstructures with locally varying intensity distribution and polarization rotation, independently. An optical approach that can manipulate both properties simultaneously can offer an unparalleled approach to creating complex features on the surface using azopolymer and light, which can be termed “all optical patterning.”

List of Publications

1. **I. K. Januariyasa**, F. Reda, F. Borbone, M. Salvatore, S. L. Oscurato, Molding three-dimensional azopolymer microstructures with holographically structured light. *RSC Appl. Interfaces* (2024).

2. **I. K. Januariyasa**, F. Borbone, M. Salvatore, S. L. Oscurato, Wavelength-Dependent Shaping of Azopolymer Micropillars for Three-Dimensional Structure Control. *ACS Appl. Mater. Interfaces* **15**, 43183–43192 (2023).

3. M. Salvatore, F. Reda, F. Borbone, **I. K. Januariyasa**, P. Maddalena, S. L. Oscurato, Diffractive Refractometer Based on Scalar Theory. *Polymers* **15**, 1605 (2023)

References

1. J. Del Barrio, C. Sánchez-Somolinos, Light to Shape the Future: From Photolithography to 4D Printing. *Advanced Optical Materials* **7**, 1900598 (2019).

2. P. van Assenbergh, E. Meinders, J. Geraedts, D. Dodou, Nanostructure and Microstructure Fabrication: From Desired Properties to Suitable Processes. *Small* **14**, 1703401 (2018).

3. H. Ding, Q. Zhang, H. Gu, X. Liu, L. Sun, M. Gu, Z. Gu, Controlled Microstructural Architectures Based on Smart Fabrication Strategies. *Adv Funct Materials* **30**, 1901760 (2020).

4. J. Ahn, H. Han, J. Ha, Y. Jeong, Y. Jung, J. Choi, S. Cho, S. Jeon, J. Jeong, I. Park, Micro-/Nanohierarchical Structures Physically Engineered on Surfaces: Analysis and Perspective. *Advanced Materials* **36**, 2300871 (2024).

5. M. Schumann, T. Bückmann, N. Gruhler, M. Wegener, W. Pernice, Hybrid 2D–3D optical devices for integrated optics by direct laser writing. *Light Sci Appl* **3**, e175–e175 (2014).

6. Q. Zhang, Z. He, Z. Xie, Q. Tan, Y. Sheng, G. Jin, L. Cao, X. Yuan, Diffractive optical elements 75 years on: from micro-optics to metasurfaces. *Photonics Insights* **2**, R09 (2023).

7. S. Nocentini, D. Martella, C. Parmeggiani, D. S. Wiersma, 3D Printed Photoresponsive Materials for Photonics. *Advanced Optical Materials* **7**, 1900156 (2019).

8. M. Liu, S. Wang, L. Jiang, Nature-inspired superwettability systems. *Nat Rev Mater* **2**, 17036 (2017).

9. Z. Cheng, D. Zhang, X. Luo, H. Lai, Y. Liu, L. Jiang, Superwetting Shape Memory Microstructure: Smart Wetting Control and Practical Application. *Advanced Materials* **33**, 2001718 (2021).

10. W. Li, R. Zhou, Y. Ouyang, Q. Guan, Y. Shen, E. Saiz, M. Li, X. Hou, Harnessing Biomimicry for Controlled Adhesion on Material Surfaces. *Small* **n/a**, 2401859.

11. H.-H. Park, M. Seong, K. Sun, H. Ko, S. M. Kim, H. E. Jeong, Flexible and Shape-Reconfigurable Hydrogel Interlocking Adhesives for High Adhesion in Wet Environments Based on Anisotropic Swelling of Hydrogel Microstructures. *ACS Macro Lett.* **6**, 1325–1330 (2017).

12. J. Wang, F. Jin, X. Dong, J. Liu, M. Zhou, T. Li, M. Zheng, Dual-Stimuli Cooperative Responsive Hydrogel Microactuators Via Two-Photon Lithography. *Small* **19**, 2303166 (2023).

13. J. E. Park, S. Won, W. Cho, J. G. Kim, S. Jhang, J. G. Lee, J. J. Wie, Fabrication and applications of stimuli-responsive micro/nanopillar arrays. *Journal of Polymer Science* **59**, 1491–1517 (2021).

14. J. Qin, L. Yin, Y. Hao, S. Zhong, D. Zhang, K. Bi, Y. Zhang, Y. Zhao, Z. Dang, Flexible and Stretchable Capacitive Sensors with Different Microstructures. *Advanced Materials* **33**, 2008267 (2021).

15. F. He, X. You, W. Wang, T. Bai, G. Xue, M. Ye, Recent Progress in Flexible Microstructural Pressure Sensors toward Human–Machine Interaction and Healthcare Applications. *Small Methods* **5**, 2001041 (2021).

16. V. Harinarayana, Y. C. Shin, Two-photon lithography for three-dimensional fabrication in micro/nanoscale regime: A comprehensive review. *Optics & Laser Technology* **142**, 107180 (2021).

17. K. G. Yager, C. J. Barrett, Novel photo-switching using azobenzene functional materials. *Journal of Photochemistry and Photobiology A: Chemistry* **182**, 250–261 (2006).

18. S. L. Oscurato, M. Salvatore, P. Maddalena, A. Ambrosio, From nanoscopic to macroscopic photo-driven motion in azobenzene-containing materials. *Nanophotonics* **7**, 1387–1422 (2018).

19. A. Priimagi, A. Shevchenko, Azopolymer-based micro- and nanopatterning for photonic applications. *J Polym Sci B Polym Phys* **52**, 163–182 (2014).

20. M. Saphiannikova, V. Toshchevikov, N. Tverdokhleb, Optical deformations of azobenzene polymers: orientation approach *vs.* other concepts. *Soft Matter* **20**, 2688–2710 (2024).

21. P. Rochon, E. Batalla, A. Natansohn, Optically induced surface gratings on azoaromatic polymer films. *Appl. Phys. Lett.* **66**, 136–138 (1995).

22. D. Y. Kim, S. K. Tripathy, L. Li, J. Kumar, Laser-induced holographic surface relief gratings on nonlinear optical polymer films. *Appl. Phys. Lett.* **66**, 1166–1168 (1995).

23. B. Yadav, J. Domurath, K. Kim, S. Lee, M. Saphiannikova, Orientation Approach to Directional Photodeformations in Glassy Side-Chain Azopolymers. *J. Phys. Chem. B* **123**, 3337–3347 (2019).

24. A. Ambrosio, S. Girardo, A. Camposeo, D. Pisignano, P. Maddalena, Controlling spontaneous surface structuring of azobenzene-containing polymers for large-scale nano-lithography of functional substrates. *Appl. Phys. Lett.* **102**, 093102 (2013).

25. L. Mazaheri, S. R. Bobbara, O. Lebel, J.-M. Nunzi, Photoinduction of spontaneous surface relief gratings on Azo DR1 glass. *Opt. Lett.* **41**, 2958 (2016).

26. C. Hubert, C. Fiorini-Debuisschert, I. Maurin, J.-M. Nunzi, P. Raimond, Spontaneous Patterning of Hexagonal Structures in an Azo-Polymer Using Light-Controlled Mass Transport. *Adv. Mater.* **14**, 729 (2002).

27. F. Reda, M. Salvatore, F. Borbone, P. Maddalena, S. L. Oscurato, Accurate Morphology-Related Diffraction Behavior of Light-Induced Surface Relief Gratings on Azopolymers. *ACS Materials Lett.* **4**, 953–959 (2022).

28. N. S. Yadavalli, M. Saphiannikova, S. Santer, Photosensitive response of azobenzene containing films towards pure intensity or polarization interference patterns. *Applied Physics Letters* **105**, 051601 (2014).

29. N. S. Yadavalli, S. Santer, In-situ atomic force microscopy study of the mechanism of surface relief grating formation in photosensitive polymer films. *Journal of Applied Physics* **113**, 224304 (2013).

30. S. L. Oscurato, M. Salvatore, F. Borbone, P. Maddalena, A. Ambrosio, Computer-generated holograms for complex surface reliefs on azopolymer films. *Sci Rep* **9**, 6775 (2019).

31. F. Reda, M. Salvatore, M. Astarita, F. Borbone, S. L. Oscurato, Reprogrammable Holograms from Maskless Surface Photomorphing. *Advanced Optical Materials* **11**, 2300823 (2023).

32. S. L. Oscurato, F. Borbone, P. Maddalena, A. Ambrosio, Light-Driven Wettability Tailoring of Azopolymer Surfaces with Reconfigured Three-Dimensional Posts. *ACS Appl. Mater. Interfaces* **9**, 30133–30142 (2017).

33. J. Choi, W. Jo, S. Y. Lee, Y. S. Jung, S.-H. Kim, H.-T. Kim, Flexible and Robust Superomniphobic Surfaces Created by Localized Photofluidization of Azopolymer Pillars. *ACS Nano* **11**, 7821–7828 (2017).

34. S. Lee, H. S. Kang, A. Ambrosio, J.-K. Park, L. Marrucci, Directional Superficial Photofluidization for Deterministic Shaping of Complex 3D Architectures. *ACS Appl. Mater. Interfaces* **7**, 8209–8217 (2015).

35. W. Jo, H. S. Kang, J. Choi, J. Jung, J. Hyun, J. Kwon, I. Kim, H. Lee, H.-T. Kim, Light-Designed Shark Skin-Mimetic Surfaces. *Nano Lett.* **21**, 5500–5507 (2021).

36. W. Jo, J. Choi, H. S. Kang, M. Kim, S. Baik, B. J. Lee, C. Pang, H.-T. Kim, Programmable Fabrication of Submicrometer Bent Pillar Structures Enabled by a Photoreconfigurable Azopolymer. *ACS Appl. Mater. Interfaces* **12**, 5058–5064 (2020).

37. M. Salvatore, F. Borbone, F. Reda, P. Maddalena, S. L. Oscurato, Programmable surface anisotropy from polarization-driven azopolymer reconfiguration. *J. Phys. Photonics* **3**, 034013 (2021).

38. Z. Wang, C. Hsu, X. Wang, Topographical transition of submicron pillar array of azo molecular glass induced by circularly polarized light. *Sci Rep* **11**, 7327 (2021).

39. S. Lee, H. S. Kang, J. Park, S. Lee, Vertically Oriented, Three-Dimensionally Tapered Deep-Subwavelength Metallic Nanohole Arrays Developed by Photofluidization Lithography. *Advanced Materials* **26**, 7521–7528 (2014).

40. Z. Wang, H. Huang, C. Hsu, X. Wang, Capturing Vector Light Field on Azo Molecular Glass Submicron Pillar Array for Polarization Recording and Creating Optical Functional Surfaces. *Adv Materials Technologies* **8**, 2301173 (2023).

41. H. Huang, Y. Su, J. Xu, X. Wang, Asymmetric Morphology Transformation of Azo Molecular Glass Microspheres Induced by Polarized Light. *Langmuir* **35**, 15295–15305 (2019).

42. W. Wang, Y. Yao, T. Luo, L. Chen, J. Lin, L. Li, S. Lin, Deterministic Reshaping of Breath Figure Arrays by Directional Photomanipulation. *ACS Appl. Mater. Interfaces* **9**, 4223–4230 (2017).

43. J. Strobelt, M. Van Soelen, H. Abourahma, D. J. McGee, Supramolecular Azopolymers for Dynamic Surface Microstructures Using Digital Polarization Optics. *Advanced Optical Materials* **11**, 2202245 (2023).

44. L. De Sio, D. E. Roberts, Z. Liao, S. Nersisyan, O. Uskova, L. Wickboldt, N. Tabiryan, D. M. Steeves, B. R. Kimball, Digital polarization holography advancing geometrical phase optics. *Opt. Express* **24**, 18297 (2016).

45. J. Strobelt, Thesis, Photonic Surface Structure Generation via Spatial Light Modulation and Replication with Nanoimprint Lithography, Berliner Hochschule für Technik, Berlin, Germany (2020).

46. C. Ye, Construction of an optical rotator using quarter-wave plates and an optical retarder. *Opt. Eng* **34**, 3031 (1995).

47. S. L. Oscurato, thesis, Light-driven directional mass transport in azobenzene containing materials for complex textures on surfaces, University of Naples "Federico II", Napoli, Italy (2017).

48. H. M. D. Bandara, S. C. Burdette, Photoisomerization in different classes of azobenzene. *Chem. Soc. Rev.* **41**, 1809–1825 (2012).

49. S. Bian, L. Li, J. Kumar, D. Y. Kim, J. Williams, S. K. Tripathy, Single laser beam-induced surface deformation on azobenzene polymer films. *Applied Physics Letters* **73**, 1817–1819 (1998).

50. S. Bian, J. M. Williams, D. Y. Kim, L. Li, S. Balasubramanian, J. Kumar, S. Tripathy, Photoinduced surface deformations on azobenzene polymer films. *Journal of Applied Physics* **86**, 4498–4508 (1999).

51. P. Karageorgiev, D. Neher, B. Schulz, B. Stiller, U. Pietsch, M. Giersig, L. Brehmer, From anisotropic photo-fluidity towards nanomanipulation in the optical near-field. *Nature Mater* **4**, 699–703 (2005).

52. H. Galinski, A. Ambrosio, P. Maddalena, I. Schenker, R. Spolenak, F. Capasso, Instability-induced pattern formation of photoactivated functional polymers. *Proc. Natl. Acad. Sci. U.S.A.* **111**, 17017–17022 (2014).

53. J. Noga, A. Sobolewska, S. Bartkiewicz, M. Virkki, A. Priimagi, Periodic Surface Structures Induced by a Single Laser Beam Irradiation. *Macromol. Mater. Eng.* **302**, 1600329 (2017).

54. C. Palmer, *Diffraction Grating Handbook* (Newport Corporation, 2005) *sixth edition*.

55. A. Kozanecka-Szmigiel, A. Hernik, K. Rutkowska, J. Konieczkowska, E. Schab-Balcerzak, D. Szmigiel, Surface Relief Modulated Grating in Azo Polymer—From the Tailoring of Diffraction Order to Reshaping of a Laser Beam. *Materials* **15**, 8088 (2022).

56. J. Choi, W. Cho, Y. S. Jung, H. S. Kang, H.-T. Kim, Direct Fabrication of Micro/Nano-Patterned Surfaces by Vertical-Directional Photofluidization of Azobenzene Materials. *ACS Nano* **11**, 1320–1327 (2017).

57. H. Huang, Y. Su, X. Zhou, C. Liao, C. Hsu, Y. Du, J. Xu, X. Wang, Shaping monodispersed azo molecular glass microspheres using polarized light. *Soft Matter* **14**, 5847–5855 (2018).

58. A. Ambrosio, L. Marrucci, F. Borbone, A. Roviello, P. Maddalena, Light-induced spiral mass transport in azo-polymer films under vortex-beam illumination. *Nat Commun* **3**, 989 (2012).

59. T. G. Mayerhöfer, S. Pahlow, J. Popp, The Bouguer-Beer-Lambert Law: Shining Light on the Obscure. *ChemPhysChem* **21**, 2029–2046 (2020).

60. A. Ambrosio, L. Marrucci, F. Borbone, A. Roviello, P. Maddalena, Light-induced spiral mass transport in azo-polymer films under vortex-beam illumination. *Nat Commun* **3**, 989 (2012).

61. A. B. D. Cassie, S. Baxter, Large Contact Angles of Plant and Animal Surfaces. *Nature* **155**, 21–22 (1945).

62. S. Suzuki, K. Ueno, Apparent Contact Angle Calculated from a Water Repellent Model with Pinning Effect. *Langmuir* **33**, 138–143 (2017).

63. A. Tuteja, W. Choi, M. Ma, J. M. Mabry, S. A. Mazzella, G. C. Rutledge, G. H. McKinley, R. E. Cohen, Designing Superoleophobic Surfaces. *Science* **318**, 1618–1622 (2007).

64. A. Tuteja, W. Choi, J. M. Mabry, G. H. McKinley, R. E. Cohen, Robust omniphobic surfaces. *PNAS* **105**, 18200–18205 (2008).

65. L. Barbieri, E. Wagner, P. Hoffmann, Water Wetting Transition Parameters of Perfluorinated Substrates with Periodically Distributed Flat-Top Microscale Obstacles. *Langmuir* **23**, 1723–1734 (2007).

66. J.-H. Lee, W.-S. Choi, K.-H. Lee, J.-B. Yoon, A simple and effective fabrication method for various 3D microstructures: backside 3D diffuser lithography. *J. Micromech. Microeng.* **18**, 125015 (2008).

67. K. Chen, Z. Guan, Z. Li, Y. Yang, Z. He, S. Yu, G. Zheng, Computer-Generated Holographic Nanoprinting. *Laser & Photonics Reviews* **17**, 2200448 (2023).

68. M. Zhang, A. Pal, X. Lyu, Y. Wu, M. Sitti, Artificial-goosebump-driven microactuation. *Nat. Mater.* **23**, 560–569 (2024).

69. K. Matsushima, *Introduction to Computer Holography: Creating Computer-Generated Holograms as the Ultimate 3D Image* (Springer International Publishing, Cham, 2020; http://link.springer.com/10.1007/978-3-030-38435-7)*Series in Display Science and Technology*.

70. S. L. Oscurato, F. Reda, M. Salvatore, F. Borbone, P. Maddalena, A. Ambrosio, Shapeshifting Diffractive Optical Devices. *Laser & Photonics Reviews* **16**, 2100514 (2022).

71. M. Pasienski, B. DeMarco, A high-accuracy algorithm for designing arbitrary holographic atom traps. *Opt. Express* **16**, 2176 (2008).

72. R. W. Gerchberg, W. O. Saxton, A Practical Algorithm for the Determination of Phase from Image and Diffraction Plane Pictures. *Optik* **35**, 237–246 (1972).

73. N. Tverdokhleb, S. Loebner, B. Yadav, S. Santer, M. Saphiannikova, Viscoplastic Modeling of Surface Relief Grating Growth on Isotropic and Preoriented Azopolymer Films. *Polymers* **15**, 463 (2023).

74. S. Loebner, B. Yadav, N. Lomadze, N. Tverdokhleb, H. Donner, M. Saphiannikova, S. Santer, Local Direction of Optomechanical Stress in Azobenzene Containing Polymers During Surface Relief Grating Formation. *Macro Materials & Eng* **307**, 2100990 (2022).

75. I. K. Januariyasa, F. Borbone, M. Salvatore, S. L. Oscurato, Wavelength-Dependent Shaping of Azopolymer Micropillars for Three-Dimensional Structure Control. *ACS Appl. Mater. Interfaces* **15**, 43183–43192 (2023).

76. X. Kong, X. Wang, T. Luo, Y. Yao, L. Li, S. Lin, Photomanipulated Architecture and Patterning of Azopolymer Array. *ACS Appl. Mater. Interfaces* **9**, 19345–19353 (2017).

77. Z. Wang, H. Huang, C. Hsu, X. Wang, Laser-Induced Transitions of Azo Molecular Glass Pillar Arrays: A New Way to Fabricate Periodic Complex Surface Patterns upon Linearly Polarized Radiation. *Advanced Optical Materials* **10**, 2102795 (2022).

78. Z.-W. Chen, M.-Q. Cai, K.-Q. Qiu, Y.-N. Wang, H.-Y. Chen, Z.-K. Liu, Y. Liu, Y.-L. Hong, H.-J. Jiang, Z.-W. Hu, Fabrication of large UV transmission blazed gratings for slitless spectral sky survey. *Res. Astron. Astrophys.* **21**, 307 (2021).

79. J. Gao, P. Chen, L. Wu, B. Yu, L. Qian, A review on fabrication of blazed gratings. *J. Phys. D: Appl. Phys.* **54**, 313001 (2021).

80. F. Pirani, A. Angelini, F. Frascella, R. Rizzo, S. Ricciardi, E. Descrovi, Light-Driven Reversible Shaping of Individual Azopolymeric Micro-Pillars. *Sci Rep* **6**, 31702 (2016).

81. J. Strobelt, D. Stolz, M. Leven, M. V. Soelen, L. Kurlandski, H. Abourahma, D. J. McGee, Optical microstructure fabrication using structured polarized illumination. *Opt. Express* **30**, 7308 (2022).

82. O. Senel, B. Gruppuso, J. Strobelt, D. J. McGee, “Continuous laser printing of surface relief microstructures on photomechanically-responsive azopolymer films using structured optical polarization” in *Advanced Fabrication Technologies for Micro/Nano Optics and Photonics XVII*, G. Von Freymann, E. Blasco, D. Chanda, Eds. (SPIE, San Francisco, United States, 2024; https://www.spiedigitallibrary.org/conference-proceedings-of-spie/12898/3000374/Continuous-laser-printing-of-surface-relief-microstructures-on-photomechanically-responsive/10.1117/12.3000374.full), p. 33.

83. L. Wu, Z. Dong, M. Kuang, Y. Li, F. Li, L. Jiang, Y. Song, Printing Patterned Fine 3D Structures by Manipulating the Three Phase Contact Line. *Advanced Functional Materials* **25**, 2237–2242 (2015).

84. C. Zhang, Y. Hu, W. Du, P. Wu, S. Rao, Z. Cai, Z. Lao, B. Xu, J. Ni, J. Li, G. Zhao, D. Wu, J. Chu, K. Sugioka, Optimized holographic femtosecond laser patterning method towards rapid integration of high-quality functional devices in microchannels. *Sci Rep* **6**, 33281 (2016).

85. B. Berteloot, I. Nys, S. Liu, K. Neyts, Two-Dimensional Liquid-Crystal Photoalignment by Multiple Illumination Steps. *ACS Appl. Opt. Mater.* **2**, 1295–1302 (2024).

86. B. Berteloot, I. Nys, G. Poy, J. Beeckman, K. Neyts, Ring-shaped liquid crystal structures through patterned planar photo-alignment. *Soft Matter* **16**, 4999–5008 (2020).